On Stresses and Fatigue

in

Flexible Pipes

by

Svein Sævik

Trondheim, December 1992

DEPARTMENT OF MARINE STRUCTURES

FACULTY OF MARINE TECHNOLOGY

THE NORWEGIAN INSTITUTE OF TECHNOLOGY

THE UNIVERSITY OF TRONDHEIM, NORWAY

ISBN 82-7119-427-5 ISSN 082-3271

TABLE OF CONTENTS:

 ISBN 82-7119-427-5 ISSN 082-3271

 ISBN 82-7119-427-5 ISSN 082-3271

 ISBN 82-7119-427-5 ISSN 082-3271

 ISBN 82-7119-427-5 ISSN 082-3271

 ISBN 82-7119-427-5 ISSN 082-3271

SUMMARY

The main purpose of this work is to improve existing methods for stress and slip analysis of nonbonded flexible pipe armouring layers and to contribute to better understanding of the flexible pipe behaviour under dynamic loading.

Existing methods have been based on simple analytical formulas and are unable to take into account the effects from realistic end restraints. A finite element formulation has therefore been developed solving the equilibrium equations for one armouring tendon with arbitrary loading and boundary conditions. Several case studies have been carried out both to verify the accuracy of the model and to investigate different physical effects, giving better understanding of flexible pipe behaviour. Results from the present model have also been compared with corresponding calculations by other more simple methods. The main conclusion from this investigation is that the existing models cannot be used to predict stresses in the end fitting region and that they will give conservative estimates for relative displacements and wear.

Deviations have been found between test data and results obtained by simple formulas regarding cross section characteristics. Proposed improvements of such formulas have shown to give improved correlation with test results.

The present model has been verified by quantitative and qualitative comparisons with experimental data. The quantitative comparison has been carried out by measuring strains along one tendon of a 4-inch nonbonded pipe and then compare results from the numerical model. The overall conclusion from this comparison is that there is a good correlation between predicted and measured behaviour. The qualitative comparison has been carried out by investigating the correlation between the predicted conditions of stresses and displacements, and the failure modes obtained by fatigue testing of two 4-inch flexible pipes. Good correlation has been found between the predicted conditions and the observed failure modes.

The overall conclusion is that the developed model is capable of describing the stresses and displacements needed to evaluate various failure modes. The potential of the method is to

 ISBN 82-7119-427-5 ISSN 082-3271

perform fatigue analysis of flexible risers at end restraints on the basis of SN-data in a similar way as for tensioned steel risers. The failure modes found from experiments are, however, not included among failure modes discussed so far in the literature. Thus there is an obvious need for future research work both to identify all relevant failure modes and to quantify the primary parameters describing each individual failure mode.

 ISBN 82-7119-427-5 ISSN 082-3271

ACKNOWLEDGEMENTS

This work was made possible by a scholarship from The Royal Norwegian Research Council (NTNF) and financial support by STATOIL. A part of this study has further been based on experiments that were carried out within the scope of a multiclient research project FPS-2000 - Flexible Pipes and Risers.

The study has been carried out at the Norwegian Institute of Technology (NTH), Department of Marine Structures under the supervision of Professor Carl M. Larsen and Professor II Tore H. Søreide (A.R.Reinertsen). Their interest in my work and suggestions for improvements of the final manuscript are gratefully acknowledged.

I am also very grateful to Elie Kodaissi and Geir Horrigmoe for their participation as members of the thesis committee.

Thanks are also extended to colleagues at SINTEF, Division of Structural Engineering, NTH, Department of Marine Structures, NTH, Marine Structures Laboratory, MARINTEK and A.R. Reinertsen for numerous helpful discussions and encouragements throughout the course of the work.

Among those who have contributed to my thesis:

The FPS-2000 Project Team, particularly Mr. Arild Bech, SINTEF, Division of Structural Engineering for helpful discussions and guidance related to the CAFLEX computer program and Professor Stig Berge, NTH, Department of Marine Structures for support and guidance during the experimental work.

Dr. Knut Arild Farnes, NTH, Department of Marine Structures, always being helpful related to software as well as hardware problems.

Dr. Nils Sødahl, MARINTEK, for providing global analysis results for 8-inch flexible riser case study.

Dr. Erik Levold, A.R. Reinertsen, for valuable discussions regarding mathematical aspects.

Ms. Guri Berge, SINTEF, Division of Structural Engineering, for preparation of excellent figures.

NOMENCLATURE

General rules

- *Vectors, tensors* and *matrices* are written by bold letters, e.g. **N**, ***X***.
- A transpose of a matrix is denoted by superscript T.
- Strains and displacements referred to the tendon cross section centre line is denoted by superscript ^{0}.
- Strains referred to the local curvilinear coordinate system is denoted by superscript *.
- Subscript 0 denotes initial configuation.
- Δ is used to denote incremental values.
- In general the letters *i,j,k,l,m,n* are used as indices describing vector and tensor components if not otherwise noted.
- For the purpose of tensor and vector calculations, capital letters are used both for base vectors and vector and tensor components in the undeformed configuration. The same rule also apply for indices. In the deformed configuration small letters are used.
- Einstein's *summation convention* is adopted when writing tensor components or index form.
- A partial derivative is whenever convenient denoted by comma followed by the index representing the variable involved, e.g.:

$$Z^I_{,1} = \frac{\partial Z^I}{\partial X^1}$$

ISBN 82-7119-427-5 ISSN 082-3271

- The square of the arc length along dr referred to the local curvilinear axes x^j with base vectors g_j is expressed by the single dot product as:

$$dl^2 = dr \cdot dr = dx^i dx^j g_i \cdot g_j = g_{ij}\, dx^i dx^j$$

where g_{ij} is the covariant metric tensor.

- For transformation of a second order tensor with components A_{KL}^* referred to the local curvilinear coordinate system with axes X^I to corresponding components A_{IJ} in a local Cartesian coordinate system with axes Y^I, the following transformation rule apply:

$$A_{IJ} = \frac{\partial X^K}{\partial Y^I}\frac{\partial X^L}{\partial Y^J} A^*_{KL}$$

- The scalar product or double dot product of two second order tensors is denoted by a double dot, e.g.:

$$d = \boldsymbol{a}:\boldsymbol{b} = a^{ij}\, b_{ij}$$

where a^{ij} is the *contravariant* components of $\boldsymbol{a}$ and b_{ij} is the *covariant* components of $\boldsymbol{b}$

- The cross product is denoted by a cross $\times$, e.g.:

$$\boldsymbol{a} \times \boldsymbol{b} = e_{ijk}\, a_j\, b_k\, \boldsymbol{I}_i$$

where e_{ijk} is the permutation symbol.

 ISBN 82-7119-427-5 ISSN 082-3271

Roman letters

a - Width of tendon cross section (m).

A - Rod cross section area (m^2).

b - Thickness of tendon cross section (m).

c - Radius of individual contact areas between two layers of armouring (m).

C_σ - Young's modulus of elasticity (Nm^{-2}).

C_τ - Shear modulus (Nm^{-2}).

D - Cross section torsion constant defined by Eq.(2.101) (m^4).

EI - Cross section sliding bending stiffness (Nm^2).

E_I - Base vectors directed along pipe centre line Cartesian coordinate axes.

E, E_{IJ} - Tensor and component form of the Green strain tensor in local Cartesian system

E^*_{IJ} - Green strain tensor components in local curvilinear system

E^{*0}_{IJ} - Green strain tensor components along rod centre line in local curvilinear system.

G - Determinant of metric tensor.

G_I, g_i - Base vectors directed along the local curvilinear coordinate axes in undeformed, deformed configurations.

G^{KL}, g^{kl} - Contravariant components of metric tensor in undeformed, deformed configurations.

G_{KL}, g_{kl} - Covariant components of metric tensor in undeformed, deformed configurations.

h - Normalized gap between individual tendons = gap/width.

I_I - Base vectors directed along curve principal torsion-flexure axes.

I_t - Cross section torsion constant defined by the integral in Eq.(2.101) (m^4).

I_p - Polar moment of inertia (m^4).

I_2 - Inertia moment about X^2 axis (m^4).

I_3 - Inertia moment about X^3 axis (m^4).

J_I - Base vectors directed along local Cartesian coordinate axes.

k - Element stiffness matrix.

K_1 - Cross section torsion constant defined by Eq.(2.102) (m^6).

K_2 - Cross section torsion constant defined by Eq.(2.104) (m^4).

 ISBN 82-7119-427-5 ISSN 082-3271

K_T - Tangential stiffness matrix.

l - Element length (m).

m_I - Distributed moment acting about the local coordinate axes (N).

M_I - Moment stress resultant acting about the local coordinate axes (Nm).

N - Matrix of displacement interpolation functions.

P,p - Denotes a material point in the rod cross section during undeformed, deformed configurations.

P_0p_0 - Denotes a material point at the centre line of the rod during undeformed, deformed configurations.

Q_I - Force stress resultants acting along the local coordinate axes (N).

ΔQ - Incremental load vector of total equilibrium equation system.

Δq - Incremental nodal displacement vector of total equation system.

q_I - Distributed loads acting along the local coordinate axes (Nm^{-1}).

R - Layer radius from pipe centre line to tendon centre line (m).

R,r - Position vector of a material particle arbitrarily positioned in the rod cross section during undeformed, deformed configurations.

R_0r_0 - Position vector of a material particle positioned in the centre line of the rod cross section during undeformed, deformed configurations.

S_0S - Surface of rod in undeformed, deformed configurations.

S - Element load vector.

t - Surface traction.

u,u_i - Vector and component form of displacement field.

u^0,u_i^0 - Vector and component form of displacement field along centre line.

V_0V - Volume of rod in undeformed/deformed configurations

v,w - Surface coordinates.

v - Vector of element degrees of freedom.

X^I,x^i - Local curvilinear coordinates.

Z^I - Cartesian coordinates referred to a Cartesian coordinate system arbitrarily positioned along the pipe centre line.

z - Pipe longitudinal coordinate referred to a fixed Cartesian coordinate system.

 ISBN 82-7119-427-5 ISSN 082-3271

On Stresses and Fatigue

in

Flexible Pipes

by

Svein Sævik

Trondheim, December 1992

DEPARTMENT OF MARINE STRUCTURES

FACULTY OF MARINE TECHNOLOGY

THE NORWEGIAN INSTITUTE OF TECHNOLOGY

THE UNIVERSITY OF TRONDHEIM, NORWAY

 ISBN 82-7119-427-5 ISSN 0802-3271

TABLE OF CONTENTS:

 ISBN 82-7119-427-5 ISSN 0802-3271

 ISBN 82-7119-427-5 ISSN 0802-3271

 ISBN 82-7119-427-5 ISSN 0802-3271

 ISBN 82-7119-427-5 ISSN 0802-3271

 ISBN 82-7119-427-5 ISSN 0802-3271

SUMMARY

The main purpose of this work is to improve existing methods for stress and slip analysis of nonbonded flexible pipe armouring layers and to contribute to better understanding of the flexible pipe behaviour under dynamic loading.

Existing methods have been based on simple analytical formulas and are unable to take into account the effects from realistic end restraints. A finite element formulation has therefore been developed solving the equilibrium equations for one armouring tendon with arbitrary loading and boundary conditions. Several case studies have been carried out both to verify the accuracy of the model and to investigate different physical effects, giving better understanding of flexible pipe behaviour. Results from the present model have also been compared with corresponding calculations by other more simple methods. The main conclusion from this investigation is that the existing models cannot be used to predict stresses in the end fitting region and that they will give conservative estimates for relative displacements and wear.

Deviations have been found between test data and results obtained by simple formulas regarding cross section characteristics. Proposed improvements of such formulas have shown to give improved correlation with test results.

The present model has been verified by quantitative and qualitative comparisons with experimental data. The quantitative comparison has been carried out by measuring strains along one tendon of a 4-inch nonbonded pipe and then compare results from the numerical model. The overall conclusion from this comparison is that there is a good correlation between predicted and measured behaviour. The qualitative comparison has been carried out by investigating the correlation between the predicted conditions of stresses and displacements, and the failure modes obtained by fatigue testing of two 4-inch flexible pipes. Good correlation has been found between the predicted conditions and the observed failure modes.

The overall conclusion is that the developed model is capable of describing the stresses and displacements needed to evaluate various failure modes. The potential of the method is to

 ISBN 82-7119-427-5 ISSN 0802-3271

perform fatigue analysis of flexible risers at end restraints on the basis of SN-data in a similar way as for tensioned steel risers. The failure modes found from experiments are, however, not included among failure modes discussed so far in the literature. Thus there is an obvious need for future research work both to identify all relevant failure modes and to quantify the primary parameters describing each individual failure mode.

 ISBN 82-7119-427-5 ISSN 0802-3271

ACKNOWLEDGEMENTS

This work was made possible by a scholarship from The Royal Norwegian Research Council (NTNF) and financial support by STATOIL. A part of this study has further been based on experiments that were carried out within the scope of a multiclient research project FPS-2000 - Flexible Pipes and Risers.

The study has been carried out at the Norwegian Institute of Technology (NTH), Department of Marine Structures under the supervision of Professor Carl M. Larsen and Professor II Tore H. Søreide (A.R.Reinertsen). Their interest in my work and suggestions for improvements of the final manuscript are gratefully acknowledged.

I am also very grateful to Elie Kodaissi and Geir Horrigmoe for their participation as members of the thesis committee.

Thanks are also extended to colleagues at SINTEF, Division of Structural Engineering, NTH, Department of Marine Structures, NTH, Marine Structures Laboratory, MARINTEK and A.R. Reinertsen for numerous helpful discussions and encouragements throughout the course of the work.

Among those who have contributed to my thesis:

The FPS-2000 Project Team, particularly Mr. Arild Bech, SINTEF, Division of Structural Engineering for helpful discussions and guidance related to the CAFLEX computer program and Professor Stig Berge, NTH, Department of Marine Structures for support and guidance during the experimental work.

Dr. Knut Arild Farnes, NTH, Department of Marine Structures, always being helpful related to software as well as hardware problems.

Dr. Nils Sødahl, MARINTEK, for providing global analysis results for 8-inch flexible riser case study.

Dr. Erik Levold, A.R. Reinertsen, for valuable discussions regarding mathematical aspects.

Ms. Guri Berge, SINTEF, Division of Structural Engineering, for preparation of excellent figures.

NOMENCLATURE

General rules

- *Vectors, tensors* and *matrices* are written by bold letters, e.g. **N**, ***X***.
- A transpose of a matrix is denoted by superscript T.
- Strains and displacements referred to the tendon cross section centre line is denoted by superscript ^{0}.
- Strains referred to the local curvilinear coordinate system is denoted by superscript *.
- Subscript 0 denotes initial configuation.
- Δ is used to denote incremental values.
- In general the letters *i,j,k,l,m,n* are used as indices describing vector and tensor components if not otherwise noted.
- For the purpose of tensor and vector calculations, capital letters are used both for base vectors and vector and tensor components in the undeformed configuration. The same rule also apply for indices. In the deformed configuration small letters are used.
- Einstein's *summation convention* is adopted when writing tensor components or index form.
- A partial derivative is whenever convenient denoted by comma followed by the index representing the variable involved, e.g.:

$$Z^I_{,1} = \frac{\partial Z^I}{\partial X^1}$$

 ISBN 82-7119-427-5 ISSN 0802-3271

- The square of the arc length along dr referred to the local curvilinear axes x^i with base vectors g_j is expressed by the single dot product as:

$$dl^2 = dr \cdot dr = dx^i dx^j g_i \cdot g_j = g_{ij}\, dx^i dx^j$$

where g_{ij} is the covariant metric tensor.

- For transformation of a second order tensor with components A_{KL}^* referred to the local curvilinear coordinate system with axes X^I to corresponding components A_{IJ} in a local Cartesian coordinate system with axes Y^I, the following transformation rule apply:

$$A_{IJ} = \frac{\partial X^K}{\partial Y^I}\frac{\partial X^L}{\partial Y^J} A^*_{KL}$$

- The scalar product or double dot product of two second order tensors is denoted by a double dot, e.g.:

$$d = a{:}b = a^{ij}\, b_{ij}$$

where a^{ij} is the *contravariant* components of a and b_{ij} is the *covariant* components of b

- The cross product is denoted by a cross $\times$, e.g.:

$$a \times b = e_{ijk}\, a_j\, b_k\, I_i$$

where e_{ijk} is the permutation symbol.

 ISBN 82-7119-427-5 ISSN 0802-3271

Roman letters

a - Width of tendon cross section (m).

A - Rod cross section area (m^2).

b - Thickness of tendon cross section (m).

c - Radius of individual contact areas between two layers of armouring (m).

C_σ - Young's modulus of elasticity (Nm^{-2}).

C_τ - Shear modulus (Nm^{-2}).

D - Cross section torsion constant defined by Eq.(2.101) (m^4).

EI - Cross section sliding bending stiffness (Nm^2).

E_I - Base vectors directed along pipe centre line Cartesian coordinate axes.

E, E_{IJ} - Tensor and component form of the Green strain tensor in local Cartesian system

E^*_{IJ} - Green strain tensor components in local curvilinear system

E^{*0}_{IJ} - Green strain tensor components along rod centre line in local curvilinear system.

G - Determinant of metric tensor.

G_i, g_i - Base vectors directed along the local curvilinear coordinate axes in undeformed, deformed configurations.

G^{KL}, g^{kl} - Contravariant components of metric tensor in undeformed, deformed configurations.

G_{KL}, g_{kl} - Covariant components of metric tensor in undeformed, deformed configurations.

h - Normalized gap between individual tendons = gap/width.

I_I - Base vectors directed along curve principal torsion-flexure axes.

I_t - Cross section torsion constant defined by the integral in Eq.(2.101) (m^4).

I_p - Polar moment of inertia (m^4).

I_2 - Inertia moment about X^2 axis (m^4).

I_3 - Inertia moment about X^3 axis (m^4).

J_I - Base vectors directed along local Cartesian coordinate axes.

k - Element stiffness matrix.

K_1 - Cross section torsion constant defined by Eq.(2.102) (m^6).

K_2 - Cross section torsion constant defined by Eq.(2.104) (m^4).

 ISBN 82-7119-427-5 ISSN 0802-3271

K_T - Tangential stiffness matrix.

l - Element length (m).

m_I - Distributed moment acting about the local coordinate axes (N).

M_I - Moment stress resultant acting about the local coordinate axes (Nm).

N - Matrix of displacement interpolation functions.

P,p - Denotes a material point in the rod cross section during undeformed, deformed configurations.

P_0p_0 - Denotes a material point at the centre line of the rod during undeformed, deformed configurations.

Q_I - Force stress resultants acting along the local coordinate axes (N).

ΔQ - Incremental load vector of total equilibrium equation system.

Δq - Incremental nodal displacement vector of total equation system.

q_I - Distributed loads acting along the local coordinate axes (Nm^{-1}).

R - Layer radius from pipe centre line to tendon centre line (m).

R,r - Position vector of a material particle arbitrarily positioned in the rod cross section during undeformed, deformed configurations.

R_0r_0 - Position vector of a material particle positioned in the centre line of the rod cross section during undeformed, deformed configurations.

S_0S - Surface of rod in undeformed, deformed configurations.

S - Element load vector.

t - Surface traction.

u,u_i - Vector and component form of displacement field.

u^0,u_i^0 - Vector and component form of displacement field along centre line.

V_0V - Volume of rod in undeformed/deformed configurations

v,w - Surface coordinates.

v - Vector of element degrees of freedom.

X^I,x^i - Local curvilinear coordinates.

Z^I - Cartesian coordinates referred to a Cartesian coordinate system arbitrarily positioned along the pipe centre line.

z - Pipe longitudinal coordinate referred to a fixed Cartesian coordinate system.

 ISBN 82-7119-427-5 ISSN 0802-3271

Greek letters

α - Tendon lay angle.

β - Twist (m^{-1}).

Γ - Cross section torsion constant defined by Eq.(2.103) (m^6).

Δ - Incrementation symbol.

$\Delta\sigma_{fg}$ - Fatigue stress limit (Nm^{-2}).

δ - Virtualization symbol.

ε_z - Global pipe axial strain.

ε_1 - Axial strain of rod.

$\varepsilon_2, \varepsilon_3$ - Kinematic quantities expressing rotation.

$\varepsilon, \varepsilon_{ij}$ - Tensor and component form of the natural strain tensor in local Cartesian coordinate system

θ - Denotes rotation angle.

θ_i - Rotation about the local curvilinear axes.

κ - Principal curvature along curve (m^{-1}).

κ_1 - Total accumulated torsion of rod centre line (m^{-1}).

κ_2 - Total accumulated transverse curvature of rod centre line (m^{-1}).

κ_3 - Total accumulated normal curvature of rod centre line (m^{-1}).

κ_r, κ_c - Principal curvatures of the supporting surface (m^{-1}).

κ_t - Pipe surface curvature in transverse tendon direction (along the X^3 axis) (m^{-1}).

λ - Lagrange multiplier.

μ - Coefficient of friction.

ξ - Non-dimensional length coordinate along beam element.

ρ - Radius of curvature of pipe surface at neutral axis (m).

σ, σ^{ij} - Tensor and component form of the Cauchy stress tensor in the local Cartesian coordinate system.

σ_a - Axial stress component (Nm^{-2}).

σ_{at} - Axial stress component induced by tension loading (Nm^{-2}).

σ_{ac} - Axial stress component induced by curvature effects (Nm^{-2}).

σ_{b2} - Bending stress component caused by bending about the surface normal, i.e transverse curvature (Nm^{-2}).

σ_{b3} - Bending stress component caused by normal curvature (Nm^{-2}).

τ - Torsion along curve (m^{-1}).

ϕ - Spherical coordinate angle.

ω - Angle between surface normal and curve normal.

$\varphi(X^2,X^3)$ - St.Venant warping function.

ω_1 - Torsion deformation, i.e. twist (m^{-1}). Between two equilibrium states (m^{-1}), $\Delta\omega_1 \equiv \Delta\kappa_1$.

ω_2 - Transverse curvature deformation (m^{-1}). Between two equilibrium states, $\Delta\omega_2 \equiv \Delta\kappa_2$.

ω_3 - Normal curvature deformation (m^{-1}). Between two equilibrium states, $\Delta\omega_3 \equiv \Delta\kappa_3$.

 ISBN 82-7119-427-5 ISSN 0802-3271

1 INTRODUCTION

1.1 The flexible pipe concept

The flexible pipe concept has been successfully used during several years both as dynamic risers and flowlines in connection with fixed and floating offshore petroleum production. For floating production systems it represents an attractive alternative to a tensioned steel riser since it does not require a heave compensation and tensioner system at the top. At the same time, it offers easy installation and reuse. This application requires a long duration pipe with high capacity with regard to tensile loading and bending, and to internal and external pressure, combined with a low bending stiffness and low critical radius of curvature.

1.1.1 Cross section properties

The desired properties are obtained by making a composite layered cross section where each layer has its specific function. The basic principle is based on using a synthetic conduit that provides sealing of the transported product and then apply helical reinforcement in order to carry the internal pressure.

Flexible pipes can be classified into bonded and nonbonded pipes depending on the cross section structure. Nonbonded pipes have separate layers that are free to move relative to each

 ISBN 82-7119-427-5 ISSN 0802-3271

other, while the cross section of a bonded pipe is vulcanized, i.e. layers are completely bonded. Examples of typical cross sections of bonded and nonbonded flexible pipes are shown in Figure 1.1.

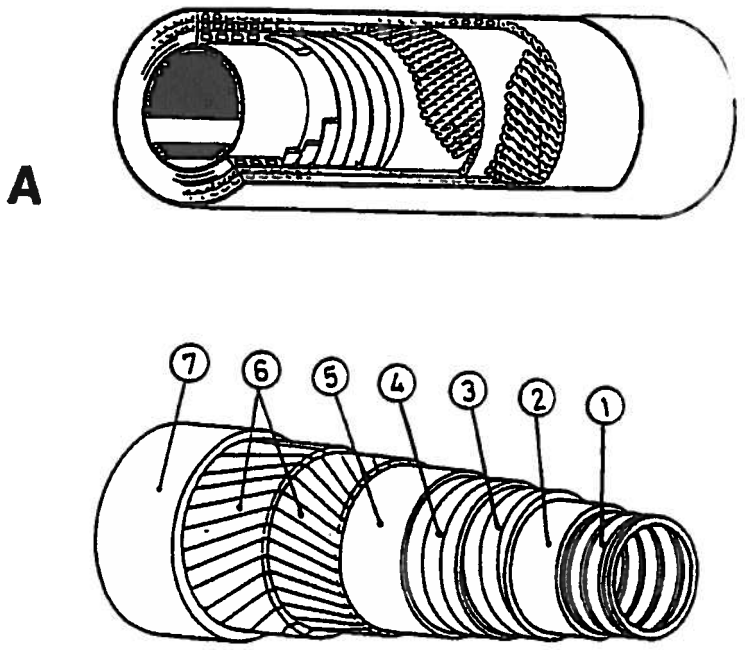

Figure 1.1 Cross sections of flexible pipes

The basic principle ensuring flexibility of nonbonded flexible pipes during bending is that the armouring tendons are free to slip under low friction. For the bonded pipe, the tendons are restrained by the surrounding rubber. The basic idea here is however to utilize the fact that the low shear modulus of the rubber will control and restrict the stresses induced by bending and hence give a sufficient flexibility.

The dominating type of flexibles today is the nonbonded pipe, which is the type that will be focused on in the present work. The function of each layer of the nonbonded pipe shown in Figure 1.1 B is given by:

1. Inner steel carcass to prevent collapse of the inner plastic sheath due to external pressure.

2. Inner plastic sheath to provide sealing of the internal fluid.

 ISBN 82-7119-427-5 ISSN 0802-3271

3. A wound steel spiral, called zeta spiral, to provide capacity with regard to radial loading caused by internal and external pressure.

4. Flat steel carcass to give additional resistance to the radial forces in very high pressure pipes.

5. Anti-friction intermediate plastic sheath.

6. Double cross-wound armouring layers to provide axial and torsional capacity of the pipe.

7. External plastic sheath for protection against corrosion and to bind the underlaying armouring layers.

There are several alternative terms in use when referring to one armouring element. Example of names are *spiral, strand, wire and tendon.* Normally, the term *wire,* is used when referring to the armouring used in bonded pipes, each being made of a number of thin steel *strands* that are helically wound into a wire structure. The term *tendon* is used when referring to the armouring used in nonbonded pipes, each representing a continuous steel cross section, which is helically cold-drawn onto the supporting pipe structure. Throughout this study, the term *tendon* will be used when referring to any helically wound armouring element if not otherwise noted.

Flexible pipe design for static applications takes into consideration the initial strength of the pipe and degradation with time of the materials involved, for example by corrosion, ageing and erosion.

In dynamic application other phenomena are important:

Mechanical deterioration of the strength by fatigue or wear induced by slip between layers due to cyclic bending.

 ISBN 82-7119-427-5 ISSN 0802-3271

High stresses in the armouring layers due to tension and bending extremes.

Thus both stresses and relative movement between layers are important response parameters to consider when describing the structural response of flexible pipes exposed to dynamic loading.

The present work will focus on establishing models that can be used for stress and fatigue analysis of armouring layers in flexible pipes exposed to torsion, tension and bending deformation. The problem of material ageing is thus not considered.

1.1.2 Physical behaviour of flexible pipes

The physical behaviour of a flexible pipe exposed to tension, torsion and bending depends on the cross section structure. A bonded pipe will within the relevant range of loading typically respond linearly to all these loadings , as shown in Figure 1.2 a. This is also valid for the nonbonded pipe as long as it is exposed to tension and torsion.

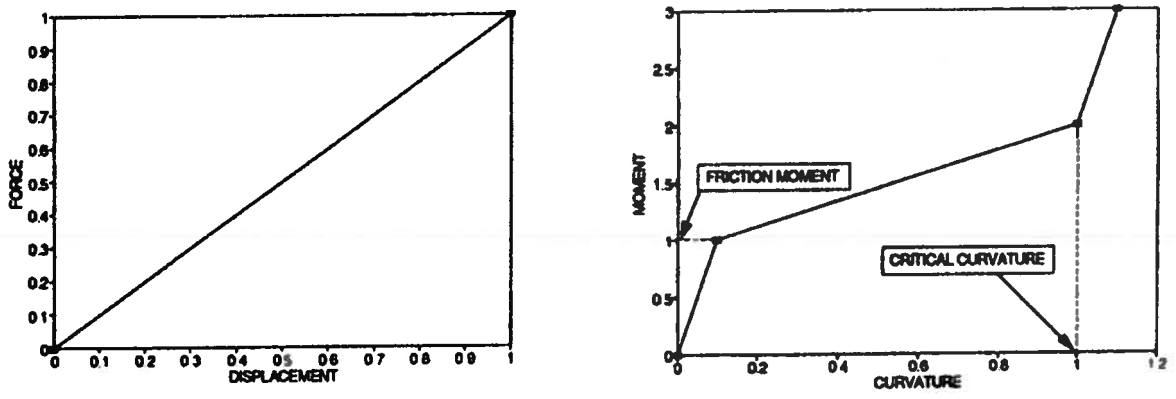

a. Axisymmetric behaviour

b. Behaviour in bending

Figure 1.2 Behaviour of flexible pipes

 ISBN 82-7119-427-5 ISSN 0802-3271

During bending, however, the nonbonded pipe will have a nonlinear moment-curvature relationship as shown in Figure 1.2 b. The first region of the curve corresponds to the assumption that plane sections remain plane, i.e there is no slip between the armouring and the supporting pipe structure. Thus, the bending stiffness is comparable to a steel pipe of similar dimension. As the moment increase beyond the limit which is normally termed *the friction moment*, slip will occur due to the shear stresses developed between the armouring element and the supporting pipe structure, leading to a significant drop in bending stiffness. The new bending stiffness will in the following be termed *the sliding bending stiffness* and is given by the stiffness of the plastic tubulars and the strain energy related to local bending moments and torsion in each armouring tendon. It also represents the bending stiffness normally given from the manufacturers for the purpose of global design analyses.

The sliding bending stiffness remains constant until the initial gaps between each tendon are closed. This occurs at the *critical radius of curvature* and from that point, the bending stiffness and armouring stresses will increase significantly. The critical curvature represents therefore a design limit that should not be exceeded under normal operation.

For a bonded pipe, the critical radius of curvature is normally determined from the maximum allowable outer fibre strain in the rubber. In some designs this criteria will also apply for nonbonded pipes.

1.1.3 Riser configurations

Flexible pipes have a large number of applications related to offshore production of oil and gas. The present study will specially focus on investigating the internal response of flexible pipes used as fully dynamic risers in fixed and floating offshore production and offshore loading systems. Other applications, such as flexible spools or flowlines laying on the seabed, will not be investigated.

Examples of commonly used riser configurations in offshore production systems are presented in Figure 1.3.

 ISBN 82-7119-427-5 ISSN 0802-3271

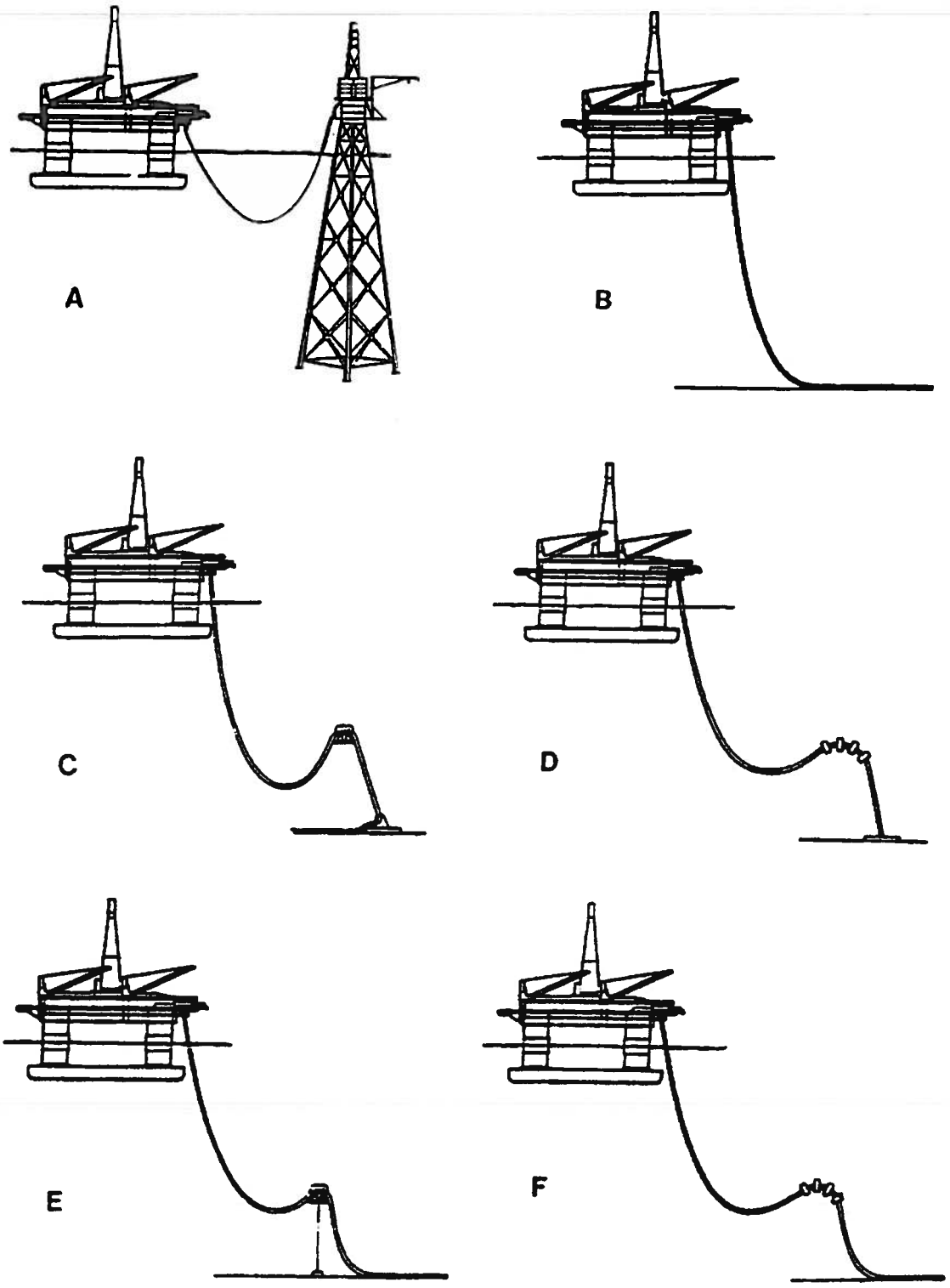

Figure 1.3 Riser configurations

These single riser configurations are often the basic components of more complex riser systems. Thus, a basic knowledge of the behaviour of these will be most important in connection with design of most flexible riser systems. The jumper configuration (see Figure

 ISBN 82-7119-427-5 ISSN 0802-3271

1.3 A) is used for transfer of fluids from a fixed wellhead platform to a floating production unit, confer Bjelland [1.1] and Brown et. al. [1.2]. The jumper configuration is also frequently used in offshore loading systems.

No objective procedure has been established for optimizing a flexible riser configuration. Selecting a configuration for a particular floating production system has therefore to be based on experience and engineering judgements. A tentative ranking of the standard configurations is presented by Pettenati-Auziere [1.3] and is based on static and dynamic behaviour, ease of installation, adaptability to other installations and costs.

1.1.4 Termination of flexible risers to rigid structures

An important problem in flexible riser design is how to terminate the flexible riser to rigid structures. A practical way to solve this problem is to introduce a properly designed bending stiffener at the supports, as indicated in Figure 1.4. The purpose of a bending stiffener is to provide a gradually increase of the bending stiffness from the rather low value of the flexible riser to a significant higher value that can tolerate a rigid connection.

The primary design requirement of a bending stiffener is that the critical curvature is not exceeded during the lifetime of the riser. Secondly, the bending stiffener should be optimized to give minimum support forces, i.e. axial force, shear force and bending moment. Thus the length of the bending stiffener should be as small as possible. Procedures that can be used in order to meet the above design criteria are given by Sødahl [1.4]. As reported in [1.4], the curvature distribution along the bending stiffener in an extreme load condition, is characterized by high bending gradients. This is an important observation when dealing with stress analysis of the flexible riser armouring layers.

 ISBN 82-7119-427-5 ISSN 0802-3271

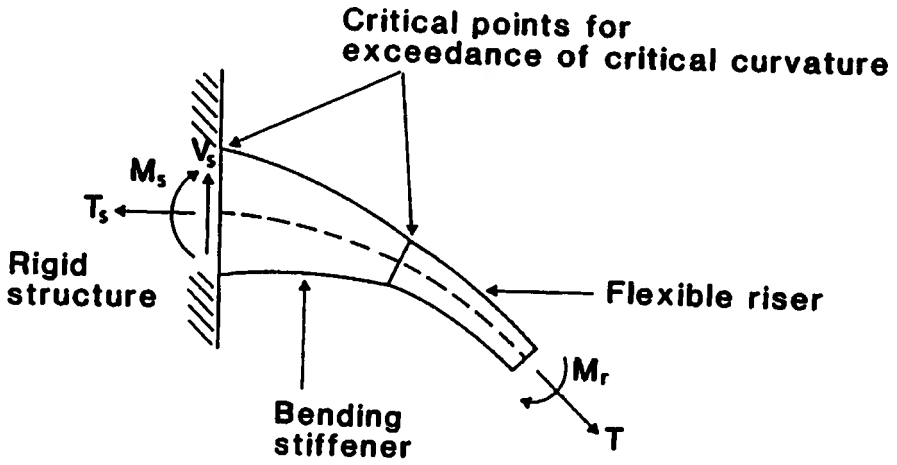

Figure 1.4 Bending stiffener

1.2 Design principles

The present work will focus on degradation due to fatigue and wear of flexible risers that are exposed to cyclic environmental loads under normal operating conditions. In the following, the design principles related to these degradation processes will be reviewed.

1.2.1 Load effects in flexible risers

Flexible risers are normally exposed to the following types of loading during operation:

- Deadweight
- Environmental loading
- Internal and external pressure
- Internal fluid flow

The deadweight will induce tension which normally has its maximum value at upper riser end. The tension force is carried mainly by the outer armouring layers in the cross section.

 ISBN 82-7119-427-5 ISSN 0802-3271

Offshore floating production systems are always exposed to environmental effects from wind, waves, and current. Waves and current will give hydrodynamic loads directly on the riser, but also loads induced by floater motions. Such forces give raise to variations in tension, torque and curvature along the flexible riser, normally with maximum values at the upper end. These variations will effect the plastic tubulars, outer armouring layers of the pipe structure and in particular the bending stiffener if present.

Hoop stresses from external and internal pressure are mainly carried by the carcass and the inner armouring layers of the flexible pipe structure, while axial stresses are mainly carried by the outer armouring layers.

1.2.2 Current design practice

Current practice for design of flexible pipes is based on an estimated extreme response using a safety format expressed by:

$$f_c = \frac{r_c}{s_f} \tag{1.1}$$

where f_c is the characteristic load effect in terms of cross sectional response and r_c is the characteristic capacity of the cross section for example the yield stress of the tendon material or the pipe critical radius of curvature. A safety factor s_f has been included in order to account for all kind of uncertainties involved in the design process of flexible risers, such as uncertainties in marine environment, loads, method of analysis, capacity etc..

The minimum safety factors recommended by guidelines issued by Det Norske Veritas (DNV) for flexible pipes are given in Table 1.1, confer Mo and Torset [1.5].

 ISBN 82-7119-427-5 ISSN 0802-3271

Table 1.1 DNV minimum safety factors for flexible pipes.

Load effect	Minimum safety factor
Internal pressure	2.0
External hydrostatic pressure	1.5
Axial force, tensile/compression	2.0
Torsion	2.0
Minimum radius of curvature	Static 1.25 Dynamic 1.5

The Guidelines also states that the service life of the armouring layers is influenced by wear, fretting, fretting corrosion and fatigue and that these effects must be taken into account in the design. Quantitative methods for predicting the service life are however not given.

The design principles for fatigue being reported by IFP/SINTEF in [1.6] and by Feret et. al. [1.7] are used as basis for the design of the *Coflexip* pipes. These principles are based on material aging of the plastic layers, wear in the armouring layers and non-exceedance of the endurance limit stress for the steel material used in the armouring. The flexible pipe is thus considered to fail, once the wear effect has reduced the thickness of the tendon cross section to such extent that stresses due to a certain design load exceeds a given value. This seems to be conservative, since a steel material normally can resist several fatigue cycles beyond the endurance limit.

The limiting stress is further taken from a Goodman line in a Haig's diagram, which expresses the endurance (or fatigue) limit stress as a function of the mean stress as shown in Figure 1.5.

 ISBN 82-7119-427-5 ISSN 0802-3271

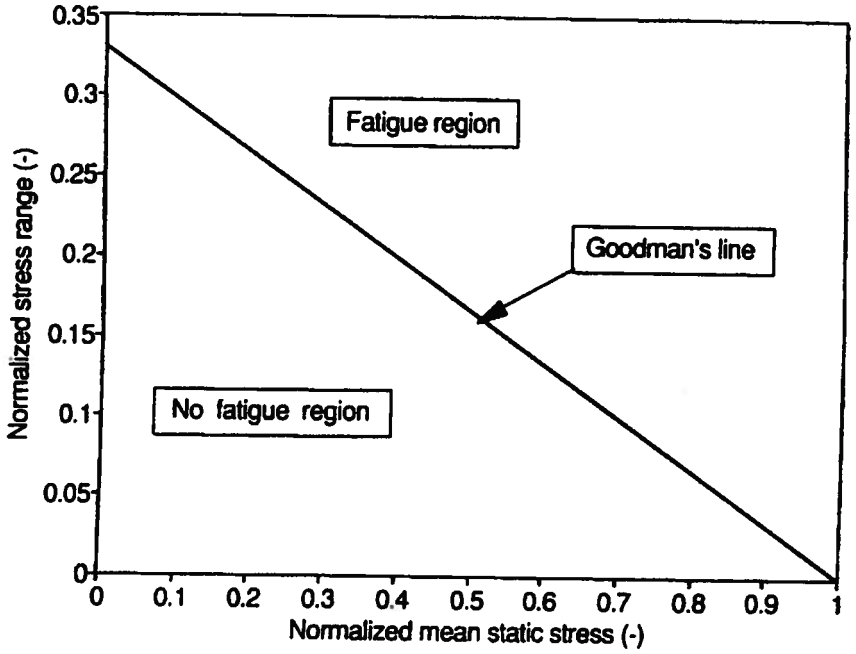

Figure 1.5 Haig's diagram

1.2.3 Procedures for estimation of lifetime extreme global response

The characteristic load effect is most commonly specified as the characteristic largest response maximum for a design lifetime of N_d years. A design lifetime of 100 years is used in most situations. Alternative procedures for estimating the lifetime extreme response are use of long term statistics, the design storm and the design wave approach, confer Larsen et. al. [1.8].

Use of long term statistics

Use of long term statistics in a complete and consistent way is unrealistic due to the large number of environmental parameters involved. In practice, a long term environmental description will only be available for waves in terms of a scatter diagram expressing the joint distribution of significant wave height H_s and spectrum peak period T_p. Realistic, but

conservative values have to be selected for other parameters like wave direction, type of wave spectrum, current profile and floater offset.

With these restrictions, the long term distribution of individual response maxima can be expressed as a weightened sum of short term distributions. For further details confer [1.8] and [1.9].

The long term approach is well established for linear structures, confer Haver [1.10]. Unfortunately, the situation is more complex for flexible risers because of important nonlinearities.

Methods for long term response statistics of nonlinear structures have been developed by Farnes [1.11] based on stochastic time domain analysis of a selected number of sea states and use of interpolation/extrapolation techniques.

Design storm approach

So far, the design storm approach is most commonly used for prediction of lifetime extreme response for offshore structures. A design storm can be defined by specifying values for all environmental parameters in a short term environmental condition, and a specified duration of the storm.

Response time histories are produced by a stochastic time domain simulation and the lifetime extreme responses are then estimated as the expected largest response maxima during the design storm.

One important problem with this approach is, however, that different types of responses will have their extreme values under different wave conditions, and that the duration of the design storm is difficult to determine in a consistent way.

This problem has been investigated by Larsen and Passano [1.12] where a method for selecting a design seastate based on an approximate long term distribution of the response was

presented. This distribution can be established from simplified frequency domain analyses using stochastic linearization of drag forces.

Design wave approach

The design wave approach means to estimate the lifetime extreme response by calculating the load effects from selected regular waves. A wave height of 100 year return period is typically used, and the wave period is given a reasonable variation. Selection of a regular wave to represent the lifetime extreme condition is however most uncertain for dynamically sensitive systems. This approach should therefore be used with care.

1.2.4 Procedures for fatigue estimation

By considering the experience with flexible risers so far, flexibles seem to have an adequate resistance with respect to metal fatigue. This indicates that the wear approach proposed in [1.6] is reasonable. The wear will be dominated by the contribution from long duration moderate seastates, where structural nonlinearites will be insignificant. This allows for use of long term statistics combined with frequency domain analyses including stochastic linearization of nonlinear drag forces. This approach has been verified by Leira and Olufsen [1.13].

Thus, flexible pipe design can be performed by a combination of frequency domain analyses in order to describe the wear, and time domain simulations in order to describe the extreme loads and curvatures.

 ISBN 82-7119-427-5 ISSN 0802-3271

1.3 Response analysis techniques

1.3.1 Global response analysis techniques

The static and dynamic behaviour in terms of global response parameters of any flexible riser system can be adequately analysed by a general purpose finite element method (FEM) computer program provided that the following features are included:

- Three-dimensional formulation
- Large rotations and displacements
- Nonlinear static analysis
- Time domain dynamic analysis
- Regular/irregular wave loading and floater motion
- Axial, bending and torsional stiffness including a nonlinear material description
- Geometric stiffness, i.e. the lateral stiffness contribution from the current axial force
- Modelling of seabed contact
- Structural damping formulation

In the design process of flexible risers, the situation is often that the generality offered by a general purpose FEM program is in conflict with the need for efficient and flexible computations and user-friendliness.

To meet these demands, several FEM computer programs tailored to practical design of flexible risers have been developed during the last years. A review of the most commonly used programs is given by Larsen [1.14] and Kodaissi et. al. [1.15].

In order to further improve the efficiency of the analysis, considerations of the flexible riser mechanics are valuable.

 ISBN 82-7119-427-5 ISSN 0802-3271

Principles for selecting response model

Bending stiffeners at the supports are crucial parts of flexible riser systems and must therefore be included in the design analyses.

Flexible riser systems are known to have a significant global dynamic response. Experiences from analyses of flexible riser systems have also shown that the global dynamic behaviour is very little affected by the bending stiffener [1.4]. The bending stiffener response is, however, locally dominated by quasi-static effects. These observations are important when selecting principles for efficient design analyses, and lead to the use of a combination of relative coarse global models for dynamic analyses and local refined quasi-static models using results from the global analyses as boundary conditions. Figure 1.6 illustrates the different models.

It has been shown by Sødahl [1.4] that by using the end force and force angle as boundary conditions, the combined model gives drastic reduction in computation time, without significant loss of accuracy.

For further details regarding use of the local and global models confer [1.4].

1.3.2 Analysis of cross sections

Behaviour of flexible pipe cross sections with respect to stresses an slip between components due to pressure, tension and torsion is relative well covered in the literature, confer [1.16]-[1.20]. Use can also be made of work done in comparable fields, e.g. reinforced cables [1.21]-[1.28] and wire ropes [1.29].

Pressure, tension and torque give axisymmetric behaviour of all components in the flexible pipe cross section allowing for a relatively simple mathematical description of the problem. Curved bar elements can be used to simulate the armouring layers and thin shell tubular elements can be used to describe the sheaths.

 ISBN 82-7119-427-5 ISSN 0802-3271

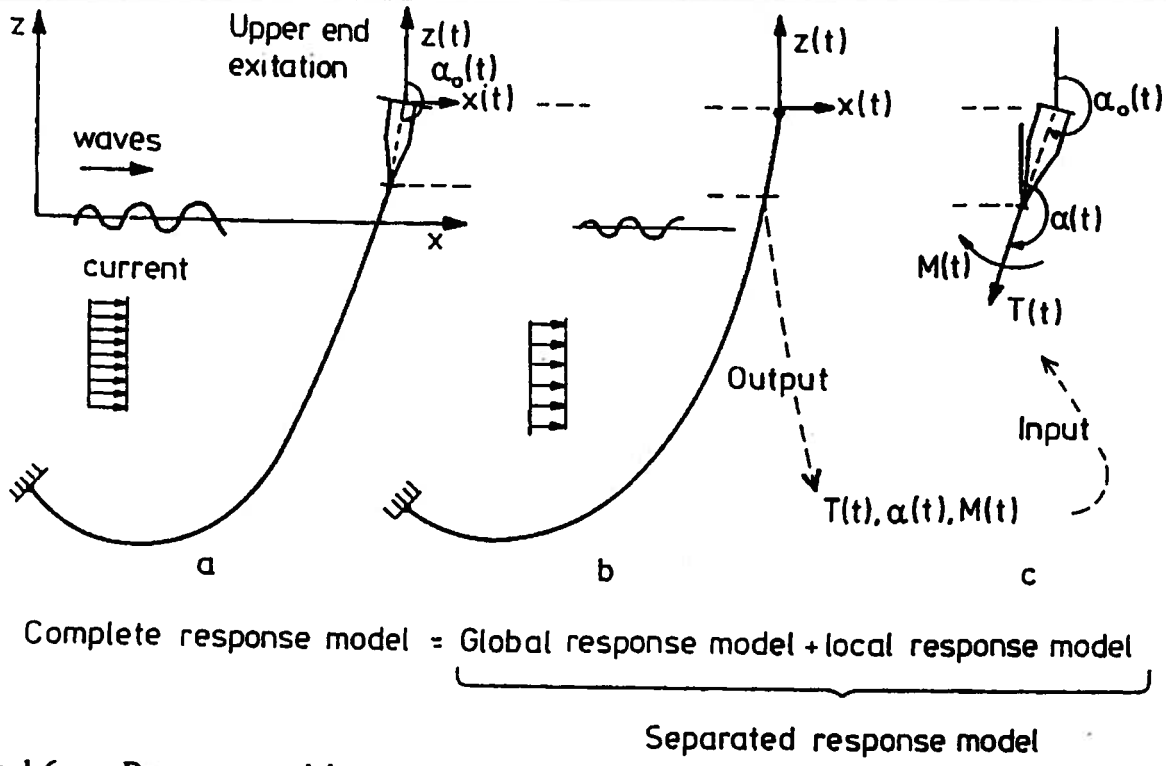

Figure 1.6 Response models

The response of flexible pipes subjected to bending is less focused on. Lutchansky [1.30] and Tan et. al. [1.31] allow axial movement of the helical reinforcing only. Feret and Bournazel [1.17] suggest that the nonbonded helically wound tendon will follow the geodesic of the curved cylinder. Leclair and Costello [1.32] use Love's equations and an assumed wire geometry to calculate the local and global response of wires in a bent rope.

The models presented in the literature so far are, however, based on the following assumptions/simplifications:

The curvature is assumed to be constant which means that harmonic mathematical functions can be used to represent the solution.

They do not consider the actual load effect induced by friction and contact forces on each tendon as the tendons are assumed to be described by a predefined curve.

They do not consider the effect of geometric stiffening of each tendon due to tension.

ISBN 82-7119-427-5 ISSN 0802-3271

All theories are based on analytical solutions which are unable to represent realistic boundary conditions from end restraints.

At the end termination each tendon is anchored and in this area high tension and significant curvature gradients will occur. It is thus clear that these models are inadequate for description of stresses and slip at riser terminations.

The main purpose of the present work has therefore been to formulate mathematical models that can describe stresses and slip of armouring tendons taking all the above mentioned effects into account.

1.4 Scope of work

From the previous discussion it is found that well established procedures and models are available for describing the global response of flexible risers, whereas little effort has been made to establish models of similar accuracy for describing the cross section response during bending. The overall purpose of this study has therefore been to improve existing methods for analysis of flexible pipe armouring layers and to contribute towards a better understanding of the behaviour of flexible pipes during bending. The aim is to create tools that can be used in practical design. The study will further focus on nonbonded pipes and concentrate on the stress and fatigue analysis of the end termination, i.e. in the bending stiffener region. The theories developed are, however, intended to be as general as possible, thus allowing the developed tools to be used for bonded pipes, umbilicals and other applications of flexible pipes as well.

A major part of this study deals with developing a theoretical model that is capable of simulating the behaviour of individual tendons exposed to an arbitrary curvature distribution. This *local* theoretical model is presented in Chapter 2.

In Chapter 3, the known fatigue mechanisms of nonbonded flexible pipes are discussed and available test data on primary parameters presented.

 ISBN 82-7119-427-5 ISSN 0802-3271

In Chapter 4, results are given from numerical studies using the local tendon model developed in Chapter 2. The purpose of these studies has been to verify the model and to investigate aspects of armouring tendon behaviour during bending. A study on the tendon behaviour in a 8-inch flexible riser during a design storm is included.

Chapter 5 presents a summary of the existing models for internal response analysis of flexible pipes subject to both axisymmetric loads and bending. A comparison is made between the results obtained from existing models and the results presented in Chapter 4 for the 8-inch riser. Some observations made in flexible pipe tests and the theory developed in Chapter 2 are further used in order to suggest improvements of existing models.

Chapter 6 focus on comparisons made between the developed model and results from experimental work carried out on full-scale test specimens.

 ISBN 82-7119-427-5 ISSN 0802-3271

2 A MODEL FOR THIN CURVED RODS SLIDING ON A CURVED CIRCULAR SURFACE

2.1 Introduction

The purpose of this chapter is to formulate a finite element model that is capable of finding stresses and slip during bending of flexible pipe armouring tendons taking all relevant effects into account. Among such effects are:

Pretension due to axisymmetric loading

Arbitrary curvature distribution

Interaction between one armouring layer and the other layers.

Initial stress stiffness

End restraint effects

It is obvious that in order to take all the above effects into account a discretization technique is needed. Further, in order to establish a model having the required capabilities, two strategies are possible:

 ISBN 82-7119-427-5 ISSN 0802-3271

1. Make a complete model of all the elements in the flexible pipe structure and then apply the external loads incrementally to obtain the true equilibrium state between internal and external forces.

2. Make a simplified model assuming the curvature distribution to be given from a separate design analysis and then consider each individual tendon.

For both strategies it is desirable to utilize the approach described in Sub-section 1.3.1 in order to minimize the number of degrees of freedom involved.

Following the idea of the first approach and use of the finite element technique, a finite element model for each individual tendon and tube layer is needed. As each layer interact with the surrounding layers, a nonlinear description is required, i.e. updating the equilibrium state in all elements at each load step. Numerical integration is further needed to calculate the overall cross section stress resultant to be used in the equilibrium control against external forces. The above described method would involve a large number of elements to model the needed part of the pipe and thus require large computer resources.

The method developed in this work has consequently been based on the second approach, where one individual tendon is analysed for a *given* curvature distribution along the pipe. This is based on two fundamental assumptions:

1. The bending stiffness induced due to local tendon behaviour at end restraints is at least one order of magnitude less than the effect of the total cross section bending stiffness. This is considered to be a reasonable assumption along the bending stiffener.

2. Each tendon behave independent of other tendons for the curvature range considered. This assumption is considered reasonable as long as the curvature is smaller than the critical curvature.

Accepting these assumptions it is possible to use results from differential geometry directly, thus reducing the number of unknowns needed to describe the tendon behaviour.

 ISBN 82-7119-427-5 ISSN 0802-3271

The finite element formulation has been based on the theory of thin curved rods. The earliest work on this subject can be traced back to Kirchoff [2.1] who studied the linear theory of slender curved rods. A brief survey on this theory is found in Love's text [2.2]. However, these references are limited to linear theory, while the nature of the present problem will lead to significant nonlinearities.

The nonlinear theory of curved rods was developed by Hay [2.3] and later generalized by Ericksen and Truesdell [2.4] and also Huang [2.5]. However, these formulations are not convenient for nonlinear finite element implementation since they do not explicitly express the nonlinear terms of the *Green strain tensor.* Washizu [2.6] used the Green strain tensor in order to obtain strain and stress measures in the linear case, but without looking at applications. The present work has been based on extending his formulation to include large displacements but small strains, and then use this theory to develop a tailor made curved beam element.

In the following, the term *rod* will be used when referring to one single armouring tendon. The term *pipe* further means the surrounding flexible pipe structure.

2.2 Fundamental concepts and assumptions

2.2.1 Coordinate systems. Concepts from differential geometry

The initial undeformed configuration of the rod's centre line is in the following assumed to be represented by a helix which is supported by a straight circular cylinder. The centre line of each rod therefore represent a curve on the cylinder surface making an angle α with the length coordinate w as shown in Figure 2.1. The supporting cylinder surface can be represented by the radius R and surface coordinates v and w. The coordinate curves on the surface are represented by setting v=*const.* and w=*const.* At the pipe centre line there is a fixed Cartesian coordinate system with axes Z^I and unit vectors $\boldsymbol{E}_I$. In the undeformed configuration or when the pipe is exposed to axisymmetric loading without deformations of

 ISBN 82-7119-427-5 ISSN 0802-3271

the cylinder, the Cartesian coordinates of a point on the surface can be expressed by cylindrical coordinates as:

$$Z^1 = w \tag{2.1}$$

$$Z^2 = R \cos v \tag{2.2}$$

$$Z^3 = R \sin v \tag{2.3}$$

When the cylinder is bent to a constant radius ρ, it is formed into a toroid, which may be described in spherical coordinates. The Cartesian coordinates of a point on the surface can be expressed by spherical coordinates as:

$$Z^1 = (\rho - R \cos v) \sin\phi \tag{2.4}$$

$$Z^2 = \rho - (\rho - R \cos v) \cos\phi \tag{2.5}$$

$$Z^3 = R \sin v \tag{2.6}$$

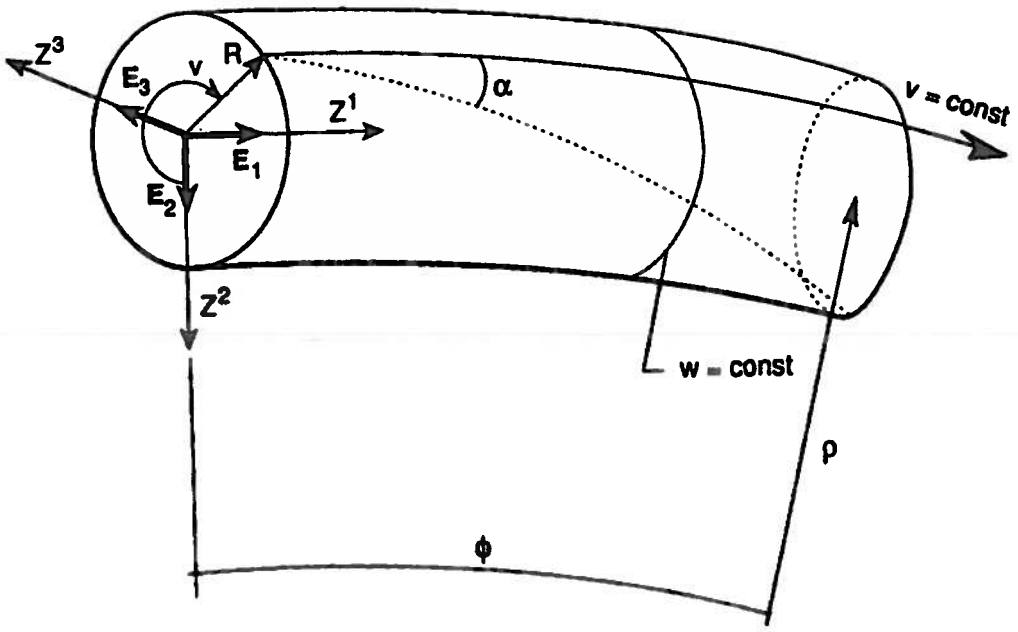

Figure 2.1 Definition of pipe centre line coordinate system and basic quantities

The cross section of the rod may in general be arbitrarily oriented relative to the centre line. The restraint is, however, introduced that the rod cross section principal axes are fixed to the

surface normal as shown in Figure 2.2. This restraint has been shown in Appendix A to be fulfilled when the rod is exposed to reasonably high tensile stresses, as during normal load condition of a flexible pipe. The fact that one layer is restrained by the next layer should, however, make this assumption reasonable even if compression occurs. It will be shown later that this assumption eliminates the need for a complete three-dimensional description of the rod .

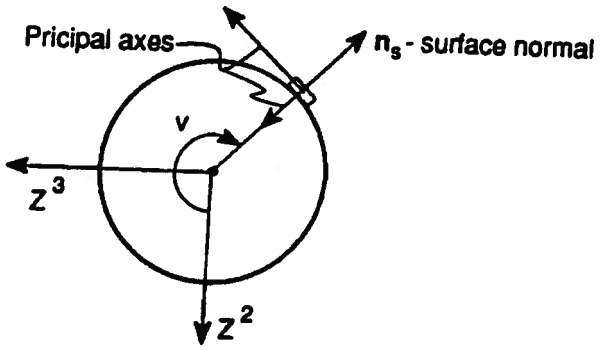

Figure 2.2 Orientation of cross section principal axes

By assuming that the position vector $\boldsymbol{R}_0$ describing any point on the centre line of the rod is a vector function of the arc length coordinate X^I and by using concepts from differential geometry, a system of local orthonormal axes is constructed at an arbitrary point P_0 having unit base vectors $\boldsymbol{I}_I$ as shown in Figure 2.3 a. These unit vectors are called the *tangent, normal and binormal vectors* and the associated coordinate axes represent the *principal torsion-flexure axes* along the curve. The vectors are determined by:

$$\boldsymbol{I}_1 = \boldsymbol{R}_{0,1} = Z^I_{,1}\, \boldsymbol{E}_I \tag{2.7}$$

$$\boldsymbol{I}_2 = \frac{1}{\kappa}\, \boldsymbol{R}_{0,11} = \frac{1}{\kappa}\, Z^I_{,11}\, \boldsymbol{E}_I \tag{2.8}$$

$$\boldsymbol{I}_3 = \boldsymbol{I}_1 \times \boldsymbol{I}_2 = \frac{1}{\kappa}\, e_{IJK}\, Z^I_{,1}\, Z^J_{,11}\, \boldsymbol{E}_K \tag{2.9}$$

where κ represents the principal curvature and e_{IJK} is the permutation symbol. The Seret-Frenet differential formula [2.7] is introduced to express the rotation of the local unit triad along an infinitesimal distance dX^I :

$$\begin{bmatrix} \frac{dI_1}{dX^1} \\ \frac{dI_2}{dX^1} \\ \frac{dI_3}{dX^1} \end{bmatrix} = \begin{bmatrix} 0 & \kappa & 0 \\ -\kappa & 0 & \tau \\ 0 & -\tau & 0 \end{bmatrix} \begin{bmatrix} I_1 \\ I_2 \\ I_3 \end{bmatrix} \tag{2.10}$$

It is noted that if these differentiations were made with respect to the fixed coordinate system Z^I, the derivation would generally involve *Christoffel symbols of second kind* [2.8]. However, as long as the differentiations are made with respect to the arc length coordinate X^I, these contributions are given directly from differential geometry.

The torsion τ and the principal curvature may be determined from the vectors directly as:

$$\tau = I_3 \cdot \frac{dI_2}{dX^1} \tag{2.11}$$

$$\kappa = I_2 \cdot \frac{dI_1}{dX^1} \tag{2.12}$$

which for a rod being wound into a circular helix gives:

$$\tau = \frac{\sin\alpha \cos\alpha}{R} \tag{2.13}$$

$$\kappa = \frac{\sin^2\alpha}{R} \tag{2.14}$$

 ISBN 82-7119-427-5 ISSN 0802-3271

where R is the layer radius.

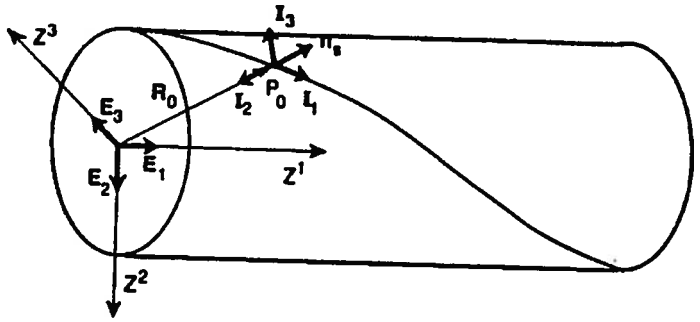

(a) The I_i system

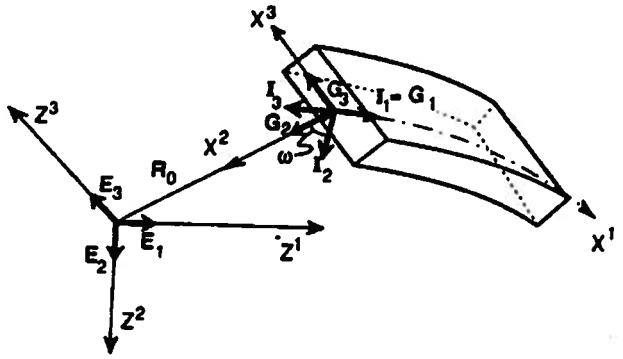

(b) G_i - systems relative orientation to I_i

Figure 2.3 Local curve coordinate systems

A new unit triad is introduced, defined by the base vectors G_I and coordinate axes X^I. This is oriented in such a way that G_1 is parallel to I_1, while G_2 is directed along the inwards surface normal and is thus fixed to the cross section principal axes. The binormal vector G_3 is determined by the orthonormality condition. From this definition of axes it is seen that the I_I-triad coincide with the G_I-triad of the cross section principal axes, only if the curve normal vector is parallel to the surface normal. The direction of the cross section axes may thus in general differ from the curve principal torsion-flexure axes. The angle ω is therefore introduced to define the orientation of the G_I system relative to the I_I system as shown in Figure 2.3 b. By defining the convention that the curvature components are positive when they give a positive rotation about the respective axes with increasing X^I and using the right hand rule, a generalized Seret-Frenet formula is obtained as:

 ISBN 82-7119-427-5 ISSN 0802-3271

$$\begin{bmatrix} \frac{dG_1}{dX^1} \\ \frac{dG_2}{dX^1} \\ \frac{dG_3}{dX^1} \end{bmatrix} = \begin{bmatrix} 0 & \kappa_3 & -\kappa_2 \\ -\kappa_3 & 0 & \kappa_1 \\ \kappa_2 & -\kappa_1 & 0 \end{bmatrix} \begin{bmatrix} G_1 \\ G_2 \\ G_3 \end{bmatrix} \tag{2.15}$$

where:

$$\kappa_1 = \tau + \frac{d\omega}{dX^1} \tag{2.16}$$

$$\kappa_2 = \kappa \sin\omega \tag{2.17}$$

$$\kappa_3 = \kappa \cos\omega \tag{2.18}$$

κ_2 and κ_3 represent the components of the principal curvature κ in the (X^1,X^3) and (X^1,X^2) planes respectively. τ represents the geometric torsion of the centre line curve of the rod and can be found from Eq.(2.11) directly. The second term of Eq.(2.16) represents the torsion of the cross section, induced by the fact that the cross section rotate relative to the torsion-flexure axes, and is determined by:

$$\omega = \tan^{-1}\frac{\kappa_2}{\kappa_3} \tag{2.19}$$

which by differentiation with respect to the arc length coordinate X^1 gives:

$$\frac{d\omega}{dX^1} = \frac{\kappa_{2,1}\kappa_3 - \kappa_2\kappa_{3,1}}{\kappa_2^2 + \kappa_3^2} \tag{2.20}$$

The torsion and curvature components may, however, also be obtained directly from the base vectors G_I (see Eq.(2.15)) as:

 ISBN 82-7119-427-5 ISSN 0802-3271

$$\kappa_1 = G_3 \cdot \frac{dG_2}{dX^1} \tag{2.21}$$

$$\kappa_2 = -G_3 \cdot \frac{dG_1}{dX^1} \tag{2.22}$$

$$\kappa_3 = G_2 \cdot \frac{dG_1}{dX^1} \tag{2.23}$$

Since G_1 coincide with I_1, it is concluded from Eq.(2.8) that the second term on the right hand side of Eq.(2.22) will represent the curve normal vector. Thus, since G_3 is based on the surface normal vector G_2, transverse curvature will only occur when the surface normal does not coincide with the curve normal, i.e. $\omega \neq 0$. In the next sub-section curves on a circular surface that have no transverse curvature will be described.

2.2.2 The geodesic

It is first noted that curves between two points in a two-dimensional plane and having transverse curvature can possibly not represent a minimum in arc length between the two points since they are not straight lines. Mathematically a minimum curve on a surface can be found by using the Lagrangian multiplier technique as shown in [2.9]:

$$F = \int_0^{X^1} \sqrt{G_1 \cdot G_1}\, dX^1 + \lambda\, S(Z^I) \tag{2.24}$$

where λ is the Lagrange multiplier. The above means:

Find the curve having minimum length under the constraint that the curve lays on the surface:

$$S\,(\,Z^1, Z^2, Z^3\,) = 0 \tag{2.25}$$

This gives the following three differential equations:

 ISBN 82-7119-427-5 ISSN 0802-3271

$$Z^1_{,11} + \lambda \frac{\partial S}{\partial Z^1} = 0 \tag{2.26}$$

$$Z^2_{,11} + \lambda \frac{\partial S}{\partial Z^2} = 0 \tag{2.27}$$

$$Z^3_{,11} + \lambda \frac{\partial S}{\partial Z^3} = 0 \tag{2.28}$$

From Eq.(2.8), it is seen that the first term in Eqs.(2.26)-(2.28) express the normal vector components of the curve. The second term represents the surface gradient, i.e. the surface normal vector components. Thus, if a minimum curve exists, the normal vector is parallel to the surface normal, and the curve has no transverse curvature. Between two sufficiently close points on the surface there is only one such curve, called the *geodesic* between the two points [2.7]. Along the geodesic, the G_I and I_I system coincide i.e $\omega = 0$, and the Seret-Frenet formula of Eq.(2.15) takes the form of Eq.(2.10).

It is easily shown that for the straight cylinder, the circular helix represents a geodesic. When the cylinder is bent, this will however change. When the pipe is bent by a constant radius, an approximate analytical description of the geodesic is found by using Eqs.(2.26)-(2.28) and the coordinate transformation defined by Eqs.(2.4)-(2.6). This gives a first order differential equation in the spherical coordinate ϕ (see Appendix A). The displacements relative to the supporting surface may be expressed as a function of R/ρ from the first term in a Taylor series expansion. The solution shows that both longitudinal and transverse slip relative to the supporting surface are needed in order to go towards the geodesic (confer Figure 2.4). This process also induces twist and changes in normal curvature along the curve. It has been shown by independent derivation (see Appendix A), that the analytical expressions describing the geodesic are identical to the results presented by Feret and Bournazel [1.17]. The displacements needed along the local curvilinear axes are obtained as:

 ISBN 82-7119-427-5 ISSN 0802-3271

$$u_1 = \frac{R^2}{\rho} \frac{\cos^2\alpha}{\sin\alpha} \sin v \tag{2.29}$$

$$u_3 = \frac{R^2}{\rho \tan\alpha} \left(2\sin\alpha + \frac{\cos^2\alpha}{\sin\alpha} \right) \sin v \tag{2.30}$$

The twist and normal curvature increment can be derived from Eq.(2.21) and Eq.(2.23) :

$$\Delta\kappa_1 = \frac{-\sin\alpha \cos\alpha}{\rho} \left(\frac{1}{\sin^2\alpha} - 3 \right) \cos v \tag{2.31}$$

$$\Delta\kappa_3 = -\frac{3 \cos^2\alpha}{\rho} \cos v \tag{2.32}$$

The physical interpretation of the solution is that in order to eliminate the large part of straining of the rod, a slip occur from the compressive side of the pipe to the tensile side. However, in order to eliminate the transverse curvature a transverse slip is additionally required as shown in Figure 2.4.

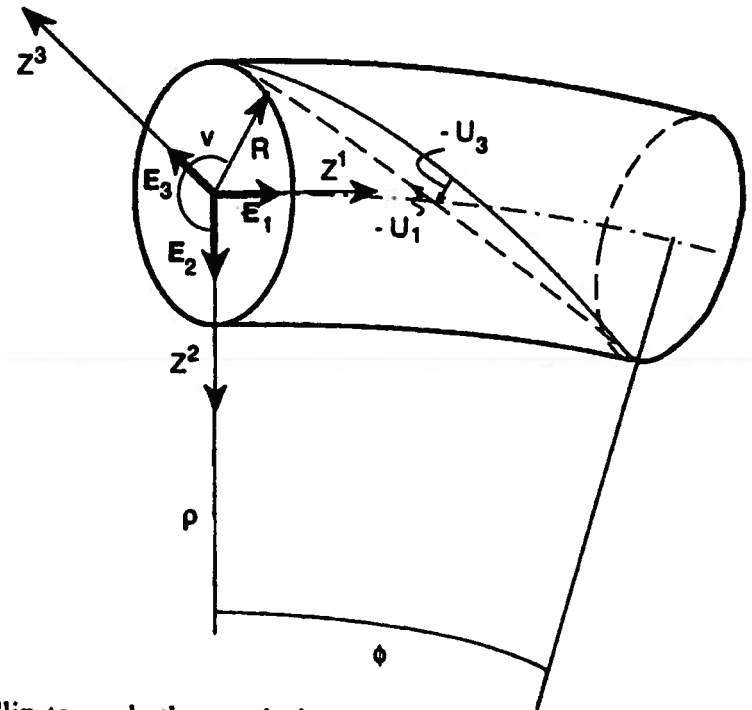

Figure 2.4 Slip towards the geodesic

 ISBN 82-7119-427-5 ISSN 0802-3271

The driving mechanism for the transverse movement of the rod towards the geodesic will be the bending moment about the X^2-axis created by transverse curvature and the transverse component induced by tension and transverse curvature in combination, the latter being the dominant one when the flexible pipe is in operation. Thus, by means of simple equilibrium consideration as visualized in Figure 2.5, transverse movements can only occur when the friction coefficient is less than:

$$\mu \leq \frac{\kappa_2}{\kappa_3} \tag{2.33}$$

The above equation, however, excludes consideration of interaction forces induced by surrounding layers and also the fact that the direction and value of the friction force will be controlled by coupling between the longitudinal and transverse displacements. Eq.(2.33) applies therefore only for outer armouring layer tendons not exposed to external pressure and the result will only represent an approximation.

The driving force inducing longitudinal movement will be the build-up of tensile and compressive stresses on the tensile and compressive sides of the pipe.

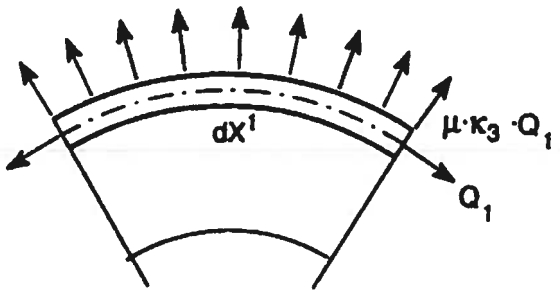

Figure 2.5 Transverse equilibrium consideration

 ISBN 82-7119-427-5 ISSN 0802-3271

2.2.3 Limit curves

It is obvious that both friction and cross section forces induced by the rod from twist and curvature increments will act against the movement of the rod towards the geodesic. It is convenient to define two ultimate limit curves. These are the *geodesic* to which the rod would naturally move if no friction or cross section restraint forces/moments occured, and the *loxodromic curve* which describes the rod under infinite friction and hence no slip. The loxodromic curve has the property that it intersects the coordinate curves of the surface by the constant initial lay angle. It is noted that axial strains in the rod may be eliminated along the loxodromic curve path, simply by feeding rod from the compressive side to the tensile side of the pipe. In order to eliminate the transverse curvature, however, an additional transverse movement is needed towards the geodesic.

The position of the loxodromic curve is fixed in the way that no transverse or longitudinal slip occur relative to the supporting surface. It is shown in Sub-section 2.4.6 that for a loxodromic curve on a toroid, the longitudinal strain, twist and curvature increments may be expressed on an explicit form. The parameters involved in the resulting equations are the lay angle, layer radius and the pipe global radius of curvature. Further, it is well known from beam theory that the curvature represents the highest order differential needed to describe the global pipe behaviour. Thus, by describing an arbitrarily curved circular surface by a finite number of toroids, each having constant curvature, it is possible to calculate the distribution of longitudinal straining, twist and curvature increments along the loxodromic curve of the surface. The basic idea utilized in the present formulation is based on first assuming that the centre line of the rod is directed along the loxodromic curve, then calculate the corresponding cross section forces and at last allow the rod to slide towards equilibrium under the action of equilibrium forces. In order to perform this operation, consistent strain and stress relations that connect one equilibrium state to another are needed. These are developed in Sections 2.4 and 2.5, together with closed form expressions for the longitudinal straining, twist and curvature increments along the loxodromic curve segments.

 ISBN 82-7119-427-5 ISSN 0802-3271

2.2.4 Kinematic restraints

In Sub-section 2.2.1 the rod cross section was assumed to be fixed to the surface normal. In addition the displacements of the supporting surface along the surface normal must be small. This means that the rod is forced to slide along the curvilinear axes X^1 and X^3 of the supporting cylinder surface as shown in Figure 2.6, thus eliminating the need for a full three-dimensional description.

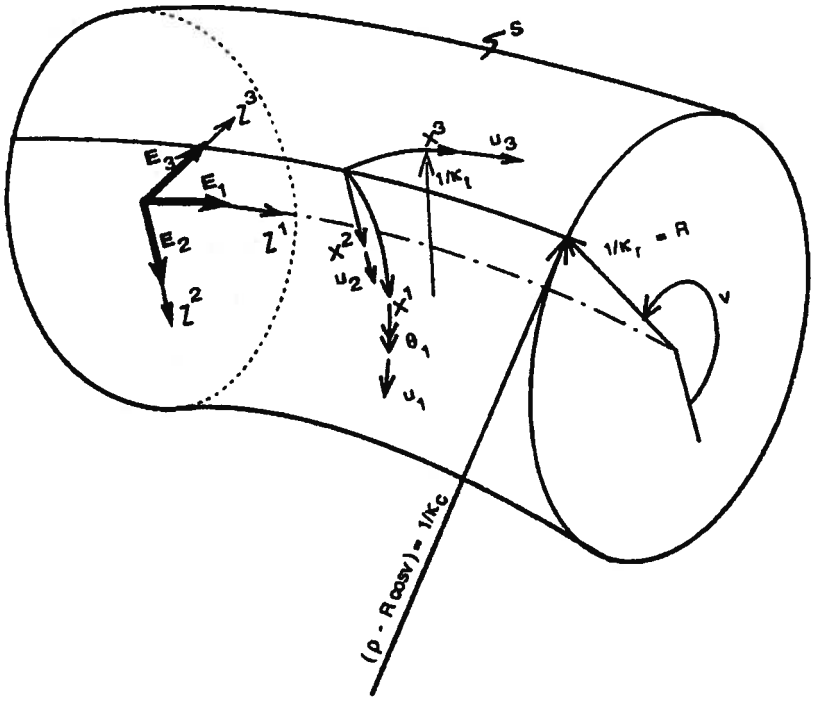

Figure 2.6 Restraint of the curvilinear plane

In order to ensure that the displacements occur along the curvilinear axes only, a restraint on the rotation θ_1 of the rod about the X^1 axis is introduced:

$$\theta_1 = - \kappa_t u_3 + \kappa_1 u_1 \tag{2.34}$$

where κ_t is the curvature along the transverse direction. This curvature can be obtained by the equation of Euler [2.7]:

 ISBN 82-7119-427-5 ISSN 0802-3271

$$\kappa_t = \cos^2\alpha\ \kappa_r + \sin^2\alpha\ \kappa_c \tag{2.35}$$

where κ_r and κ_c represent the principal curvatures in the circumferential and longitudinal directions of the surface.

2.3 Equilibrium equations

Figure 2.7 shows an infinitesimal element of the curved rod. Along the centre line there is a local coordinate system with axes X^I and base vectors G_I. These axes are fixed to the principal axes of the rod cross section. At the first end of the element there are stress resultants Q_I and M_I. These have changed to Q_I+dQ_I and M_I+dM_I at the second end.

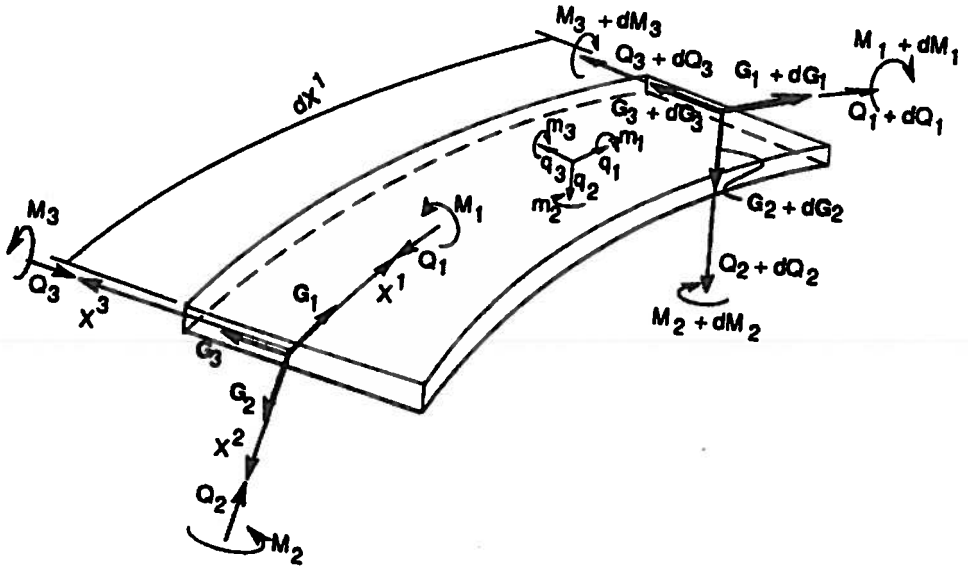

Figure 2.7 Curved infinitesimal beam element

Since the element is curved the unit coordinate system have similarly changed from G_I to G_I+dG_I. Along the element there are distributed loads and moments q_I and m_I. Consideration of force and moment equilibrium give:

$$Q_1 \frac{dG_1}{dX^1} + Q_2 \frac{dG_2}{dX^1} + Q_3 \frac{dG_3}{dX^1} + q_1 G_1 + q_2 G_2 + q_3 G_3 + \frac{dQ_1}{dX^1} G_1 + \frac{dQ_2}{dX^1} G_2 + \frac{dQ_3}{dX^1} G_3 = 0 \tag{2.36}$$

$$M_1 \frac{dG_1}{dX^1} + M_2 \frac{dG_2}{dX^1} + M_3 \frac{dG_3}{dX^1} + m_1 G_1 + m_2 G_2 + m_3 G_3 + Q_2 G_3 - Q_3 G_2 + \frac{dM_1}{dX^1} G_1 + \frac{dM_2}{dX^1} G_2 + \frac{dM_3}{dX^1} G_3 = 0 \tag{2.37}$$

The generalized Seret-Frenet formula from Eq.(2.15) is introduced and the following six coupled equilibrium equations are obtained:

$$\frac{dQ_1}{dX^1} - \kappa_3 Q_2 + \kappa_2 Q_3 + q_1 = 0 \tag{2.38}$$

$$\frac{dQ_2}{dX^1} + \kappa_3 Q_1 - \kappa_1 Q_3 + q_2 = 0 \tag{2.39}$$

$$\frac{dQ_3}{dX^1} - \kappa_2 Q_1 + \kappa_1 Q_2 + q_3 = 0 \tag{2.40}$$

$$\frac{dM_1}{dX^1} - \kappa_3 M_2 + \kappa_2 M_3 + m_1 = 0 \tag{2.41}$$

$$\frac{dM_2}{dX^1} + \kappa_3 M_1 - \kappa_1 M_3 - Q_3 + m_2 = 0 \tag{2.42}$$

$$\frac{dM_3}{dX^1} - \kappa_2 M_1 + \kappa_1 M_2 + Q_2 + m_3 = 0 \tag{2.43}$$

When the pipe is exposed to axisymmetric loading, simplifications can be made to solve these equations (see Chapter 5). For bending, analytical solutions may be obtained by assuming

 ISBN 82-7119-427-5 ISSN 0802-3271

constant bending radius [1.32]. For arbitrary curvature distribution, however, the finite element approach is needed, conveniently formulated through the Principle of Virtual Displacements.

2.4 Strain and deformation

2.4.1 Continuum concept

The adoption of the *continuum concept* implies that the molecular structure is disregarded. The material is assumed to be continuously distributed throughout its volume and to completely fill the space it occupies. This simplification means that all mathematical functions entering the theory are piecewise continuous in space and time.

2.4.2 Description of motion

The material particles of the rod occupy a region B having a volume V_0 and a surface S_0 in the initial state. A curvilinear coordinate system X^K with base vectors G_K is attached to each material particle P_0 along the centre line. The notation for direction of axes is based on concepts from differential geometry, assuming that the position vector R_0 extending from the origo of a Cartesian system Z^K to each material particle, is a vector function of the arc length coordinate X^1. The position vector of an arbitrary material particle P in the cross section of the rod can now be determined by:

$$R = R_0 + X^2 G_2 + X^3 G_3 \tag{2.44}$$

After deformation the volume V_0 and surface S_0 goes into a region b as shown in Figure 2.8 consisting of a spatial volume V and its surface S. The particle P_0 is now located at p_0. At p_0 there is a curvilinear coordinate system x^k with in the general case deformed base vectors g_k. The vector r_0 is the position vector of p_0. r is the corresponding position vector of p and is determined by:

 ISBN 82-7119-427-5 ISSN 0802-3271

$$r = r_0 + x^2 g_2 + x^3 g_3 \tag{2.45}$$

Basically, there are two descriptions of motions in common use. These are the *material* description and the *spatial* description. In the *material* or *Lagrangian* description the independent variables are the particle P and time t. The coordinates in the reference state, X^K, are called material or Lagrangian coordinates. In the *spatial* or *Euler* description attention is fixed to a given region in space instead of a particle in a continuum. Independent variables are the present time t and the present position x of a particle that occupied the point X at time $t=0$. The coordinates x^k in the current configuration are called spatial or Eulerian coordinates.

The material description is the most convenient and most frequently used description for continuums, and is therefore used as basis for this work.

The motion can be expressed in the Lagrangian description by:

$$x = x\,(X,t)\ ,\quad x^k = x^k\,(X^K,t) \tag{2.46}$$

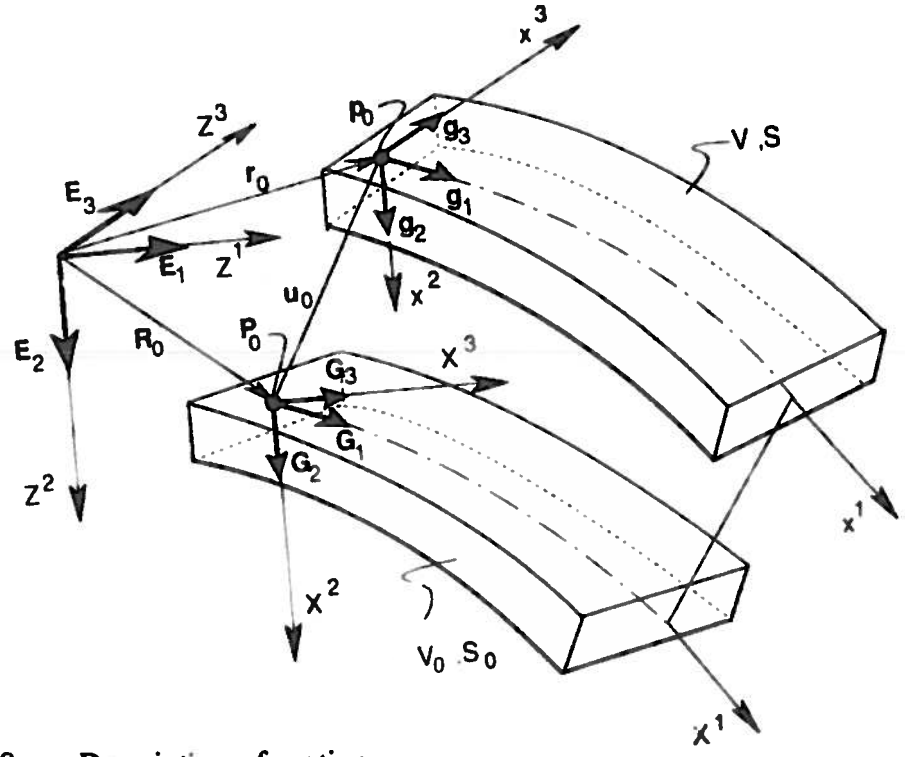

Figure 2.8 Description of motion

 ISBN 82-7119-427-5 ISSN 0802-3271

2.4.3 Green strain tensor in local curvilinear system

In the reference configuration an infinitesimal vector dR connecting two neighbouring material particles at P can be expressed as:

$$dR = \frac{\partial R}{\partial X^K} dX^K = G_K dX^K \tag{2.47}$$

In the deformed configuration the vector dr at p connecting the same material points, can be expressed by:

$$dr = \frac{\partial r}{\partial x^k} dx^k = g_k dx^k \tag{2.48}$$

G_K and g_k are the (covariant) base vectors at X^K and x^k, respectively. As G_K is defined through the relations given from differential geometry it represents an orthonormal system. It is in the following assumed that the deformations are so small that the change in surface and volume of the rod can be neglected. This means that the deformation of the base vectors G_2 in the radial direction and G_3 in the transverse direction are insignificant. Thus only longitudinal strains may influence base vector length. It is also assumed that the shear deformations of the thin and slender rod are sufficiently small to ensure that g_k is orthogonal.

The contravariant metric tensors are expressed as:

$$G^{KL} = G^K \cdot G^L \tag{2.49}$$

$$g^{kl} = g^k \cdot g^l \tag{2.50}$$

The corresponding covariant metric tensors are determined by:

$$G_{KL} \cdot G^{LM} = \delta_K^M \tag{2.51}$$

$$g_{kl} \cdot g^{lm} = \delta_k^m \tag{2.52}$$

where δ_k^m represents the Kroenecker delta, being 1 for equal indices and 0 else. G_{KL} is the covariant components of the metric tensor. The covariant components are given by:

$$G_{KL} = \begin{bmatrix} (1+X^3\kappa_2-X^2\kappa_3)^2+(X^3\kappa_1)^2+(X^2\kappa_1)^2 & -X^3\kappa_1 & X^2\kappa_1 \\ -X^3\kappa_1 & 1 & 0 \\ X^2\kappa_1 & 0 & 1 \end{bmatrix} \tag{2.53}$$

and the determinant, G as:

$$G = (1 + X^3\kappa_2 - X^2\kappa_3)^2 \tag{2.54}$$

Let dL be the length between two material points in the undeformed configuration and dl be the length between them in the deformed configuration. The difference of the squares of the line elements, containing the same material particles in the initial and deformed configuration, implies a length change due to deformation. If $dl^2 = dL^2$ for any pair of neighbouring material particles, the deformation has not changed the distance of the pair. The body has undergone a rigid body displacement if $dl^2 = dL^2$ for all material particles. Thus, the difference is a measure of the deformation produced during a displacement. For an infinitesimal element measured in the local curvilinear triad G_K

$$dl^2 - dL^2 = dr \cdot dr - dR \cdot dR = 2E^*_{KL} dX^K dX^L \tag{2.55}$$

where E^*_{KL} represents the Green's strain tensor defined in the local curvilinear system. The component form is given by:

$$E^*_{KL} = \frac{1}{2}\left(\frac{\partial r}{\partial X^K}\cdot\frac{\partial r}{\partial X^L} - \frac{\partial R}{\partial X^K}\cdot\frac{\partial R}{\partial X^L} \right) = \frac{1}{2}\left(g_{kl} - G_{KL} \right) \tag{2.56}$$

The components of the Green strain tensor in the local curvilinear system is now found by introducing:

$$r = R + u \tag{2.57}$$

and the Seret-Frenet formula from Eq.(2.15)

2.4.4 Transformation to local Cartesian coordinate system

Having in mind that the constitutive relations normally are given in Cartesian coordinates it is necessary to transform the curvilinear strain tensor to a Cartesian strain tensor. A local Cartesian coordinate system is therefore introduced with coordinate axes Y^I and unit vectors J_I, it's direction choosen to coincide with that of the G_I-triad. Then the following transformation is valid [2.8]:

$$E_{IJ} = \frac{\partial X^K}{\partial Y^I}\frac{\partial X^L}{\partial Y^J} E^*_{KL} \tag{2.58}$$

where E_{IJ} represents the Green strain tensor components in the local Cartesian coordinate system, and

$$\frac{\partial X^K}{\partial Y^I} = G^{KM}\left(J_I \cdot \frac{\partial r}{\partial X^M} \right) \tag{2.59}$$

$$\frac{\partial X^L}{\partial Y^J} = G^{LN}\left(J_J \cdot \frac{\partial r}{\partial X^N} \right) \tag{2.60}$$

It is noted that the same transformation equations are valid between stresses in the two coordinate systems

2.4.5 Description of volume

Since the strains considered in the present theory are assumed to be small, there will be no significant volume or area change during deformation. Thus the integrations to be performed in the virtual work equations can be performed with reference to the initial volume and area. However, the fact that the theory is developed in a curvilinear system, is considered.

The volume of an infinitesimal parallelepiped enclosed by the six surfaces X^I = constant and X^I+dX^I = constant, as shown in Figure 2.9, is found by using the triple vector product as:

$$\begin{aligned} dV_0 &= dX^1\, G_1 \cdot (\, dX^2\, G_2 \times dX^3\, G_3\,) \\ &= \sqrt{G}\; dX^1\, dX^2\, dX^3 \end{aligned} \tag{2.61}$$

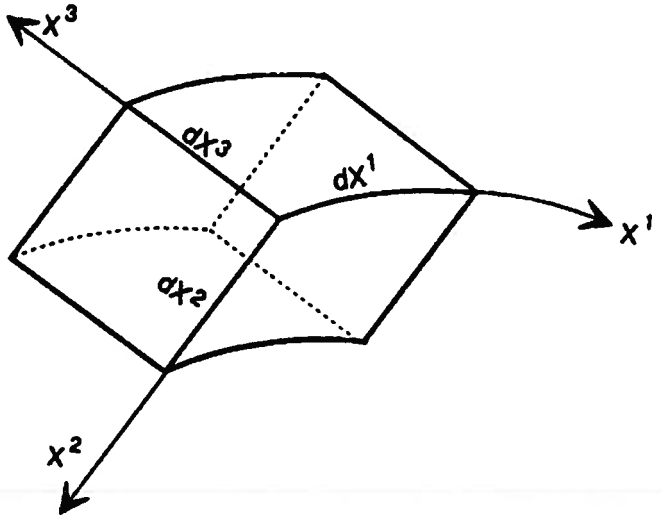

Figure 2.9 Infinitesimal volume element

2.4.6 Strain and curvatures along the loxodromic curve

For the *loxodromic* surface curve on a constantly curved pipe with global radius ρ, the longitudinal component of the Green strain tensor is determined by Eq.(2.56) (see Appendix B) as:

$$E_{11}^{*0} = -(\frac{R}{\rho})\cos^2\alpha\cos\nu + \frac{1}{2}(\frac{R}{\rho})^2\cos^2\alpha\cos^2\nu \tag{2.62}$$

This strain imply that the length of g_1 has been changed compared to G_1 and the deformed triad is no longer orthonormal. For later convenience it is desirable to express the curvature components with reference to the initial undeformed configuration. The following length correction is therefore introduced before determination of the curvature components:

$$G_1 = \frac{g_1}{\sqrt{1+2E_{11}^{*0}}} \approx \frac{g_1}{1+\varepsilon_{11}^{*0}} \tag{2.63}$$

where ε_{11}^{*0} is the component of natural longitudinal strain along the centre line referred to the local curvilinear coordinate system. In Sub-section 2.2.2 it was stated that there is only one curve between two sufficiently close points on a surface where the curve normal vector coincide with the surface normal, namely the geodesic, which also gave the shortest length between the two points. It was further shown that in order to follow such a curve during bending, a certain slip was required relative to a virtual restrained line intersecting the surface coordinate curves by a constant angle α. Thus, for the loxodromic curve, the curve normal will not be parallel to the surface normal, which again imply that transverse curvature will occur.

By using Eqs.(2.21)-(2.23), the following results are obtained for the twist and curvature increments (see Appendix B):

$$\Delta\kappa_1 = \frac{\sin\alpha\cos\alpha}{\rho}\cos^2\alpha\cos\nu \tag{2.64}$$

$$\Delta\kappa_2 = -\frac{\cos\alpha}{\rho}(1+\sin^2\alpha)\sin\nu \tag{2.65}$$

$$\Delta\kappa_3 = -\frac{\cos^2\alpha}{\rho}\cos^2\alpha\cos\nu \tag{2.66}$$

It is seen that the twist is purely due to the strain correction given in Eq.(2.63)

Further, by double differentiation of the transverse displacement of Eq.(2.30) with respect to the arc length coordinate X^1, the same result as Eq.(2.65) is obtained. This means that the transverse curvature is eliminated by the sideways displacement needed to reach the geodesic, which confirms the physical interpretation of the transverse slip given in Sub-section 2.2.2.

The transverse curvature is caused by two effects. The first effect, reflected in the first term of Eq.(2.65) is due to the fact that the global curvature can be decomposed directly into a line segment with an angle α to the longitudinal pipe axis. The other term is due to the straining of the supporting toroid, giving strain induced displacement not only in the longitudinal direction but also in the transverse direction.

The change in normal curvature is both due to straining of the rod and global curvature.

By introducing Eq.(2.14), Eq.(2.32) and Eq.(2.65) in Eq.(2.20) and then add the result obtained from Eq.(2.11), the final result will be according to Eq.(2.16). This result is further found to be the same as obtained by using the $G_\Gamma$triad directly in Eq.(2.21). This confirms the statement made regarding the physical interpretation of Eq.(2.16) given in Sub-section 2.2.1 (see Appendix B).

2.5 Strain and stress relations

2.5.1 The Green strain tensor in the local Cartesian coordinate system

In the following it is assumed that the equilibrium state of the rod can be described in terms of axial strains, bending and twist. Thus the deformation of an arbitrary point P in the rod can be expressed as:

 ISBN 82-7119-427-5 ISSN 0802-3271

$$u = u_1 G_1 + u_2 G_2 + u_3 G_3 \tag{2.67}$$

$$u_1 = u_1^0(X^1) + X^3\theta_2(X^1) - X^2\theta_3(X^1) + \beta(X^1)\varphi(X^2,X^3) \tag{2.68}$$

$$u_2 = u_2^0(X^1) - X^3\theta_1(X^1) \tag{2.69}$$

$$u_3 = u_3^0(X^1) + X^2\theta_1(X^1) \tag{2.70}$$

where u_i is the displacement components along the respective local curvilinear axes and θ_i the rotation components about the respective axes. $\varphi(X^2,X^3)$ represents the warping function of Saint-Venant's torsion, fulfilling the boundary conditions set by the cross section shape. According to the Saint-Venant's theory for straight beams exposed to a constant torque, the twist β is equal to $\theta_{1,1} = const.$ However, in this case the twist expression is not obvious, and β is therefore initially assumed to be an arbitrary function of X^1.

By using Eq.(2.15) and Eqs.(2.56-2.60) and neglecting insignificant 2nd order terms, the Green strain tensor measured in the local Cartesian coordinate system is found as:

$$GE_{11} = \sqrt{G}\,(\varepsilon_1 + X^3\omega_2 - X^2\omega_3 + \varphi\beta_{,1} + \kappa_1\beta[X^3\varphi_{,2} - X^2\varphi_{,3}]) + \frac{1}{2}\varepsilon_1^2 + \frac{1}{2}\varepsilon_2^2 + \frac{1}{2}\varepsilon_3^2 \tag{2.71}$$

$$2\sqrt{G}\,E_{12} = \varepsilon_2 - \theta_3 - X^3\omega_1 + \beta\,[\sqrt{G}\,\varphi_{,2} + \kappa_3\varphi] \tag{2.72}$$

$$2\sqrt{G}\,E_{13} = \varepsilon_3 + \theta_2 + X^2\omega_1 + \beta\,[\sqrt{G}\,\varphi_{,3} - \kappa_2\varphi] \tag{2.73}$$

where:

$$\varepsilon_1 = u_{1,1}^0 - \kappa_3 u_2^0 + \kappa_2 u_3^0 \tag{2.74}$$

$$\varepsilon_2 = u_{2,1}^0 + \kappa_3 u_1^0 - \kappa_1 u_3^0 \tag{2.75}$$

$$\varepsilon_3 = u_{3,1}^0 - \kappa_2 u_1^0 + \kappa_1 u_2^0 \tag{2.76}$$

$$\omega_1 = \theta_{1,1} - \kappa_3\theta_2 + \kappa_2\theta_3 \tag{2.77}$$

$$\omega_2 = \theta_{2,1} + \kappa_3\theta_1 - \kappa_1\theta_3 \tag{2.78}$$

$$\omega_3 = \theta_{3,1} - \kappa_2\theta_1 + \kappa_1\theta_2 \tag{2.79}$$

2.5.2 Constitutive relation in the Cartesian system

For an isotropic elastic material, the Hooke's material law is assumed:

$$\sigma^{11} = C_\sigma \varepsilon_{11} \tag{2.80}$$

$$\sigma^{13} = 2C_\tau \varepsilon_{13} \tag{2.81}$$

$$\sigma^{12} = 2C_\tau \varepsilon_{12} \tag{2.82}$$

C_σ is the Young's modulus of elasticity and C_τ is the shear modulus. σ^{22},σ^{33} are assumed to be constants given from axisymmetric analyses and σ^{23} are set to zero as it is assumed that there is no restraint present in the transverse direction and that the rod is thin.

2.5.3 Stress relations obtained by the Principle of Virtual Displacements

Variation techniques play an important role in continuum mechanics. One of the most frequently used, is the *Principle of Virtual Displacement*, or *the Principle of Virtual Work*. The principle is not a real energy principle, since the computed work is a fictious work done by a set of (statically admissible) forces and stresses on a set of kinematically admissible displacements and strains. The stresses and displacements need not be the actual distribution in the deformed body, and they may be independently prescribed. The major point is, however, to in average fulfill the differential equation for the problem by weight function multiplication and volume integration, instead of finding the exact solution. By prescribing that the external work equals the internal work it is provided that the error made by the assumed weight function in the external work equation equals the corresponding error coming from the internal work equation. If the weight functions are selected such that the appropriate boundary conditions are fulfilled, the error in the external work equation is eliminated and a state of *integrated equilibrium* is obtained. This means that in average for the total volume of integration, the error is zero. However, at an arbitrary point within the volume, the differential equation is not necessarily fulfilled.

 ISBN 82-7119-427-5 ISSN 0802-3271

Excluding volume forces, the principle of virtual work in an arbitrary equilibrium state reads:

$$\int_V \sigma:\delta\mathbf{e}\,\sqrt{G}\,dX^1dX^2dX^3 - \int_S \mathbf{t}\cdot\delta\mathbf{u}dS = 0 \tag{2.83}$$

In order to obtain the stress relations it is further assumed that the difference between two neighbouring equilibrium states is sufficiently small to neglect the second order terms of Eq.(2.71). The following assumptions are further made:

1. $\sqrt{G} \approx 1$ (2.84)

2. $\varphi(X^2,X^3) = -\varphi(-X^2,X^3) = -\varphi(X^2,-X^3)$ (2.85)

The first assumption imply that the rod is thin in the sense that the cross section width is small compared to the characteristic curvature. For the present application of the theory this gives by use of Eq.(2.54) a typical deviation less than 0.5 % from the exact solution.

The second assumption states that only double symmetric cross sections are considered.

By making use of Eqs.(2.71)-(2.79), and introducing ε_1, ε_2, ε_3, ω_1, ω_2, ω_3 and β as virtual quantities together with the material laws of Eqs.(2.80)-(2.82), the internal virtual work is obtained as:

$$\begin{aligned} W_i = &\int_0^l Q_1\delta\varepsilon_1 dX_1 + C_\sigma D\kappa_1\int_0^l \varepsilon_1\delta\omega_1 dX^1 - C_\sigma\Gamma\int_0^l \omega_{1,11}\delta\omega_1 dX^1 \\ &+ \int_0^l Q_2\delta(\varepsilon_2-\theta_3)dX^1 + \int_0^l Q_3\delta(\varepsilon_3+\theta_2)dX^1 \\ &+ \int_0^l M_1\delta\omega_1 dX^1 + \int_0^l M_2\delta\omega_2 dX^1 + \int_0^l M_3\delta\omega_3 dX^1 \end{aligned} \tag{2.86}$$

with stress resultants defined by:

$$Q_1 = C_\sigma A\varepsilon_1 + C_\sigma D\kappa_1\beta \tag{2.87}$$

$$Q_2 = C_\tau A(\varepsilon_2 - \theta_3) \tag{2.88}$$

$$Q_3 = C_\tau A(\varepsilon_3 + \theta_2) \tag{2.89}$$

$$M_1 = C_\tau I_t\beta + C_\tau I_p(\omega_1 - \beta) \tag{2.90}$$

$$M_2 = C_\sigma I_2\omega_2 \tag{2.91}$$

$$M_3 = C_\sigma I_3\omega_3 \tag{2.92}$$

Q_I represents the force along axes Y^I, and M_I the moments acting about the respective axes Y^I. A is the area of the cross section, D, Γ, I_t, I_p are torsion constants defined in the next section and I_2, I_3 are inertia moments about the respective cross section axes.

In Sub-section 2.4.3 the assumption of neglecting shear deformations was stated. From Eq.(2.88) and Eq.(2.89) it is seen that this assumption gives:

$$\theta_2 = -\varepsilon_3 \tag{2.93}$$

$$\theta_3 = \varepsilon_2 \tag{2.94}$$

Thus the rotations about the X^2- and X^3-axes are uniquely defined by the centre line displacement field only. Q_2 and Q_3 have to be found from equilibrium considerations and can not be found from the displacement state. This is a basic property of traditional Euler-Bernoulli beam theory.

The above also imply that the two last nonlinear terms of Eq.(2.71) represents the axial strains of the centre line due to centre line rotation, which is in accordance with the results obtained from nonlinear theory of straight beams [2.10].

An important observation is that by introducing the kinematic restraint of Eq.(2.34) together with the restraints of Eq.(2.93) and Eq.(2.94), all rotations can be described by means of the centre line displacement field of the rod alone.

 ISBN 82-7119-427-5 ISSN 0802-3271

By regarding the definitions in Eqs.(2.74)-(2.79) and Eqs.(2.87)-(2.94), the physical interpretation of the strain expressions are :

ε_1 represents the longitudinal straining of the centre line due to longitudinal, radial and transverse displacements.

ε_2 and ε_3 represent the rotation of the centre line.

ω_1 is the effective torsion deformation, i.e. twist corrected for the effect of curvatures along X^1.

ω_2 is the effective transverse curvature deformation corrected for the effect of torsion and curvature along X^1.

ω_3 is the effective normal curvature deformation corrected for the effect of torsion and curvature along X^1.

It is seen that by setting ω_1 equal to β in Eq.(2.90), the well known relation between the twist and the torsion constant for cylindrical shafts having constant twist and without end section warping restraint, is obtained. Since the armouring tendons are long and slender the assumption is introduced that:

$$\beta = \omega_1 \tag{2.95}$$

Based on the above interpretations, the following relations for the incremental change in twist and curvature deformations between two equilibrium states are obtained:

$$\Delta\kappa_i = \Delta\omega_i \tag{2.96}$$

It has been verified that by adding the increments in twist and curvature obtained by inserting the displacements from Eq.(2.29) and Eq.(2.30) for the geodesic into Eqs.(2.77)-(2.79), to the

curvature increments obtained by Eq.(2.31) and Eq.(2.32), the same result in total incremental twist and curvature is obtained as the result of Eqs.(2.64)-(2.66) (see Appendix B). This shows that the expressions for curvature and twist increments are capable of describing the kinematics of the problem correctly, and that the physical interpretation of them is correctly understood.

2.6 Incremental form of the Principle of Virtual Displacements

In finite element analysis of large deformation problems in solid mechanics, there are two different formulations widely used. These are the Total Lagrangian (TL) and the Updated Lagrangian (UL) formulations. The difference between them is the choice of reference configuration. In a TL formulation, all static and kinematic variables are referred back to the initial (C^0) configuration, while in the UL formulation these are referred to the last obtained equilibrium configuration, i.e. the current (C^n) configuration. Both formulations have been successfully used in many nonlinear problems, see e.g. [2.11]-[2.18]. Note that the formulations are theoretically equivalent if no approximations are introduced.

Several variations of the TL- and UL-formulations have been developed to improve the computational efficiency. The basic idea is to separate the rigid body motion from the local or relative deformation of the element. This is done by attaching a local coordinate system to the element and letting it continuously translate and rotate with the element during deformation. The nonlinearities arising from large displacements can be separated from the nonlinearities within the element. Several terms have been introduced to lable various formulations. Examples of names are 'Co-rotational formulation' and 'Co-rotated ghost reference' formulation.

In the Total Lagrange formulation, the kinematic and static quantities have to be referred back to the initial configuration. Since one basic idea of the present formulation is to operate on the supporting pipe surface, the initial coordinate system would be defined from the initial circular helix. As the supporting pipe structure is deformed, the only realization of the initial coordinate system on the new surface must be based on the corresponding geodesic, thus

 ISBN 82-7119-427-5 ISSN 0802-3271

involving deformation of the reference system itself. This excludes use of the Total-Lagrangian formulation in this case, leaving the UL and Co-rotated formulations as the remaining alternatives.

The present work has been based on the UL-formulation. In the UL-formulation the last obtained reference configuration is adequately described by the current torsion and curvatures. Since the loads are obtained on the basis of closed form expressions given as functions of the global curvature distribution, and the quantities of interest are rod stresses and displacements, there is no need for a fixed coordinate system. This means that for the present formulation, no congruence transformations are needed.

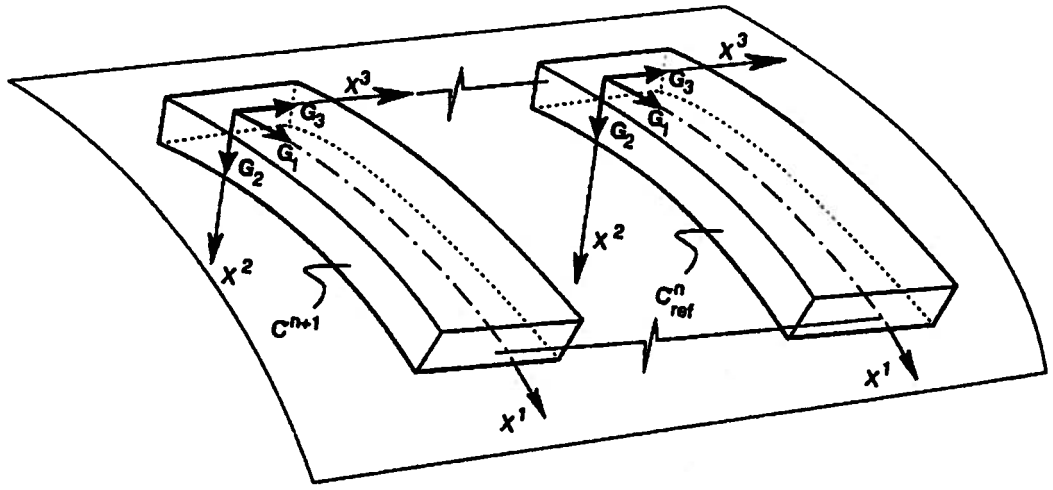

Figure 2.10 Reference systems in two neighbouring configurations

It is noted that since the derivation of the prescribed strain, torsion and curvatures have been based on a constant length of the tangential base vector, the present formulation represent a slight modification to the traditional UL-formulation. The effect of this modification is, however, small as the resulting strains are small in this case.

In the Updated Lagrangian formulation, the equation of incremental stiffness is obtained by making use of Eq.(2.83) and study the virtual work in an infinitesimal increment Δ as follows:

$$\int_V C:(\varepsilon+\Delta E):\delta(\varepsilon+\Delta E)dV - \int_S (t+\Delta t)\cdot\delta u dS = 0 \tag{2.97}$$

By subtracting Eq.(2.83) from Eq.(2.97), neglecting higher order terms in Δ and by assuming that the difference between two neighbouring equilibrium states is small, the following expression is obtained:

$$\int_V C:\Delta\varepsilon:\delta\varepsilon dV + \int_V \sigma:\delta\Delta E dV - \int_S \Delta t dS = 0 \tag{2.98}$$

Eq.(2.98) gives the incremental equilibrium equation to be used as basis for the stiffness matrix. The first term gives the material stiffness matrix, whereas the second term gives the geometric or more correctly, the initial stress stiffness matrix. These two internal work terms are determined as:

$$\begin{aligned} W_i^M = {} & C_\sigma A\int_0^l \Delta e_1\delta e_1 dX_1 + C_\sigma D\kappa_1\int_0^l (\Delta\kappa_1\delta e_1+\Delta e_1\delta\omega_1)dX^1 - C_\sigma\Gamma\int_0^l \Delta\kappa_{1,11}\delta\omega_1 dX^1 \\ & + (C_\tau I_t + C_\sigma\kappa_1^2 K_1 - C_\tau D + C_\tau\Gamma\kappa^2 + C_\tau K_2)\int_0^l \Delta\kappa_1\delta\omega_1 dX^1 \\ & + C_\sigma I_2\int_0^l \Delta\kappa_2\delta\omega_2 dX^1 + C_\sigma I_3\int_0^l \Delta\kappa_3\delta\omega_3 dX^1 \end{aligned} \tag{2.99}$$

$$W_i^G = Q_1\int_0^l (\Delta e_1\delta e_1 + \Delta e_2\delta e_2 + \Delta e_3\delta e_3)dX^1 \tag{2.100}$$

where D, Γ, K_1 and K_2 are cross section constants determined by:

$$D = I_p - I_t = I_2+I_3 - \int_s \varphi_{,2}X^3-\varphi_{,3}X^2+X^2X^2+X^3X^3 dS \tag{2.101}$$

$$K_1 = \int_S (X^3\varphi_{,2}-X^2\varphi_{,3})^2 dS \tag{2.102}$$

$$\Gamma = \int_S \varphi^2 dS \tag{2.103}$$

$$K_2 = \int_S \varphi_{,2}^2 + \varphi_{,3}^2 dS \tag{2.104}$$

The warping function for rectangular cross sections reads [2.2]:

$$\varphi = -X^3X^2 + b^2\left(\frac{2}{\pi}\right)^3 \sum_{n=0}^{\infty} \frac{(-1)^n}{(2n+1)^3} \frac{\sinh\left(\frac{2n+1}{b}\pi X^3\right)}{\cosh\left(\frac{2n+1}{2b}\pi a\right)} \sin\left(\frac{2n+1}{b}\pi X^2\right) \tag{2.105}$$

where the different parameters are defined in Figure 2.11.

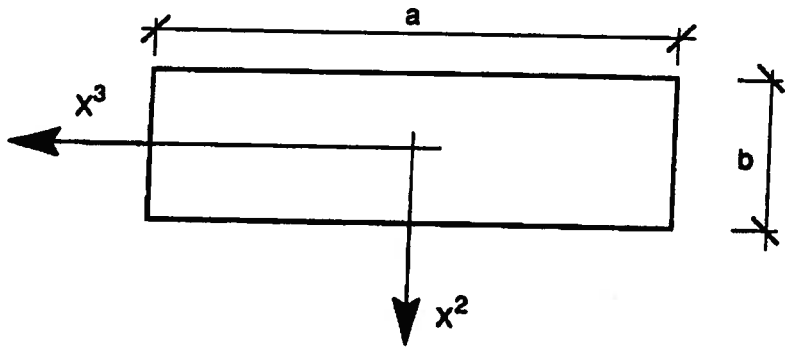

Figure 2.11 Definition of cross section parameters

The cross section constants defined by Eqs.(2.101)-(2.104) have been obtained by using the warping function defined by Eq.(2.105) and numerical integration. By investigating the different contributions to the fourth term of Eq.(2.99) it was found that the total sum was approximately equal to $C_\tau I_t$, which is the well known torsion constant.

The third integral of Eq.(2.99) gives further an asymmetric contribution to the material stiffness matrix. This contribution is however small and is neglected in order to obtain symmetric equations. The term is, however, included in the total virtual work equation and is thus being part of the equilibrium iterations.

2.7 Finite element implementation

2.7.1 Finite element discretization

The restraint introduced in Sub-section 2.2.4 imply that the rod is forced to slide on the supporting surface. This means that all deformations are going to take place on the supporting pipe surface. Consequently there should be three degrees of freedom at each nodal point as in Cartesian coordinates.

There are, however, basically three translation and three rotation degrees of freedom. In order to describe the transverse displacement state on the surface, two independent parameters are needed in each nodal point. The restraint introduced in Sub-section 2.2.4 on the rotation about the X^1-axis ensure that the rotation about the surface normal in one node of an element gives transverse displacement along the supporting surface only. Introducing the translation along the X^1-axis, the rotation about the X^3-axis and the translation along the X^2-axis thus make the difference between the present formulation and a two-dimensional description. In order to implement the rod/pipe interaction as far as contact forces are concerned, the translation degree of freedom along the X^2-axis is needed. The component of rotation about X^3 can, however, be neglected since the radial displacement is assumed to be small, i.e. the form of the supporting cylinder will remain smooth without undulations throughout subsequent deformation. Thus, the rotation about the X^3-axis is given by means of the longitudinal and transverse displacements through Eq.(2.94) and Eq.(2.75).

This gives in total 4 degrees of freedom per node or 8 degrees of freedom per element.

In the transverse X^3 direction, standard beam element representation based on cubic interpolation functions has been used. In the axial direction cubic interpolation has been used instead of the conventional linear interpolation both in order to meet the requirements set by the strong coupling observed between the axial strain and the transverse displacements reflected in Eqs.(2.74)-(2.79) and also to take into account the strain distribution induced along

 ISBN 82-7119-427-5 ISSN 0802-3271

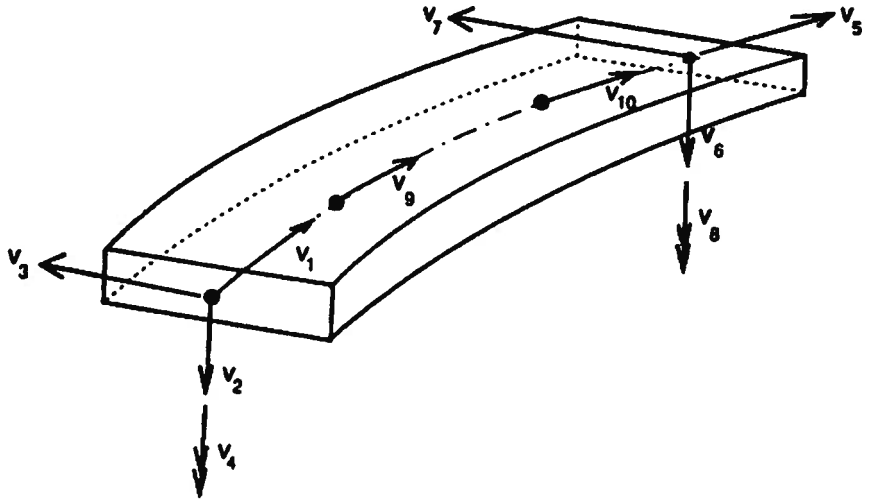

Figure 2.12 Eight (Ten) degree of freedom curved beam element

the element by friction forces. The two internal degrees of freedom are, however, eliminated by static condensation prior to the merging process (see Figure 2.12). In the radial direction linear interpolation has been used.

The displacement field u^0 along the centre line can be expressed by the nodal degrees of freedom and non-dimensional length coordinate ξ and element length l. On matrix form this can be expressed as:

$$u^0 = N\, v \tag{2.106}$$

or in component form:

$$u_i^0(\xi) = N_i^j(\xi)\, v_j \tag{2.107}$$

u^0 is a 3×1 matrix of displacement components along the centre line and v are a $n\times1$ matrix of the n element degrees of freedom. N is a $3\times n$ matrix of interpolation functions. The transposed N matrix takes the following form:

$$N^T = \begin{bmatrix} (1-\frac{11}{2}\xi+9\xi^2-\frac{9}{2}\xi^3) & 0 & 0 \\ 0 & (1-\xi) & 0 \\ 0 & 0 & (1-3\xi^2+2\xi^3) \\ 0 & 0 & -l\xi(\xi-1)^2 \\ (\xi-\frac{9}{2}\xi^2+\frac{9}{2}\xi^3) & 0 & 0 \\ 0 & \xi & 0 \\ 0 & 0 & (3\xi^2-2\xi^3) \\ 0 & 0 & -l\xi^2(\xi-1) \\ (9\xi-\frac{45}{2}\xi^2+\frac{27}{2}\xi^3) & 0 & 0 \\ (-\frac{9}{2}\xi+18\xi^2-\frac{27}{2}\xi^3) & 0 & 0 \end{bmatrix} \tag{2.108}$$

By dividing the N matrix into three parts N_i where i corresponds to row i in the N matrix, the virtual strain terms can be expressed by means of the nodal displacements as:

$$\delta\varepsilon_1 = (N_{1,1}-\kappa_3 N_2+\kappa_2 N_3)\ \delta v \tag{2.109}$$

$$\delta\varepsilon_2 = (N_{2,1}+\kappa_3 N_1-\kappa_1 N_3)\ \delta v \tag{2.110}$$

$$\delta\varepsilon_3 = (N_{3,1}-\kappa_2 N_1+\kappa_1 N_2)\ \delta v \tag{2.111}$$

$$\delta\omega_1 = (\kappa_2 N_{2,1}+\kappa_1\kappa_3 N_2-\kappa_t N_{3,1}+\kappa_3 N_{3,1}-\kappa_1\kappa_2 N_3)\ \delta v \tag{2.112}$$

$$\delta\omega_2 = (\kappa_2 N_{1,1}-\kappa_1\kappa_3 N_1-2\kappa_1 N_{2,1}-N_{3,11}-\kappa_t\kappa_3 N_3+\kappa_1^2 N_3)\ \delta v \tag{2.113}$$

$$\delta\omega_3 = (\kappa_3 N_{1,1}+\kappa_1\kappa_2 N_1+N_{2,11}-\kappa_1^2 N_2+\kappa_2\kappa_t N_3-2\kappa_1 N_{3,1})\ \delta v \tag{2.114}$$

By using the above terms, the stiffness matrix and the equilibrium forces of each element is determined by using Eqs.(2.99)-(2.100) and Eqs.(2.86)-(2.92) respectively.

The load vector contribution from each element is further determined by prescribing the increment in strain, twist and curvatures by means of Eq.(2.62) and Eqs.(2.64)-(2.66) and then

use the internal virtual work equation defined by Eqs.(2.86)-(2.92) for each global curvature increment. This corresponds to treating the loads as an initial strain problem.

The axisymmetric loading is further treated as a constant contribution to the prescribed longitudinal initial strain.

2.7.2 Rod/surface interaction

The rod/surface interaction has been modelled by means of hyperelastic or elastoplastic springs introduced at each node. The hyperelastic spring is conveniently used for bonded pipes where the rod is surrounded by rubber, whereas the elastoplastic (Coulomb friction) spring is used for nonbonded pipes in order to simulate sliding under friction. The elastoplastic spring has components of both stiffness and force in the X^1 and X^3 directions depending on the direction of slip [2.19]-[2.20]. It is coupled to a hyperelastic X^2 spring that simulates the radial stiffness of the supporting pipe. Hyperelastic properties in the X^1 and X^3 directions are included as an option. The spring properties are shown schematically in Figure 2.13.

2.7.3 Numerical integration

The technique used in order to carry out the integrations of the virtual work terms has been based on the three point Gauss numerical integration scheme. Thus, the torsion, curvature and strain components have to be prescribed and updated in the three integration stations.

In principal the three point Gauss integration scheme integrates a fifth order polynomial exactly. It is however seen from Eqs.(2.109-2.114) and Eqs.(2.99,2.100) that the resulting strain energy occuring in the stiffness matrix term will be of sixth order due to the coupling terms. The integration method used will therefore represent a *reduced integration* method [2.21]. The accuracy will be further commented in Chapter 4.

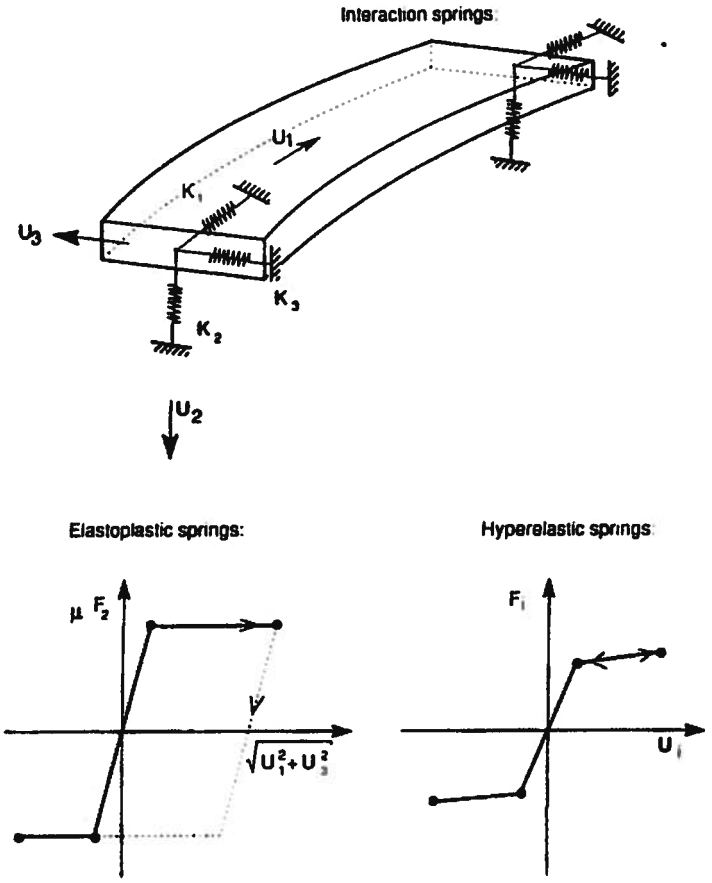

Figure 2.13 Tendon/Pipe interaction model

2.7.4 Numerical procedure

The numerical procedure utilized in order to solve the previous examined equations is briefly described below:

Loop over global curvature increments

For each global curvature step *n*, the load vector contribution is computed for each element by means of Gauss integration. The procedure used at each station is started by first

prescribing the increments of longitudinal strain ΔE_{11}^{0p}, twist $\Delta\kappa_1{}^p$, and curvatures $\Delta\kappa_2{}^p$ and $\Delta\kappa_3{}^p$, using Eq.(2.62) and Eqs.(2.64)-(2.66). Then the corresponding prescribed accumulated deformation values $E_{11}^{0\,p}$, $\omega_1{}^p$, $\omega_2{}^p$ and $\omega_3{}^p$ and also the total torsion and curvature components κ_1, κ_2 and κ_3 are updated. The load vector contributions are then calculated by using Eqs.(2.86)-(2.92) and the incremental prescribed kinematic quantities. The resulting accumulated internal element forces S^{it} are determined and stored for each element. Governing incremental kinematic equations are:

$$(E_{11}^{0\,p})^n = (E_{11}^{0\,p})^{n-1} + (\Delta E_{11}^{0\,p})^n \tag{2.115}$$

$$(\omega_1^p)^n = (\omega_1^p)^{n-1} + (\Delta\kappa_1^p)^n \tag{2.116}$$

$$(\omega_2^p)^n = (\omega_2^p)^{n-1} + (\Delta\kappa_2^p)^n \tag{2.117}$$

$$(\omega_3^p)^n = (\omega_3^p)^{n-1} + (\Delta\kappa_3^p)^n \tag{2.118}$$

$$(\kappa_1)^n = (\kappa_1)^{n-1} + (\Delta\kappa_1^p)^n \tag{2.119}$$

$$(\kappa_2)^n = (\kappa_2)^{n-1} + (\Delta\kappa_2^p)^n \tag{2.120}$$

$$(\kappa_3)^n = (\kappa_3)^{n-1} + (\Delta\kappa_3^p)^n \tag{2.121}$$

Equilibrium iterations within one load step

1. Build up the element stiffness matrices by using Eq.(2.99), Eq.(2.100) and Eqs.(2.109)-(2.114). In order to perform static condensation for elimination of the two internal nodes, the element equilibrium equation can be formulated as:

$$\begin{bmatrix} \Delta S_e^{ext} \\ \Delta S_i^{ext} \end{bmatrix} = \begin{bmatrix} k_{ee} & k_{ei} \\ k_{ie} & k_{ii} \end{bmatrix} \begin{bmatrix} \Delta v_e \\ \Delta v_i \end{bmatrix} + \begin{bmatrix} \Delta S_e^{it} \\ \Delta S_i^{it} \end{bmatrix} \tag{2.122}$$

where $\Delta S^{it}{}_e$ and $\Delta S^{it}{}_i$ have contribution both from internal stresses and consistent contact forces.

2. Perform static condensation of Eq.(2.122) to determine the element load vectors and stiffness matrix contributions by means of matrix manipulation :

$$\Delta \hat{S}=\Delta S_e^{ext}-\Delta S_e^{it}-k_{et}k_{ii}^{-1}(\Delta S_i^{ext}-\Delta S_i^{it}) \tag{2.123}$$

$$\hat{k}=k_{ee}-k_{ei}k_{ii}^{-1}k_{ie} \tag{2.124}$$

The sub-matrices k_{ei} and k_{ii}^{-1} are stored in order to find the elemental displacement distribution after solution of the final equation system.

3. Add the element load vectors and stiffness matrices into the global load vector ΔQ and tangential stiffness matrix K_T.

4. Implement interaction springs and boundary conditions.

5. Solve the equation system. Governing equation is:

$$K_T \Delta q=\Delta Q \tag{2.125}$$

6. Update the internal kinematic quantities by first finding the internal nodal displacements by:

$$\Delta v_i=k_{ii}^{-1}(\Delta S_i^{ext}-\Delta S_i^{it})-k_{ii}^{-1}k_{ie}\Delta v_e \tag{2.126}$$

and then update the kinematics in each Gauss station by:

$$(e_1)^{n,j} = (e_1)^{n-1+m,\,j-1} + (\Delta e_1)^{n,j} \tag{2.127}$$

$$(\varepsilon_2)^{n,j} = (\varepsilon_2)^{n-1+m,j-1} + (\Delta\varepsilon_2)^{n,j} \tag{2.128}$$

$$(\varepsilon_3)^{n,j} = (\varepsilon_3)^{n-1+m,j-1} + (\Delta\varepsilon_3)^{n,j} \tag{2.129}$$

$$(E_{11}^0)^{n,j} = (E_{11}^0)^{n-1+m,j-1} + (\Delta\varepsilon_1 + \frac{1}{2}\Delta\varepsilon_1^2 + \frac{1}{2}\Delta\varepsilon_2^2 + \frac{1}{2}\Delta\varepsilon_3^2)^{n,j} \tag{2.130}$$

$$(\omega_1)^{n+1,j} = (\omega_1)^{n-1+m,j-1} + (\Delta\kappa_1)^{n,j} \tag{2.131}$$

$$(\omega_2)^{n+1,j} = (\omega_2)^{n-1+m,j-1} + (\Delta\kappa_2)^{n,j} \tag{2.132}$$

$$(\omega_3)^{n+1,j} = (\omega_3)^{n-1+m,j-1} + (\Delta\kappa_3)^{n,j} \tag{2.133}$$

$$(\kappa_1)^{n+1,j} = (\kappa_1)^{n-1+m,j-1} + (\Delta\kappa_1)^{n,j} \tag{2.134}$$

$$(\kappa_2)^{n+1,j} = (\kappa_2)^{n-1+m,j-1} + (\Delta\kappa_2)^{n,j} \tag{2.135}$$

$$(\kappa_3)^{n+1,j} = (\kappa_3)^{n-1+m,j-1} + (\Delta\kappa_3)^{n,j} \tag{2.136}$$

where j is the iteration step and $m=0$ for $j = 1$ and $= 1$ else.

7. Determine the unbalanced load vector from each element in the same way as described for the load step, but based on the difference between the last calculated quantities of Eqs.(2.130-2.133) and the prescribed quantities of Eqs.(2.115-2.118) from the current load step computation.

8. Update the interaction spring state and add the reaction forces to the load vector to be used for next iteration.

9. Calculate normalized Euclidean displacement norm and unbalanced force norm. If these are larger than the tolerance limit repeat step 1-9, else initiate the next load increment.

2.7.5 Computer implementation

The procedure outlined in the previous sub-section has been implemented into a computer program *AFLEX*. The language used is standard *FORTRAN-77* and it has been implemented on *DEC-station* under the *UNIX* operative system.

 ISBN 82-7119-427-5 ISSN 0802-3271

3 FATIGUE MECHANISMS IN FLEXIBLE PIPES

3.1 Introduction

The purpose of this chapter is firstly to examine the different physical phenomena connected to surface contact and sliding between layers during bending of nonbonded flexible pipes. This will give an understanding of fatigue mechanisms relevant for armouring layers and also how the friction coefficient is influenced by various factors. The friction coefficient is an important input parameter to the numerical studies carried out in the subsequent chapters.

Secondly, the *state of the art* of current fatigue design practice will be reviewed together with a presentation of available data for some important parameters.

3.2 Surface interaction

3.2.1 General

If two metal surfaces are in contact with each other like two armouring layers of flexible pipes, there will be atom to atom contact in some regions, whereas in other regions no such contact will occur due to surface roughness. The atom to atom contact will create *junctions* between the two materials at certain *asperities*. By increasing the normal load, the number of

 ISBN 82-7119-427-5 ISSN 0802-3271

asperities in direct contact will increase, thus giving increased resistance against sliding between the two surfaces if a tangential load is applied. The friction resistance therefore depend on the *real area* of contact, thus explaining why the friction resistance is independent of the *apparent area* of contact, but depending on the normal load only.

As the two contacting surfaces are exposed to an equal magnitude but opposite directed tangential force adhesive interatom forces will build up at the individual asperity contact points. These forces will inhibit free sliding between the two surfaces. Shear stresses will therefore build up until the asperities are plastically sheared and unidirectional sliding takes place. During this process material fragments are produced, thus creating wear of the two materials.

The above is called the *adhesive wear theory*, according to Rabinowicz [3.1].

If the surfaces are exposed to unidirectional sliding or oscillatory sliding of sufficient amplitude, the asperities in direct contact are sheared off during each cycle. This process will involve *sliding wear* and the amount of wear can be evaluated by the Archard's formula [3.2], which reads:

$$V_w = \frac{k_w P_N u}{3p_h} \tag{3.1}$$

where V_w is the wear volume, k_w is the wear coefficient, P_N is the normal load, u is the sliding distance and p_h is the material surface penetration hardness [3.1].

3.2.2 Fretting

Fretting is defined as low amplitude oscillatory sliding between two tribo surfaces (contact between two convex surface elements), Vingsbo and Odfalk [3.3].

When two metal bodies are pressed together at a small contact area, high contact stresses will

 ISBN 82-7119-427-5 ISSN 0802-3271

occur. These stresses have to be transferred into the surrounding material volume of both bodies. The way this transfer takes place and the associated deformations were first investigated by Hertz. A treatise of his theory is found in Love [2.2], where general solutions are presented for bodies that can be described by means of their principal radii of curvature at the point of contact and where the surrounding material volume is large compared to the contact area. The solution involve elliptic integrals of first and second kind.

The solution of the contact problem for elliptical and spherical bodies exposed to both normal and tangential loading has been extensively treated by Mindlin and Deresiewicz [3.4], Mindlin [3.5], Deresiewicz [3.6] and Mindlin et. al [3.7]. For spherical bodies the solution shows that the contact stress due to normal loading between the two bodies has its maximum at the centre of the contact area. The theoretical distribution of shear stresses due to tangential load is further found to be described by being zero at the centre of the contact area, growing towards infinite at the rim of the contact area. This shear stress can, however, not exceed the normal contact stress multiplied by the friction coefficient. Thus, microslip will take place outside the inner region where the shear stress is less than the maximum friction stress. The inner region at which no slip occur is termed the *stick* region, whereas the outer region where slip does occur is termed the *slip* region.

Vingsbo and Søderberg [3.8] defines four different slip amplitude regimes for oscillatory sliding, each involving different modes of surface damage:

1. *Stick regime*. There is no slip between the surfaces. Very limited surface damage by oxidation and wear. No crack formation observed (up to 10^6 cycles). *Low damage fretting*, sometimes referred to as fretting corrosion.

2. *Mixed stick-slip regime.* Slip at the outer region, no slip in the inner region of contact. Wear and oxidation effects are small. Accelerated crack growth may result in strongly reduced fatigue life. *Fretting fatigue.*

3.*Gross-slip regime.* Slip occur over the entire contact area, but the displacement amplitude is small. Severe surface damage by oxidation-assisted wear. Crack formation limited. *Fretting wear.*

4. *Reciprocating sliding regime* (generally not classified as fretting). With increasing amplitude gross slip approaches reciprocating sliding. The limiting conditions are those for which wear mechanisms and wear rates become characteristic of unidirectional sliding.

The mechanisms behind fretting and wear damage are complicated, and influenced by at least three primary parameters for a given material and environmental condition [3.8] :

- Normal load
- Tangential force/displacement amplitude
- Tangential force/displacement frequency

Nakazawa et al. [3.9] however conclude that for frequencies in the range 0.167-20 Hz, the number of cycles needed to create fatigue is unaffected by changing the frequency. The material investigated was high strength steel. From this one can conclude that the normal load and the displacement amplitude are the controlling parameters for fretting fatigue of armouring layers in flexible pipes.

Among the above defined regimes, the *mixed stick-slip regime* has the strongest influence on fatigue life. This is caused by the fact that high macrostresses will be present at the transition between the stick and slip regions, stresses which are highly effective in crack formation [3.8]. The cracks initiated in this process will typically grow with an angle deviating from the surface normal into the material.

Vingsbo and Odfalk [3.3] have advocated the use of fretting maps, in which the transition from one failure mode to another is identified by combinations of critical values of two primary parameters. Generally there is a gradual transition from the fretting corrosion to the

 ISBN 82-7119-427-5 ISSN 0802-3271

fatigue region, whereas the transition from the fatigue to the wear region is more well defined. There is no clear distinction between the fretting wear and the reciprocating wear regimes. According to Waterhouse [3.10], the specific wear rate is controlled by unidirectional sliding for slip amplitudes above 0.1 mm and the process should be termed reciprocating sliding for slip above this value.

3.2.3 The friction coefficient

The friction coefficient depends on several factors, such as the material of the contacting surfaces, static or dynamic sliding conditions and the presence of lubrication.

Lubrication or anti-friction layers are commonly used between armouring layers in order to avoid surface interaction problems. Thus, the friction coefficients to be used in simulations depend on the actual pipe design.

The effect of lubrication in terms of the friction coefficient depends on the sliding velocity according to the *Stribeck's* curve [3.11]. Such a curve is presented in Figure 3.1 where the friction coefficient has been expressed as a function of the lubrication parameter defined as the product of dynamic viscosity, sliding velocity and the inverse normal load. The curve is divided into three regions, each being characterized by different conditions of lubrication. At zero and low velocities there is boundary lubrication, characterized by a thin lubricant film adsorbing to the solid surfaces which significantly inhibits asperity welding. There is, however, still considerable asperity interaction. As the velocity increases the friction coefficient drops until hydrodynamic lubrication is obtained. At hydrodynamic lubrication a pressure is created within the lubricant which is sufficiently high to keep the surfaces completely separated. In this way, various conditions of lubrication gives significant different friction coefficients.

In a flexible riser the sliding velocity will vary along each tendon (see Eq.(2.29) and Eq.(2.30)). Thus, the friction coefficient will vary along lubricated tendons in flexible risers.

 ISBN 82-7119-427-5 ISSN 0802-3271

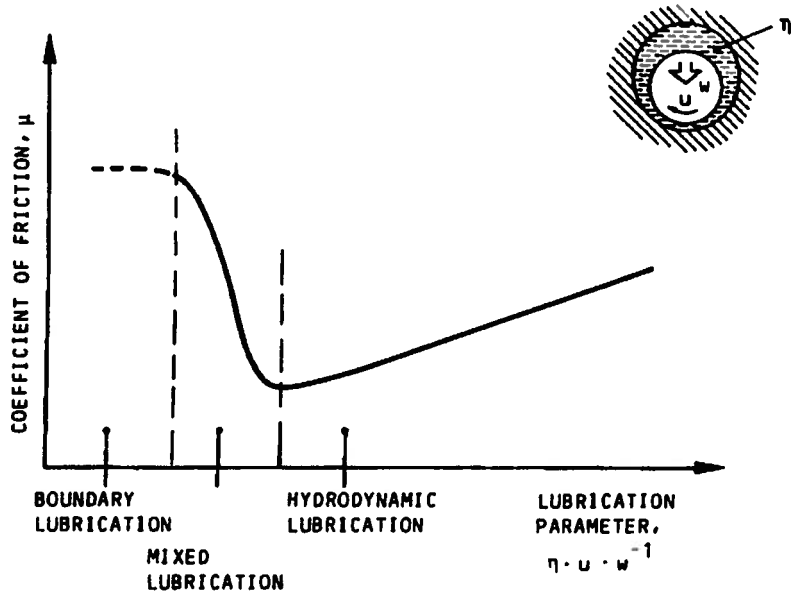

Figure 3.1 Stribeck's curve

3.3 Existing fatigue failure models

3.3.1 Fatigue failure models

The fatigue failure models reported by Feret et al. [1.7] and Nielsen et al. [3.12] are both based on wear effects due to reciprocating sliding and evaluating the wear rate by means of the Archard's formula, see Eq.(3.1). This means that fretting effects are not considered in these formulations.

The oscillatory sliding amplitudes are obtained by assuming that the tendon deformations follow the geodesic of a constantly curved pipe. Laboratory tests have further been carried out to find the wear coefficients. On this basis and calculated contact stresses, a wear model is established.

 ISBN 82-7119-427-5 ISSN 0802-3271

In the first wear model one stage of deterioration is assumed. The reciprocating sliding causes a decrease in the cross section of the armouring and therefore an increase in stresses. The flexible pipe is considered to fail when the maximum dynamic stress range exceeds the fatigue limit of the material. The fatigue limit has further been assessed on the basis of uniaxial fatigue tests of an individual armouring tendon, from which a Haig diagram can be constructed (Confer Figure 1.5).

In the second fatigue model reported, however, the *S-N* approach is utilized instead of the conservative criterion of fatigue onset. The design life is subdivided into wear rate intervals over which material loss is integrated. The stress ranges characterizing one interval is adjusted for the amount of wear that occured in the previous interval. Miner's rule is then used to determine the expected life at selected locations based on cumulative damage. The detailed procedures used are however not given on explicit form.

3.3.2 Measured friction and wear coefficients

The effect on friction from lubrication for two steel armouring layers in direct contact was investigated both by using individual tendon specimens and full-scale pipe specimens as reported by Feret et al. [1.7]. With reference to the Stribeck's curve in Figure 3.1, the static friction coefficient corresponding to zero sliding velocity was found to be 0.3 whereas the minimum value corresponding to full lubrication was 0.01. Under rotative bending tests of flexible pipe specimens, a state of average lubrication was obtained giving dynamic friction coefficients in the range 0.07-0.1. These friction coefficients were obtained by calibrating the calculated friction moment to the measured moment, and they must therefore be considered as average values along the tendons.

For metal to metal contact, Rabinowicz [3.2] gives wear coefficients of $5 \cdot 10^{-3}$, $2 \cdot 10^{-4}$, 10^{-5} and 10^{-6} for clean, poorly lubricated, average lubricated and excellent lubricated sliding conditions, respectively.

The wear coefficients found from laboratory tests on individual armouring tendons, were in the interval of $5 \cdot 10^{-6}$ - $4 \cdot 10^{-5}$, whereas the results from rotative bending tests indicated a

reduction factor of 4. Following the definition by Rabinowicz, this confirms the state of average lubrication, as the most relevant condition for flexible pipe armouring.

 ISBN 82-7119-427-5 ISSN 0802-3271

4 NUMERICAL STUDIES

4.1 Introduction

The purpose of this chapter is mainly to verify that the numerical model presented in Chapter 2 adequately describes the tendon kinematics. This verification has been carried out by comparing the results from the numerical model with analytical solutions valid for a tendon along the geodesic in a pipe exposed to constant curvature.

The second purpose is to evaluate the influence on the tendon behaviour in terms of twist, curvatures, stresses and displacements from various effects such as pressure, friction, global tension, global curvature distribution, radial stiffness and load history. These effects have been investigated by analysing one outer layer tendon exposed to different conditions of loading and boundary conditions.

Finally an investigation of stresses and relative displacements in a realistic 8-inch flexible riser has been carried out.

ISBN 82-7119-427-5 ISSN 0802-3271

4.2 Stiffness of supporting surface

The tendon is assumed to be sliding on the supporting pipe cross section surface. This surface is represented by means of hyperelastic springs in the numerical model. The outer armouring layer will be restrained by stiff steel layers against inward displacements, whereas for the outward direction the restraint is represented by the soft external sheath. Thus there will be a significant difference between the inward stiffness and the outward stiffness. In order to find the spring stiffness to be used in the numerical examples, the radial displacement of the armouring layer versus the change in tendon axial stresses has been investigated under axisymmetric conditions using the computer program CAFLEX [1.6].

For the purpose of the numerical examples described in this chapter a radial spring stiffness of $9 \cdot 10^8$ Nm^{-2} inwards and $5 \cdot 10^6$ Nm^{-2} outwards has been used if not otherwise noted.

4.3 Comparison between numerical and analytical solutions

4.3.1 Description of example

The purpose of this example is to verify that the developed finite element model can give an adequate description of the kinematics involved in the problem. The verification has been carried out by comparing the results obtained from the numerical model with the analytical solution for a case with a constantly curved pipe and with no friction between the armouring layers. When the pipe is bent, the tendon will tend to move towards the geodesic in order to eliminate transverse curvature. The analytical solution of this problem in terms of relative displacement components as well as twist and normal curvature change is given by Eqs.(2.29)-(2.32).

One outer tendon with 25^o lay angle and 0.1 m layer radius is exposed to a constant curvature of 0.25 m^{-1}. The material law of the tendon is based on standard steel values and the cross section is 3 mm thick and 6 mm wide. The length of the model corresponds to 2.5 pitches and 50 elements are used. This gives an element length of 74 mm at 25^o lay angle. The start of

 ISBN 82-7119-427-5 ISSN 0802-3271

the model is at the outermost fibre on the tensile side of the pipe ($\nu = \pi$) as shown in Figure 4.1. The tendon is assumed to be fixed against radial and transverse displacements but free to rotate about the surface normal at both ends. Longitudinal springs with stiffness $2.0 \cdot 10^7$ Nm^{-1} have also been introduced at the ends. In order to ensure that the tendon will move towards the geodesic, the friction is set to zero and an initial pretension stress of 500 MPa is applied. The loading is applied by means of one tension load step, followed by five curvature increments.

4.3.2 Discussion of results

The numerical and analytical solutions for relative displacements as well as twist and normal curvature change, are presented in Figures 4.2-4.4. In these figures the numerical predicted values are indicated by markers and continuous curves are used to present the analytical solutions. It is seen that the correlation between the numerical solutions and the analytical expressions in general is very good. However, the numerical model gives more twist on the compressive side than on the tensile side of the pipe, while the analytical solution is symmetric. This is caused by the fact that the analytical solution represents the first term of a Taylor series expansion in R/ρ. As the torsion involves third order derivatives of the arc length coordinate, this simplification will introduce inaccuracies in the analytical solution. A similar behaviour has been reported by Feret et al. [1.17].

The results show that the kinematic description implemented in the numerical model gives similar results as can be obtained by differential geometry. It is thus concluded that the kinematic restraint introduced by Eq.(2.34) correctly provides a support of the tendon element and thereby gives a correct description of the tendon on the pipe surface.

 ISBN 82-7119-427-5 ISSN 0802-3271

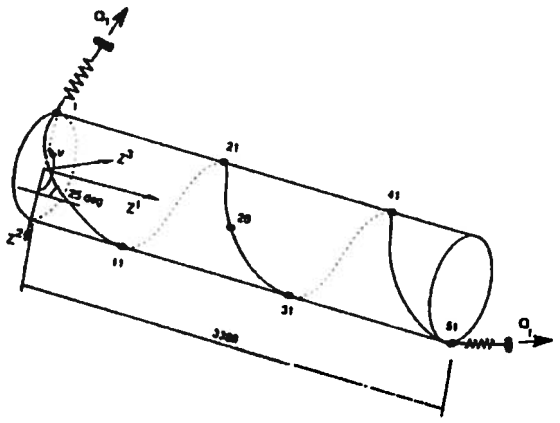

Figure 4.1 AFLEX finite element model for simple test examples

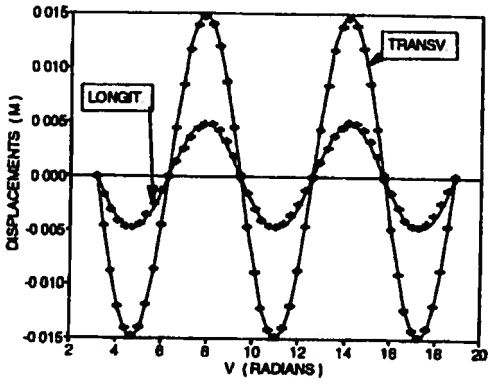

Figure 4.2 Comparison between numerical (dots) and analytical (solid line) predicted displacements, constant curvature

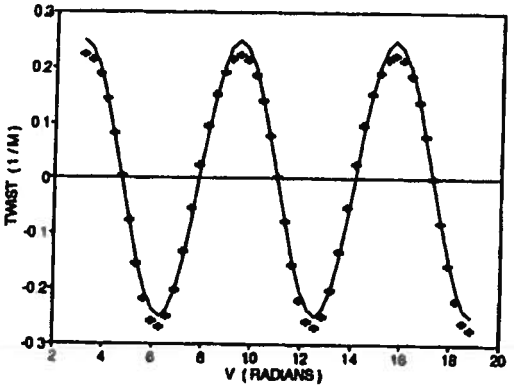

Figure 4.3 Comparison between numerical (dots) and analytical (solid line) predicted twist, constant curvature

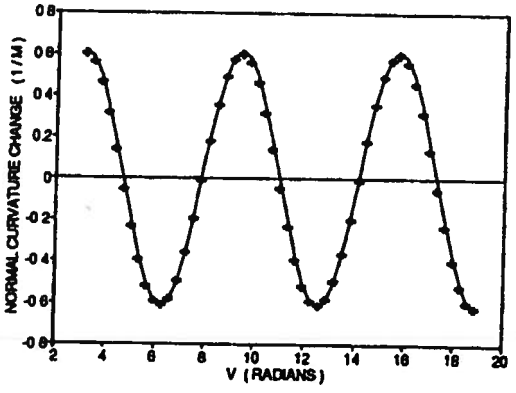

Figure 4.4 Comparison between numerical (dots) and analytical (solid line) predicted normal curvature change, constant curvature

ISBN 82-7119-427-5 ISSN 0802-3271

4.4 Displacements, twist and normal curvature at curvature gradients

4.4.1 Description of numerical example

The purpose of this example is to investigate the effect from variable curvature along the pipe on relative displacements as well as twist and normal curvature change. The error induced by applying the analytical expressions based on constant curvature at any point along a pipe with varying curvature is demonstrated. The example is the same as described in Sub-section 4.3.1 except that the curvature is varied linearly from 0.25 m^{-1} at the start of the model to zero after 0.5 pitch and that the boundary conditions in the longitudinal direction are changed. The tendon is fixed in the longitudinal direction at the start of the model and free at the other.

4.4.2 Discussion of results

The results are presented in Figures 4.5-4.7. It is seen that both the longitudinal and the transverse displacements are underestimated by the analytical expressions. The reason is that any varying curvature will influence the tendon behaviour over the entire length of the model. Since the curvature has the highest value at the start of the model and the tendon starts at the tensile side, the length of the curve path along the first quarter pitch will be longer than for the next quarter pitch. If friction was present this would induce axial strains in the tendon. However, since there is no friction, straining is compensated by a longitudinal displacement along the entire tendon.

By looking at the transverse displacements in Figure 4.5, the following is observed: As the length of the model is increased towards infinite, the theoretical maximum value of the transverse displacement needed to reach the geodesic will be limited by the value giving zero slope of the transverse displacement curve. Therefore, the geodesic between two points on a surface having variable curvature may involve larger transverse displacements than for a constantly curved pipe even if the maximum curvature of the first pipe is smaller.

It is seen that the twist and normal curvature change are overestimated by the analytical formulas. This is caused by the fact that the gradient of transverse tendon displacement is

 ISBN 82-7119-427-5 ISSN 0802-3271

lower than predicted by the analytical formulas, i.e the distance over which the actual displacements occur is longer.

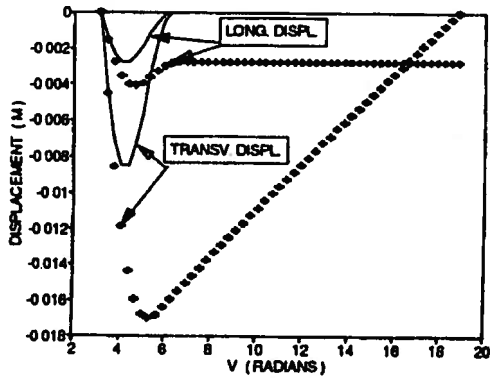

Figure 4.5 Comparison between numerical (dots) and "analytical" (solid line) predicted longitudinal displacements, linear curvature

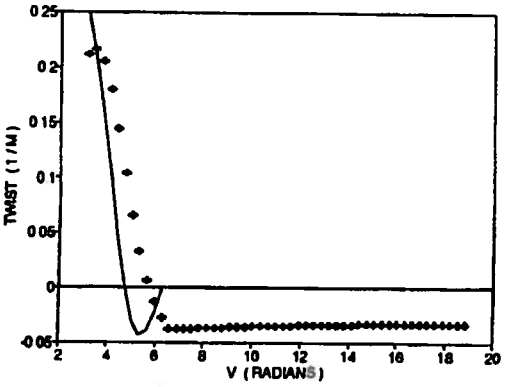

Figure 4.6 Comparison between numerical (dots) and "analytical" (solid line) predicted twist, linear curvature.

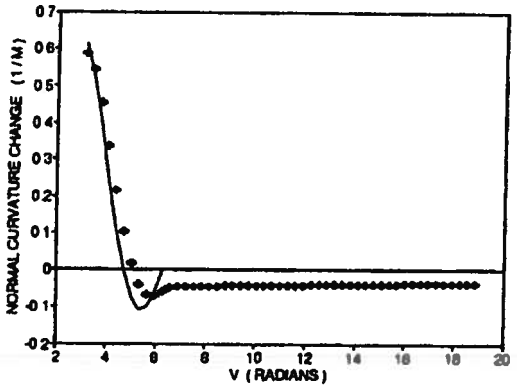

Figure 4.7 Comparison between numerical (dots) and "analytical" (solid line) predicted normal curvature change, linear curvature

 ISBN 82-7119-427-5 ISSN 0802-3271

4.5 Effect from friction and pretension on transverse displacements

4.5.1 Description of numerical example

The purpose of the following example is to investigate the effect from tension and friction on the tendon transverse relative displacement. The example is identical to the one described in Sub-section 4.3.1, except that the lay angle, the cross section geometry, the friction coefficient and the tendon tension are varied as described below.

4.5.2 Tension under no friction

The normalized transverse displacement is studied as a function of tension. The friction is set to zero. Results are normalized with respect to the maximum value found from Eq.(2.30), which represents the geodesic solution. Two alternative lay angles (25^o and 35^o) and two cross section dimensions (1×1 mm and 3×6 mm) are included in the analysis.

Figure 4.8 shows the maximum normalized transverse displacement as a function of applied tensile stress for the alternative lay angles and cross section dimensions. It is seen that the tendon will be restrained from reaching the geodesic. This is due to the effect from torque and bending moments induced during the movement towards the geodesic. At low tensile stress the tendon's equilibrium position is represented by a curve between the loxodromic curve and the geodesic. As the tension is increased, these effects are eliminated, more efficiently for small cross sections, until the geodesic is reached in the limit.

ISBN 82-7119-427-5 ISSN 0802-3271

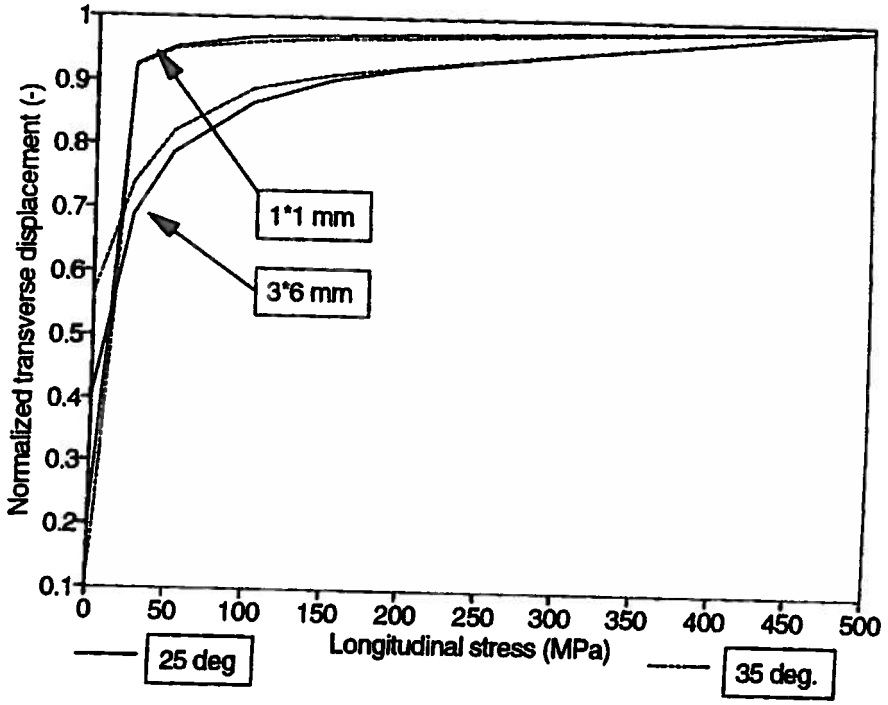

Figure 4.8 Normalized transverse displacement as function of applied tensile stress, no friction

4.5.3 Friction under constant tension

The normalized transverse displacement is studied as a function of the friction coefficient. The cross section dimension is 3×6 mm and a pretension stress of 150 MPa is applied. Three alternative lay angles (25°, 35° and 45°) are investigated. The friction is introduced by using the Coulomb friction model and by applying the full magnitude of the friction force after 0.1 mm sliding which corresponds to the transition between gross-slip and reciprocating sliding conditions (confer Sub-section 3.2.2).

By using the Principle of Virtual Displacements and assuming a simple trigonometric sinusoidal shape function, including terms from axial forces, initial curvature along the loxodromic curve, bending stiffness and sideways forces from friction, the maximum normalized transverse displacement of the tendon is obtained as:

ISBN 82-7119-427-5 ISSN 0802-3271

$$\bar{u}_3 = \frac{1 - \dfrac{4}{\pi} \dfrac{\mu Q_1 R \rho}{C_\sigma I_2 \cos\alpha (1+\sin^2\alpha)} + \dfrac{Q_1 R^2}{C_\sigma I_2 \sin^2\alpha}}{1 + \dfrac{Q_1 R^2}{\sin^2\alpha C_\sigma I_2}} \tag{4.1}$$

Results from this equation are shown by markers in Figures 4.9-4.11 for the three lay angles. The corresponding values obtained by the numerical model are shown by continuous curves in the same figures. It is seen that there is a good correlation between the numerical solution and the results obtained from Eq.(4.1) at low friction values, whereas there is a significant deviation at higher friction values. This is caused by the fact that the analytical formula assumes that the full magnitude of friction is applied in the transverse direction only, while the numerical model takes into account that the friction force always must be opposite to the slip direction. If the slip had followed the tendon axial direction, the friction force would not have a component in the transverse direction. Since a bent pipe will induce tendon transverse curvature along the tendon, transverse force components will occur due to tension as well as torque and bending moments. These load components will tend to eliminate the transverse curvature. Thus both longitudinal and transverse slip will always occur. This is in contradiction to the approach reported by Nielsen at. al. [3.12]. The magnitude of the transverse displacement will, however, be significantly reduced compared to the geodesic solution. For a lay angle of 35° only 40 % of the possible slip will take place for a friction coefficient of 0.05.

The observation is made that the transverse displacements are suppressed for friction coefficients of 0.12, 0.075 and 0.04 for 25°, 35° and 45° lay angles respectively by using Eq.(4.1). This result can be verified by introducing Eq.(2.14) and Eq.(2.65) in Eq.(2.33). Transverse displacements can thus not take place for friction coefficients larger than:

$$\mu = \frac{\cos\alpha}{\sin^2\alpha} (1+\sin^2\alpha) \frac{R}{\rho} \tag{4.2}$$

 ISBN 82-7119-427-5 ISSN 0802-3271

This equation is studied in Figure 4.12, where the limit friction coefficient is presented as a function of R/ρ for several alternative lay angles. In this case $R/\rho = 0.025$. It is seen that the results obtained for the limit friction coefficient by Eq.(4.1) are in good agreement with the values obtained by Eq.(4.2). However, analytical formulas are generally not capable of predicting the actual transverse displacements.

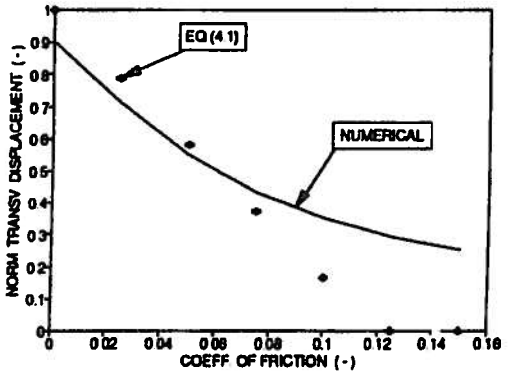

Figure 4.9 Normalized transverse displacement as a function of friction, 25° lay angle

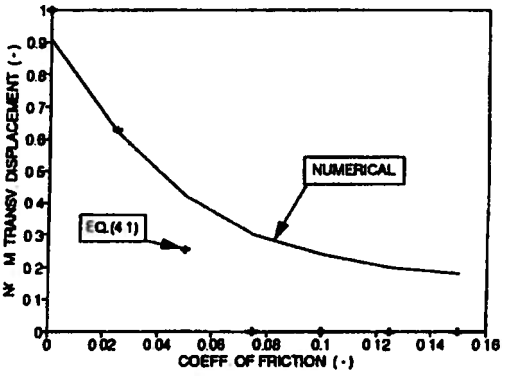

Figure 4.10 Normalized transverse displacement as a function of friction, 35° lay angle

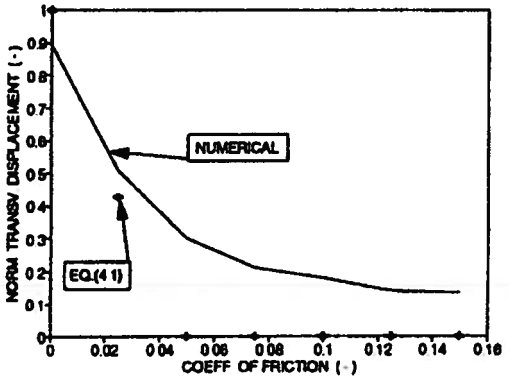

Figure 4.11 Normalized transverse displacement as a function of friction, for 45° lay angle

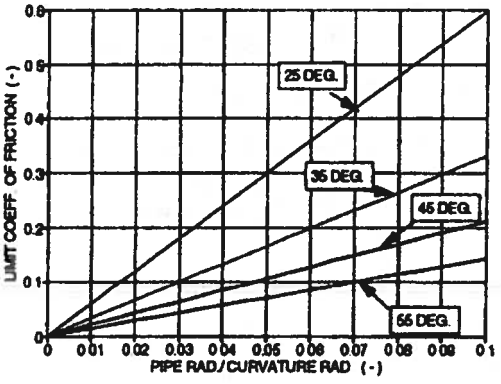

Figure 4.12 Limit friction coefficient for alternative lay angles

 ISBN 82-7119-427-5 ISSN 0802-3271

4.6 Investigation of friction effects under cyclic curvature loading

4.6.1 Description of example

The purpose of this example is to study the influence from friction on axial stresses and longitudinal displacements during loading and unloading throughout a cycle of constant curvature loading. Two alternative friction formulations are used, namely hyperelastic and Coulomb friction spring models.

The example is similar to that described in Sub-section 4.3.1, except that the pretension stress is 150 MPa and the friction coefficient is set to 0.05. The full magnitude of friction is introduced after 0.1 mm relative displacement as described in Sub-section 4.5.3. The pretension is applied under no friction but friction is introduced during the succeeding stepwise application of constant curvature cycles ranging from -0.01 m^{-1} to 0.01 m^{-1}.

4.6.2 Investigation of alternative friction models

Figure 4.13 shows the axial stress in node 21 (see Figure 4.1), which is positioned on the tensile side of the pipe, as a function of curvature and using both hyperelastic and Coulomb friction spring models. It is observed that for the hyperelastic model there is no hysteresis as expected, whereas the Coulomb friction spring model gives significant hysteresis. The predicted maximum stress range is, however, equal for both formulations. This is due to the fact that the value and direction of the friction force computed by the hyperelastic model is a one to one function of the total relative displacement. Thus, in order to change friction force direction in the hyperelastic model, the sign of the displacement has to shift. The maximum stress will therefore be equally predicted for periodic loading where the curvature shift sign. However, for cases where the curvature direction does not change, there will be a significant difference between the stress ranges predicted by the Coulomb friction and hyperelastic spring models due to the hysteresis effect. The observation is also made that there is a smooth transition in the axial stress towards the threshold value corresponding to full sliding.

 ISBN 82-7119-427-5 ISSN 0802-3271

Figure 4.14 shows the axial displacement of node 26 (see Figure 4.1), which is positioned at the neutral axis of bending, during the same curvature cycle. Both spring formulations are included in the analysis. It is seen that the axial displacement at this point is not influenced by friction, thus being independent of the spring model choice. This is due to the fact that the possible axial straining induced by bending will create shear stresses much higher than the friction resistance. Thus the displacements will be entirely controlled by the movement of the supporting pipe.

Figure 4.15 shows the corresponding force displacement diagram for the Coulomb and hyperelastic spring models in node 26.

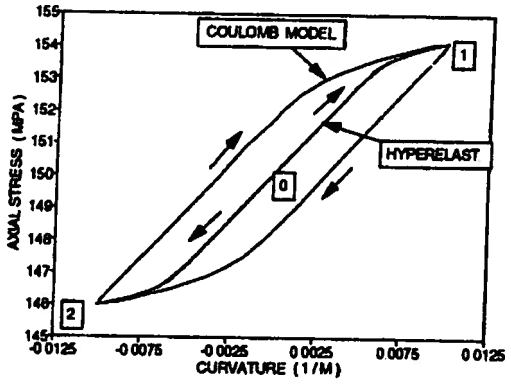

Figure 4.13 Axial stress history in node 21

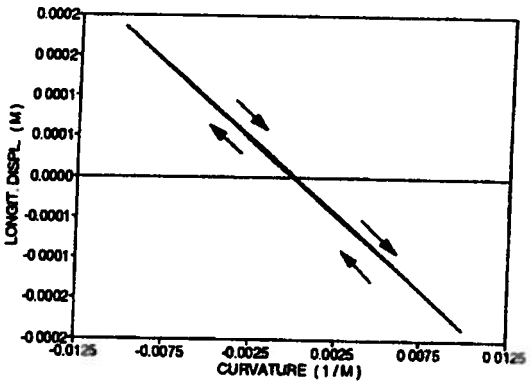

Figure 4.14 Axial displacement history in node 26

4.6.3 Development of slip zone

The curvature amplitude is increased to 0.02 m^{-1}. Other parameters are as described in Sub-section 4.6.1. Figure 4.16 shows the normalized slip length as a function of curvature during the first quarter of a cycle. The normalized slip length is obtained by taking the length of tendon along one half pitch having relative displacements above the value corresponding to full friction (0.1 mm) and then divide by the half pitch tendon length. It is seen that as the

curvature increase above 0.0047 m^{-1} slip occurs and grows rapidly up to a curvature level of 0.0078 m^{-1} and then shows a continuously reduced gradient. This behaviour explains the smooth transition of the axial stress curve towards the threshold value in Figure 4.13.

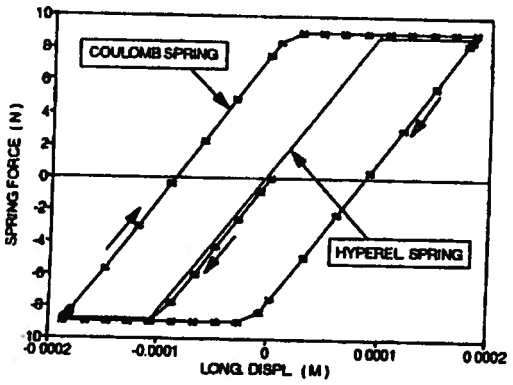

Figure 4.15 Spring force/displacement diagram in node 26

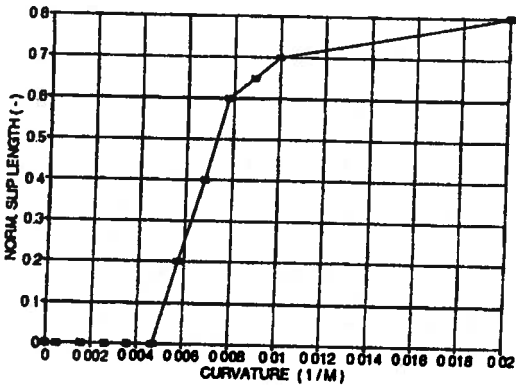

Figure 4.16 Development of slip zone as a function of curvature

4.7 Investigation of stress effects from bending gradient and end restraint

4.7.1 Description of example

The purpose of this example is to perform a sensitivity study of the stresses occuring at end restraints with respect to the sequence of load application, end restraint axial stiffness, the radial stiffness and the friction coefficient. The end restraint axial stiffness occurs from the termination of each individual tendon at the end fitting by use of an epoxy casting whereas the radial stiffness is due to the stiffness of the surrounding pipe layers as described in Section 4.2. The example chosen corresponds to a flexible pipe that is rigidly connected with a given end angle at one end and exposed to a stepwise increasing tensile load in the other end. The tensile load will hence induce a moment at the rigidly connected end. This will induce an exponential curvature distribution along the pipe given by:

 ISBN 82-7119-427-5 ISSN 0802-3271

$$\frac{1}{\rho}(z) = \theta \left(\frac{T}{EI}\right)^{\frac{1}{2}} e^{-\left(\frac{T}{EI}\right)^{\frac{1}{2}} z} \tag{4.3}$$

where EI is the bending stiffness, T is the applied tension, θ is the applied end angle and z is the length coordinate along the pipe longitudinal axis. For a fixed angle and given bending stiffness there will be an unique curvature distribution corresponding to each tension level.

Based on the above considerations, the maximum curvature at the fixed end of the tendon model is prescribed to 0.1 m^{-1} and then decreasing linearly to zero after one half pitch. This curvature is assumed to be obtained at an axial stress level of 450 MPa. The initial axial stress from internal pressure at zero curvature is assumed to be 150 MPa which means that the maximum curvature corresponds to 300 MPa increase in the tendon axial stress.

The model geometry and boundary conditions are according to Sub-section 4.3.1 except that the tendon starts at the neutral axis of bending ($\nu=\pi/2$) and that the tendon at this position is rotationally fixed about the surface normal. According to Eq.(2.65) the maximum tendon transverse curvature will occur at the neutral axis of bending. Since the tendon is assumed to be fixed against rotation about the surface normal at this point, secondary curvature effects similar to those described by Eq.(4.3) will occur locally in the tendons as the tension is increased.

According to Sub-section 4.4.2, a variable curvature distribution as described by Eq.(4.3) will create friction induced axial stresses caused by axial displacements. These displacements occur from the differences in path lengths of the tendon along the tensile and compressive pipe sections respectively. The difference in path length in this case occurs both due to the position of the tendon at the start of the model and the presence of curvature gradient. The lay angle is 25° implying that the tendon will be on the tensile side of the pipe when the maximum global curvature occurs. Thus axial tensile stresses will occur in this case.

 ISBN 82-7119-427-5 ISSN 0802-3271

The full magnitude of friction is obtained after 0.1 mm displacement corresponding to the transition between the gross-slip and reciprocating sliding regimes (confer Sub-section 3.2.2). Both axial and local bending stress effects are studied.

4.7.2 Axial stress distribution for alternative load histories

The effect of applying two alternative load histories is studied. The end restraint and radial spring stiffness are according to Sub-section 4.3.1 and the friction coefficient is 0.05.

Both load histories are started by applying the initial prestress of 150 MPa. Thereafter, the first history applies curvature and tensile stresses by equal incrementation (History 1). The second history applies 70 % of the total curvature at 20 % of the tensile stress during the first part of the load sequence, then continuing up to the full magnitude of both (History 2). These procedures have been used throughout loading, unloading and reloading.

Figure 4.17 shows the axial stress histories for node 6 being positioned at the outer tensile side of the pipe. Results for both loading procedures are given. It is seen that there is a significant difference in stress values at a given curvature. The maximum stress range is, however, not significantly effected by the sequence of load application.

4.7.3 Axial stress distribution for alternative radial stiffnesses

The axial end restraint spring stiffness is $2 \cdot 10^7$ Nm^{-1} as in Sub-section 4.3.1 and the friction coefficient is 0.05. The load history has been based on equal incrementation of tension and curvature up to the maximum values. The maximum axial stress distribution obtained by radial stiffnesses $9 \cdot 10^9$ (Stiffness 1), $9 \cdot 10^8$ (Stiffness 2) and $9 \cdot 10^7$ Nm^{-2} (Stiffness 3) have been studied. The results are presented in Figure 4.18. It is seen that for stiffnesses above $9 \cdot 10^8$, a further increase in stiffness will have limited effect on the stresses.

 ISBN 82-7119-427-5 ISSN 0802-3271

4.7.4 Axial stress distribution for alternative end restraint spring stiffnesses

The radial spring stiffness used is $9 \cdot 10^8$ Nm^{-2} according to Section 4.2 and the friction coefficient is set to 0.05. The load history has been based on equal incrementation of tension and curvature up to the maximum values. The maximum axial stress distribution obtained by end restraint stiffnesses $2 \cdot 10^8$ (Stiffness 1), $2 \cdot 10^7$ (Stiffness 2), $2 \cdot 10^6$ (Stiffness 3) and $2 \cdot 10^5$ Nm^{-1} (Stiffness 4) are presented in Figure 4.19. It is seen that for stiffnesses above $2 \cdot 10^7$, an increase in stiffness will have limited effect on the stresses.

4.7.5 Local bending stress distribution for alternative friction coefficients

The distribution of the maximum bending stresses close to the end fitting and induced by bending about the surface normal is studied for alternative friction coefficients. The results are shown in Figure 4.20. The radial and end restraint spring stiffnesses used are $9 \cdot 10^8$ Nm^{-2} and $2.0 \cdot 10^7$ Nm^{-1} respectively and the load history is as described above. It is seen that for zero friction the bending stress build up to very large values at the end restraint. This is due to secondary bending induced by the tension. As the friction increase, the tendon is kept fixed along the prescribed curve path, thus reducing secondary bending effects. The threshold value for the bending stress is found to be 64 MPa as the friction is increased. This corresponds to the value calculated from Eq.(2.65).

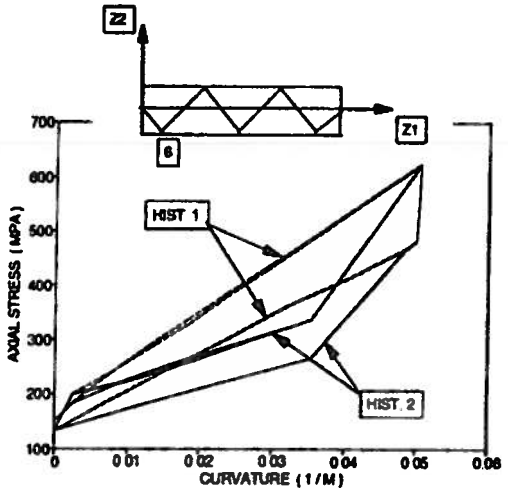

Figure 4.17 Axial stress in node 6 for alternative load histories

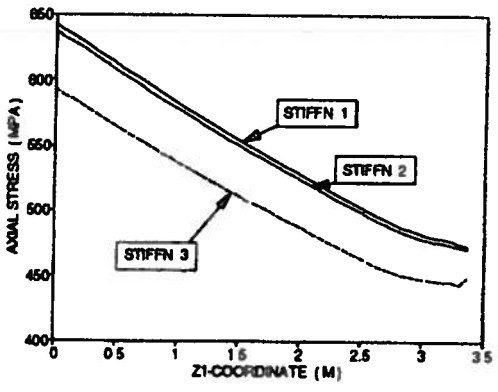

Figure 4.18 Axial stress distributions for alternative radial stiffnesses

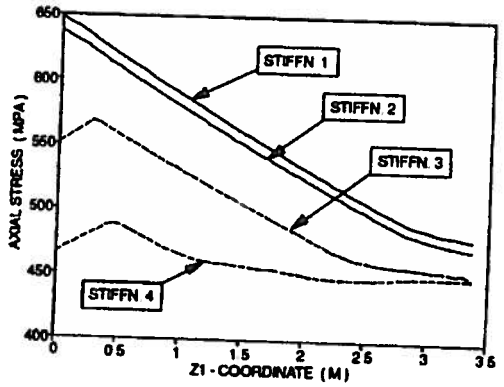

Figure 4.19 Axial stress distributions for alternative end restraint spring stiffnesses

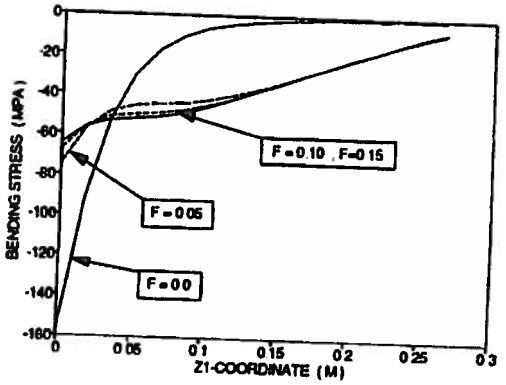

Figure 4.20 Bending stress for alternative coefficients of friction

4.8 Investigation of a 8-inch pipe bending stiffener

4.8.1 Description of example

The purpose of this example is to investigate the stresses and relative displacements in a realistic flexible riser termination. The example chosen is taken from Sødahl [1.4]. An 8-inch flexible riser is installed in a *steep wave* configuration at 120 m water depth and connected to a floater as shown in Figure 4.21. Bending stiffeners are used for connection to the floater and to the sea floor. The wave condition considered is described by a Pierson-Moscowitz wave spectrum with a significant wave height H_s = 14.5 m and a peak period T_p = 16.5 s. In addition, a constant current velocity of 1.0 m/s has been included in the analysis. Both waves and current are acting in the positive x-direction, see Figure 4.21.

By means of the procedure described in [1.4] the stiffness distribution of the bending stiffener has been found. The result is shown in Figure 4.22. According to common design practice, the bending stiffener starts at a distance of 200 mm from the end fitting to avoid stress concentration problems at the point where the tendon enters the end fitting (Confer Section 4.7).

The basic parameters describing the flexible pipe cross section are summarized in Table 4.1. The cross section include two layers of crosswound tensile armouring. The geometrical quantities have been estimated based on the outer diameter and weight specified in [1.4], whereas the strength characteristics have been assumed. It is also assumed that there is an antifriction layer supporting the inner armouring layer, whereas lubrication is present between the two armouring layers. The friction coefficient has been taken as 0.1 between the inner layer and the antifriction layer and 0.05 between the armouring layers. This corresponds to an average in the range 0.07-0.1 according to Sub-section 3.3.2. The internal pressure is assumed to be 200 bar.

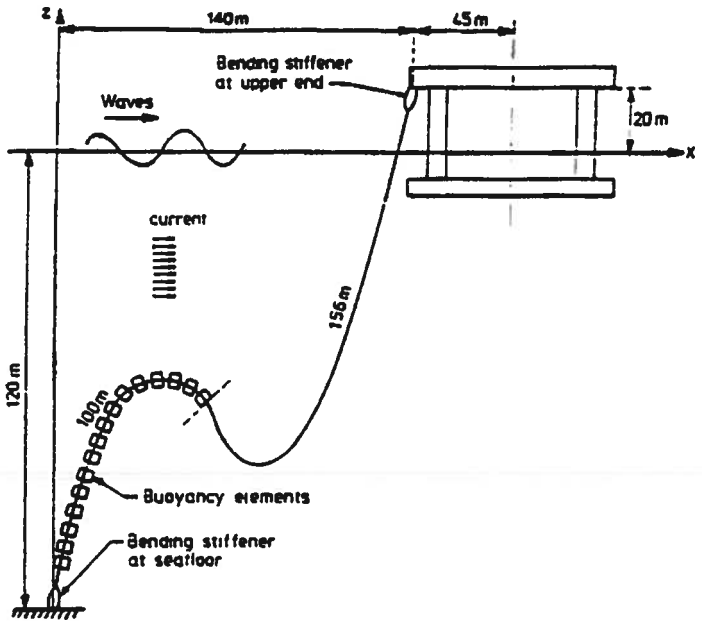

Figure 4.21 8-inch flexible riser installed in a steep wave configuration

 ISBN 82-7119-427-5 ISSN 0802-3271

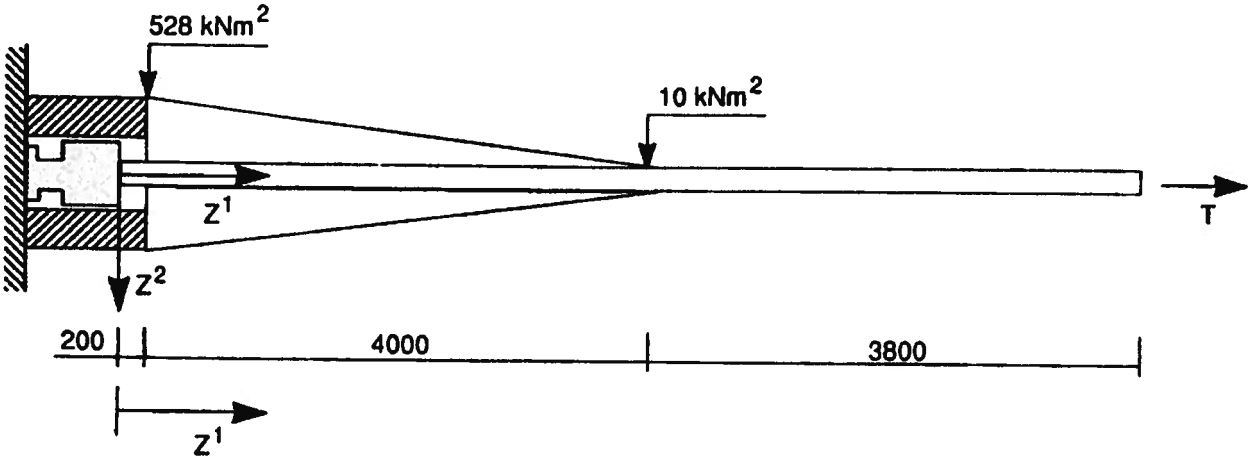

Figure 4.22 Bending stiffener design of 8-inch flexible riser

Table 4.1 Characteristics of 8-inch flexible riser pipe

Parameter		Value
External diameter	(m)	0.294
Mass per unit length	(kgm^{-1})	120.0
Submerged weight per unit length (kNm^{-1})		0.494
Axial stiffness	(kN)	$2.9 \cdot 10^4$
Sliding bending stiffness	(kNm^2)	10.0
Tendon cross section a/b	(mm)	9.0/4.0
Number of tendons Outer/Inner		72/69
Armouring radius Outer/Inner	(mm)	136.0/132.0
Critical curvature radius	(m)	4.0
Ultimate stress	(MPa)	1500.0
Fatigue limit at zero mean stress	(MPa)	500.0
Lay angle Outer/Inner	(deg.)	+35.0/-35.0

 ISBN 82-7119-427-5 ISSN 0802-3271

One cycle of simultaneous tension and curvature histories has been investigated. This cycle is an idealized extreme cycle taken from a 9 hour record of a dynamic simulation in a typical design storm condition. The cyclic description of tension and end angles used in the analyses are shown in Figure 4.23. For each realization of end angle and tension there is a unique curvature distribution [1.4]. By selecting the realizations at 5° end angle intervals throughout the cycle, the curvature distributions of Figure 4.24 are obtained. These are taken directly from the simulations carried out by Sødahl [1.4].

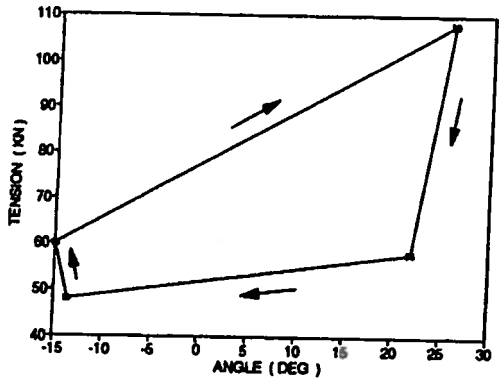

Figure 4.23 One cycle of riser tension and end angle

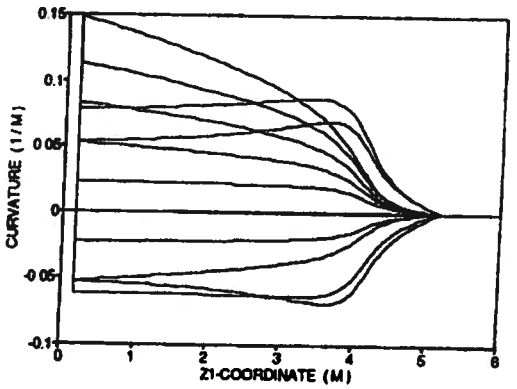

Figure 4.24 Curvature distributions taken at 5° intervals

4.8.2 Method of analysis

In order to predict the distribution of maximum stress ranges in the armouring layers and the distribution of maximum relative displacements between the two armouring layers, the following procedure has been utilized.

CAFLEX [1.6] was first used in order to find the tendon axial stresses due to internal pressure and applied tension, and in order to determine the stiffness properties in the radial direction.

Thereafter the present finite element model was used in order to investigate the tendon behaviour due to bending. AFLEX calculates stresses and displacements in one armouring

tendon exposed to an arbitrary load history defined by axial stresses and corresponding curvature distributions. The calculations carried out in Section 4.6 showed that for periodic loading including shift of curvature direction the stress range was equally predicted by using Coulomb friction and the hyperelastic spring model. In order to investigate this effect in a realistic flexible riser, both spring models were used. The load procedure was determined to implement the true combination of tension and curvature distribution in the actual order of occurance. The load sequence applied in the AFLEX model therefore consisted of a series of tensions and curvature distributions throughout one cycle defined by Figures 4.23 and 4.24.

The AFLEX program can handle only one tendon in an analysis. In order to find the stress and displacement values along the pipe surface, 8 different tendons were investigated, each starting at 45 degrees intervals at the restrained end. The results generated from these calculations were then transformed into a fixed grid which had 8 points over the cross section and 150 points along the pipe. A new refined grid was further generated using 40 points over the cross section. The stress value at each point was calculated by curvilinear interpolation between the 8 point grid. This grid was then used to generate 3-dimensional plots of stress and relative displacement ranges by using the UNIGRAPH 2000 + program [4.1]. The computing time for the complete analysis was approximately 6 hours running 8 work stations (DEC-station 5000/120) in parallel.

4.8.3 Description of numerical model

A pipe section starting at the end fitting and reaching 3.8 m outside the bending stiffener is investigated. This gives a total length of the finite element model of 8 m measured along the pipe axis (Confer Figure 4.22). 200 elements were used which gives an element length of 49 mm.

The stiffness along the surface normal was obtained by CAFLEX to be $2.2 \cdot 10^8$ Nm^{-2} inwards and $5.0 \cdot 10^6$ Nm^{-2} outwards for both layers.

 ISBN 82-7119-427-5 ISSN 0802-3271

Tendon displacements along the surface normal and in the transverse direction and the rotation about the surface normal were all assumed to be zero at the end termination. In the longitudinal direction, a longitudinal spring with stiffness $2 \cdot 10^7$ Nm^{-1} was introduced. At the other end the tendon was fixed only in the surface normal and transverse directions.

4.8.4 Definition of stress and displacement ranges

The stress range between two equilibrium states has been based on using the Von Mises' equivalent stress concept at the corners of the tendon cross section (Confer Figure 4.25). The equivalent stress range $\Delta\sigma_e$ is defined as:

$$\begin{aligned}\Delta\sigma_e=&(\sigma_{11}^2+2\sigma_{11}\Delta\sigma_{11}+\Delta\sigma_{11}^2+\sigma_{22}^2+2\sigma_{22}\Delta\sigma_{22}+\Delta\sigma_{22}^2-\sigma_{11}\sigma_{22}-\Delta\sigma_{11}\sigma_{22}-\sigma_{11}\Delta\sigma_{22}-\Delta\sigma_{11}\Delta\sigma_{22}\\&+3\sigma_{12}^2+6\sigma_{12}\Delta\sigma_{12}+3\Delta\sigma_{12}^2+3\sigma_{13}^2+6\sigma_{13}\Delta\sigma_{13}+3\Delta\sigma_{13}^2)^{\frac{1}{2}}\\&-(\sigma_{11}^2+\sigma_{22}^2-\sigma_{11}\sigma_{22}+3\sigma_{12}^2+3\sigma_{13}^2)^{\frac{1}{2}}\end{aligned} \tag{4.4}$$

where

$$\sigma_{11}=\sigma_a+\sigma_{b2}+\sigma_{b3} \tag{4.5}$$

and where σ_{11} is the total longitudinal stress, with components σ_a (axial stress), σ_{b2} (bending stress caused by bending about the X^2 axis) and σ_{b3} (bending stress caused by bending about the X^3 axis). σ_{22} is the contact pressure, whereas σ_{12} and σ_{13} are the shear stresses caused by twist. Δ indicates that the stresses are the maximum ranges found between two equilibrium states being obtained by checking alternative load steps during loading and unloading.

The corresponding relative displacement ranges were further found by considering Figure 4.26 where the first subindex on u defines the direction of displacement along the axes X^1 and X^3

and the second subindex defines the considered layer. The relative displacement Δu_{rel} is defined by the following equation:

$$\Delta u_{rel}=(\Delta u_{11}^2+\Delta u_{12}^2-2\Delta u_{11}\Delta u_{12}\cos 2\alpha+\Delta u_{31}^2+\Delta u_{32}^2-2\Delta u_{31}\Delta u_{32}\cos 2\alpha$$
$$-2\Delta u_{12}\Delta u_{31}\sin 2\alpha+2\Delta u_{11}\Delta u_{32}\sin 2\alpha)^{\frac{1}{2}} \qquad (4.6)$$

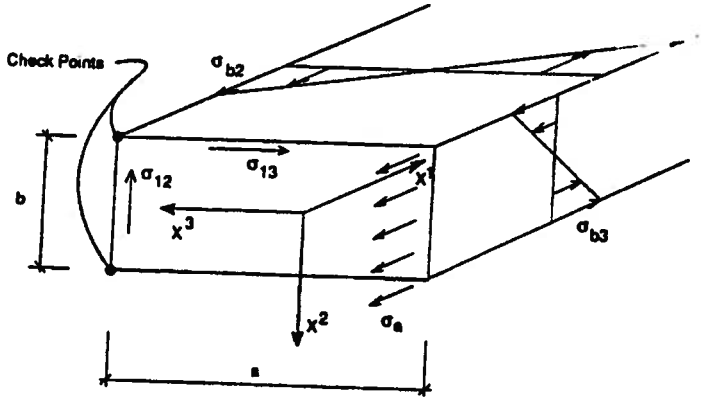

Figure 4.25 Definition of stress components

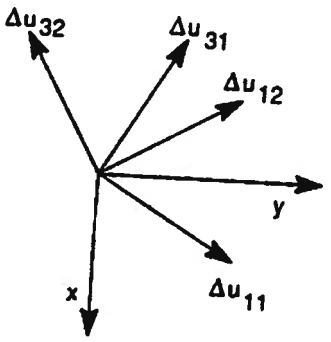

Figure 4.26 Definition of displacement components

4.8.5 Results from initial analyses

Table 4.2 gives the tendon axial stresses for the armouring layers and the contact pressure occuring between the armouring layers as obtained by CAFLEX for different alternative tension levels and for 200 bar internal pressure.

Table 4.2 Axial stresses due to axisymmetric loading of 8-inch flexible riser pipe

Quantity	T=0.0kN	T=70 kN	T=108 kN
Axial stress σ_a Outer layer (MPa)	206	222	231
Axial stress σ_a Inner layer (MPa)	243	260	269
Contact pressure σ_{22} (MPa)	2.1	2.3	2.4

4.8.6 Presentation and discussion of maximum stress ranges

The distribution of the maximum stress ranges along the first 6 m of the inner and outer armouring layers are shown by contour plots in Figures 4.27 and 4.28 for the outer and inner layers respectively. In these figures the pipe has been rotated 90 degrees away from the reader, so that the tensile side of the pipe is positioned at $Z^3 = 0$, closest to the reader.

It was found that the maximum stress ranges were equally predicted for the two spring models and the maximum stress ranges were found to be determined by the combination of maximum end angle/ tension and the minimum end angle/tension equilibrium states.

It is seen that the largest stress ranges will occur in the inner layer. The largest stress range is found for the tendon at the neutral axis at the point where the curvature starts. This tendon is directed towards the tensile side of the pipe at this point. The maximum stress range was found to be 592 MPa, of which 68% was axial stresses induced by friction and 32% was due to bending about the surface normal. The large amount of friction induced axial stresses is caused by the axial displacement needed to compensate the increased length of the first quarter pitch from curvature. Since the tendon starts at the neutral axis, there is no neighbouring compressive pipe section. The increased path length along the tensile side must therefore be

compensated by feeding tendon from sections further away, thus giving increased friction induced stresses (see Figure 4.28). Since the inner layer has higher contact loads, this layer will have the highest stresses.

By linear interpolation in the Haig diagram, the maximum allowable value based on non exceedance of the fatigue limit was found to be 400 MPa, which is far below the predicted stress range.

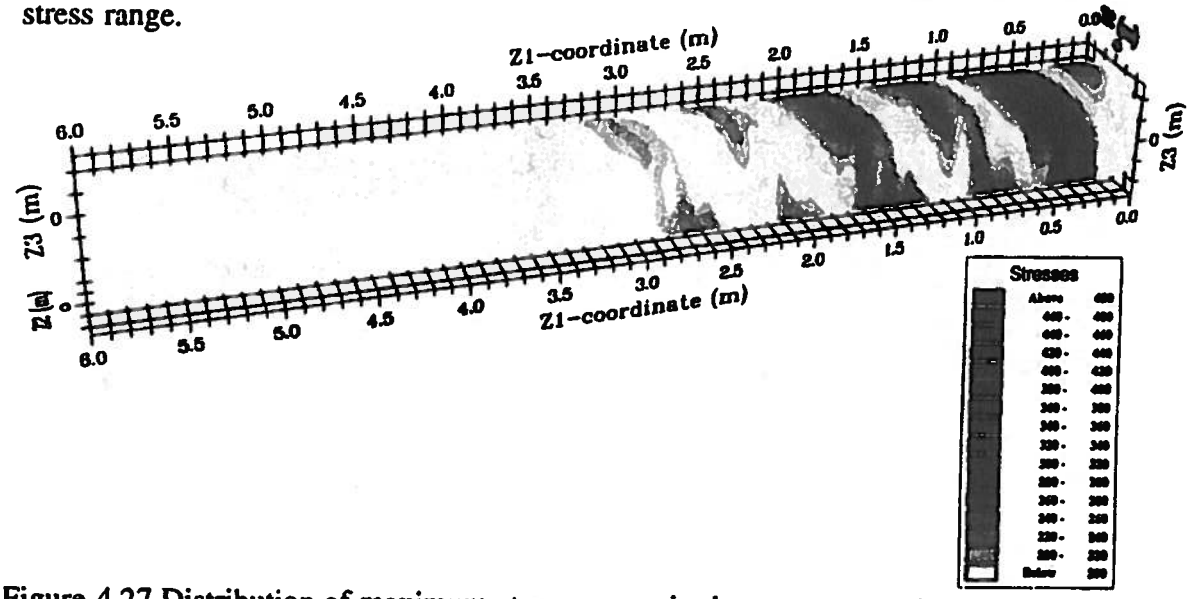

Figure 4.27 Distribution of maximum stress ranges in the outer armouring layer of the 8-inch riser

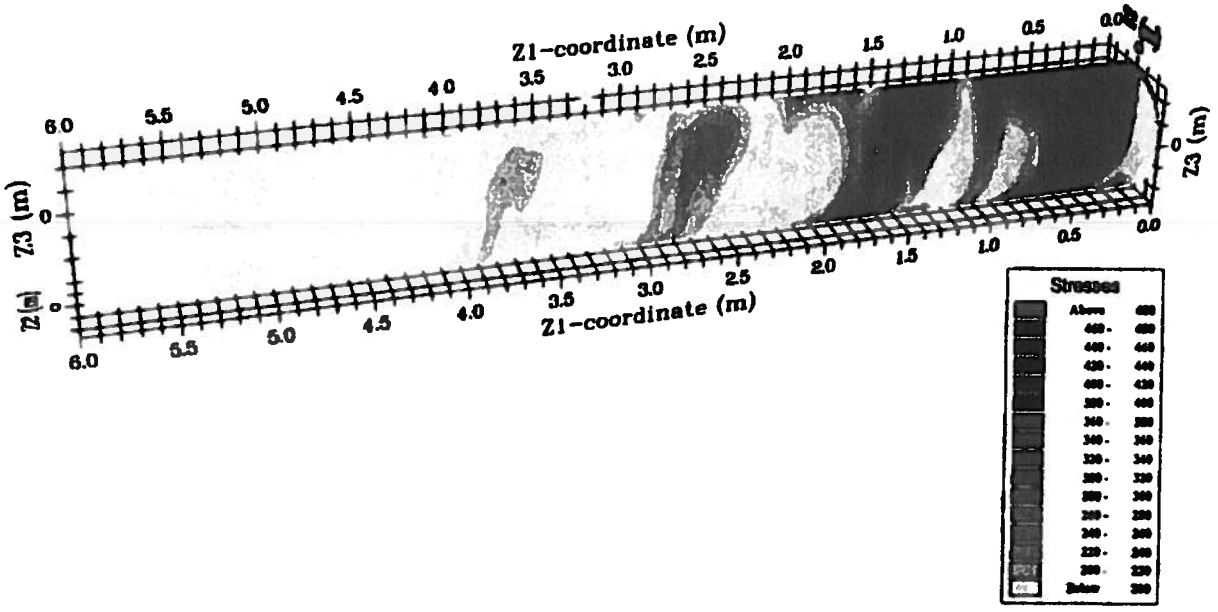

Figure 4.28 Distribution of maximum stress ranges in the inner armouring layer of the 8-inch riser.

ISBN 82-7119-427-5 ISSN 0802-3271

4.8.7 Presentation and evaluation of maximum displacement ranges

The distribution of the maximum relative displacement ranges occuring between the two armouring layers along the first 6 m of the model are shown by contour plot in Figure 4.29. In this figure the pipe has been rotated 90 degrees towards the reader, so that the compressive side of the pipe is positioned at $Z^3 = 0$, closest to the reader.

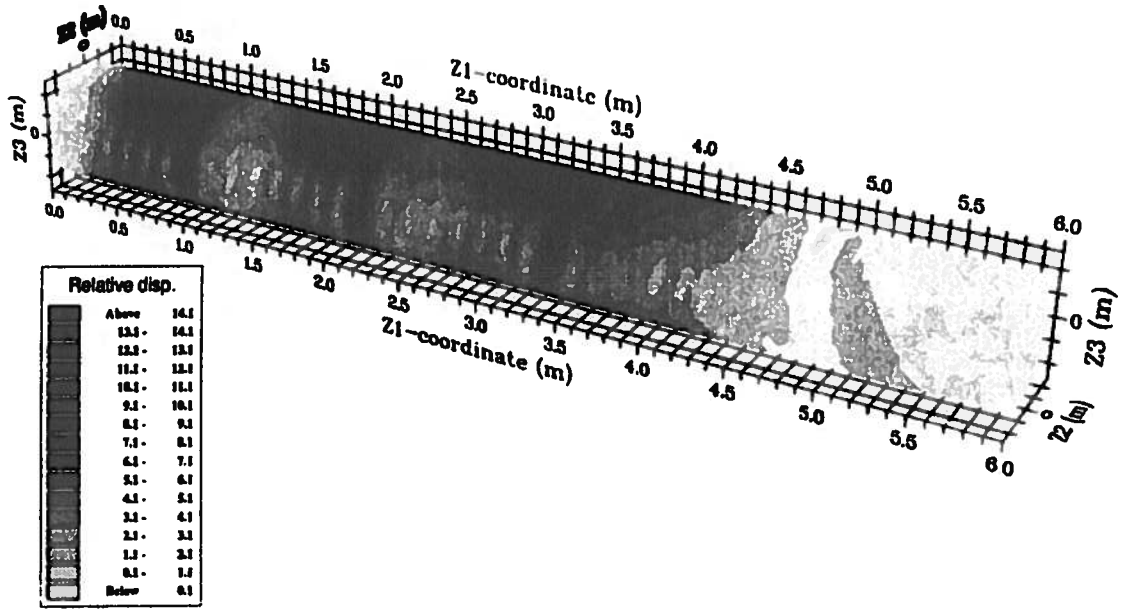

Figure 4.29 Distribution of relative displacement ranges for the 8-inch flexible riser

It is seen that the maximum relative displacement ranges occur along the neutral axis of the pipe as expected. The maximum relative displacement found was 12.3 mm. Investigation of the numerical values showed that for the inner layer, the slip is dominated by longitudinal displacements. This is due to high contact loads inducing large friction forces that will tend to suppress transverse displacements. For the outer layer, however, and at the point of maximum slip, 40% of the slip was caused by transverse displacements which is due to less contact loads and hence also friction forces for this layer.

5 DISCUSSION OF EXISTING MATHEMATICAL MODELS

5.1 Introduction

In this Chapter, the existing models for predicting the behaviour of flexible pipe cross sections will be discussed with major focus on the innovative theory developed by Feret et. al. [1.17]. This theory represents the basis for the CAFLEX computer program, for which detailed documentation has been available [1.6]. The CAFLEX program was developed during 1989 for STATOIL as a cooperation between SINTEF (Trondheim) and IFP (Paris). Another basis for this discussion is experimental results that have been published from the FPS-2000 project, see Skallerud [5.1], [5.2]. For general information of the FPS-2000 project, confer Olufsen [5.3].

The CAFLEX theory will be discussed and compared with other formulations as presented in papers [1.18]-[1.32] and the theory presented in Chapter 2. This will also include comparisons between the results obtained by the CAFLEX model and results presented in Chapter 4. By considering the deviations between test results and the CAFLEX computations reported in [5.1]-[5.2], the present theory has been used to suggest improvements in the CAFLEX model. These improvements were implemented into the CAFLEX program, February 1992 [5.4] with promising results.

 ISBN 82-7119-427-5 ISSN 0802-3271

5.2 Presentation and discussion of existing models

5.2.1 Axisymmetric behaviour

The axisymmetric model is used to predict the stresses in each layer of bonded and nonbonded flexible pipes occuring from tension, torque and internal/external pressure, and to estimate cross section parameters for global analyses, such as axial stiffness and torsion stiffness.

Since pressure, tension and torque loads do not change the shape of the pipe cross section, the assumption of axisymmetric behaviour can be used and relatively simple relations can be obtained to predict strains and stresses in each layer. The governing equations are based on equilibrium, a material law and kinematic relations. The theory is outlined in detail in [1.6] and will not be fully repeated here. The basic principle is based on equilibrium consideration of one pipe element exposed to internal and external pressure, a tensile/compressive force and a torque as shown in Figure 5.1. Each physical layer of the pipe is represented by one internal element, for which local equilibrium equations are established. There are two different element types, the sheath element and the helix element. The sheath element is used to simulate pressure carrying tubular layers whereas the helix element is used for the carcass, zeta-spiral and the armouring layers.

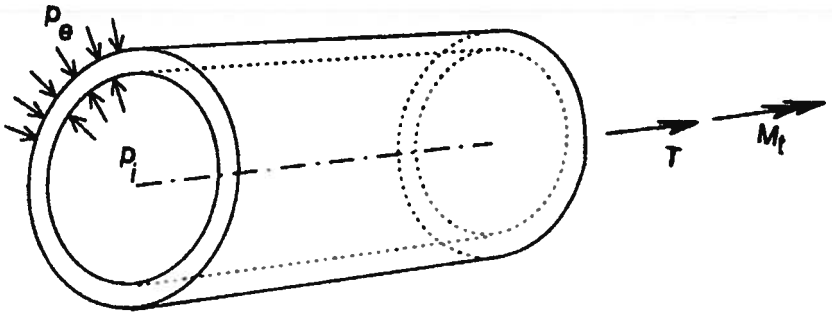

Figure 5.1 Pipe element

For the sheath element, equilibrium equations are established by regarding longitudinal, radial and circumferential forces and the torque. Hooke's law is further assumed, i.e the material is assumed to be linearly elastic in the relevant range of material straining and to have equal properties in all directions.

McNamara and Harte [1.18] allow orthotropic material behaviour of the tubular layers, i.e. the layer is allowed to have different properties in the circumferential and longitudinal directions. Due to the low stiffness of the tubular layers compared to the steel layers, however, the large part of the axisymmetric loads will be carried by the steel layers where the most critical stresses therefore will occur. An improved accuracy on the material law applied for the tubular layer, will consequently be of limited value.

Thin shell theory is used to describe kinematic relations, and together with the equilibrium equations and material law one can derive the final relations between load condition and displacements and stresses.

Equilibrium of the helix element is based on the theory of thin curved rods as described in Section 2.3. When the pipe is exposed to axisymmetric loads, the tendon will still describe a helix and the transverse curvature κ_2 and all differentials will therefore vanish. Further, among all the applied forces and moments only the distributed contact line load q_2 will be different from zero, which imply that the problem reduces to the two following equilibrium equations:

$$\kappa_3 Q_1 - \kappa_1 Q_3 + q_2 = 0 \tag{5.1}$$

$$\kappa_3 M_1 - \kappa_1 M_3 - Q_3 = 0 \tag{5.2}$$

Eq.(5.1) represents the force equilibrium equation in the radial direction whereas Eq.(5.2) represents the moment equilibrium equation about the surface normal. These two equilibrium equations can be used to eliminate the unknown contact pressure q_2 and shear force Q_3 once the other quantities are expressed as a function of twist and curvature induced by the axisymmetric loading. In CAFLEX only the axial force Q_1 was originally taken into account, as the changes in torsion and normal curvature induced by axisymmetric loads were assumed

 ISBN 82-7119-427-5 ISSN 0802-3271

to be small. In the model presented by Witz and Tan [1.20] and the work made by Costello et. al. [1.23]-[1.27], these terms were included. In Sub-section 5.3.1, equations describing these effects have been developed on the basis of the theory outlined in Chapter 2. The section also includes an evaluation of their importance.

For the helix element, Hooke's material law is again assumed. This law is however modified in the case of bonded pipe reinforcement in order to take into account the fact that this armouring is made of thin helically wound strands giving different moduli in the longitudinal and transverse directions.

The kinematic quantities are expressed by considering the motions of an element in longitudinal, radial and circumferential directions assuming the cross section shape to remain circular under all types of loads.

A distinction is made between bonded and nonbonded pipes with regard to the circumferential strains in the helical windings due to pressure. This is necessary as the armouring layers of a bonded pipe is surrounded by rubber, having a Poisson's ratio close to 0.5. This implies that under pressure, the rubber will behave like a fluid having equal stresses in all directions. A steel layer between pressure barriers in a nonbonded pipe will not have circumferential stresses whereas the corresponding layer in a bonded pipe will have equal radial and circumferential stress components. This is visualized in Figure 5.2.

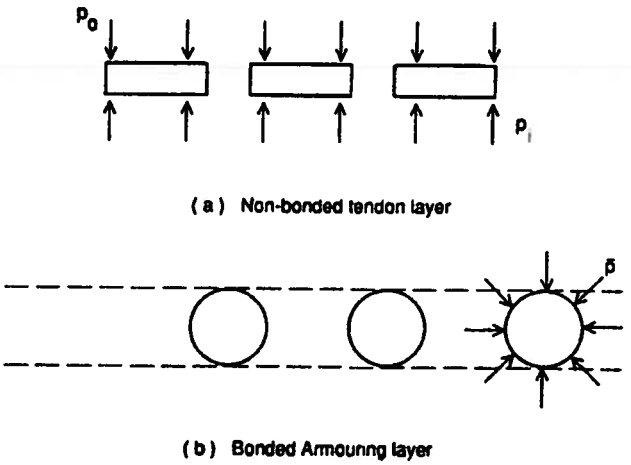

Figure 5.2 Circumferential stresses

The rubber between armouring layers in bonded pipes will tend to be squeezed outwards due to internal pressure. This gives shear loading of the rubber inducing an associated circumferential strain component in the steel tendon. According to Often and Løtveit [1.19] this will give a redistribution of stresses in each armouring layer, tending to reduce the stresses in inner armouring layers and increase the stresses in the outer layers.

The physical interpretation is that due to the increased tensile transverse strain there will be an associated compressive strain in the longitudinal tendon direction due to the Poisson effect. In order to compensate the resulting reduction in tensile stress in the inner layers, the outer layers tensile stress must increase. Thus a more even distribution of radial load transfer will result. Often and Løtveit thus conclude that a nonbonded model does not provide sufficient accuracy for a bonded pipe.

The established equation system is based on local and global equilibrium and the restraints induced by the gaps that may occur between layers. This leads to an equation system with $6n+2$ unknowns, where n is the number of layers. The equations are obtained as follows:

For each layer there are three equations on layer level that takes care of equilibrium between internal and external forces in longitudinal, circumferential and radial directions. Similarly there is a local moment equilibrium equation linking the external torque to the contribution from each layer. This gives $4n$ equations.

In addition there are four equilibrium equations on global level, linking the total contribution from all layers to total axial force, torque and internal pressure and external pressure. This gives 4 additional equations.

By consideration of the gap between layers, $n-1$ relations are established, expressing the size of the gap explicitly.

Depending on positive or negative gaps there are $n-1$ additional relations. If the gap is negative, the gap is set to zero. If it is positive, the pressure between the layers equals the local pressure, which is zero between pressure barriers.

 ISBN 82-7119-427-5 ISSN 0802-3271

This gives in total $6n+2$ unknowns. It is noted that the last $n-1$ relations must be established by means of iteration.

5.2.2 Bending behaviour of nonbonded pipes

The CAFLEX bending model for nonbonded pipes is based on assuming constant pipe curvature and serves the following purposes:

To determine the friction moment.
To determine the sliding bending stiffness.
To calculate the minimum radius of curvature.
To predict stresses induced by bending.
To estimate fatigue and wear.

Prediction of friction moment and bending stiffness

The basic assumption made in the CAFLEX model for nonbonded pipes regarding the prediction of friction moment and sliding bending stiffness, was originally that the tendon would move to the geodesic when the tendons are prestressed due to internal pressure. In Chapter 2 it was shown that a basic property of the geodesic is that it represents the minimum distance between two points on a surface and that the curve normal vector is parallel to the surface normal vector, thus having no transverse curvature. In order to go towards the geodesic during bending, both longitudinal and transverse slips relative to the supporting pipe structure are needed. The physical interpretation of this result is that the longitudinal slip eliminate longitudinal straining, and that the transverse slip eliminate transverse curvature. The geodesic thus represents an upper limit for the tendon/pipe relative displacement. It was, however, shown in Chapter 4 that the transverse slip will be limited by friction forces. In the case study of the 8-inch flexible riser presented in Section 4.8, transverse displacements were eliminated for the inner layer and reduced for the outer layer.

 ISBN 82-7119-427-5 ISSN 0802-3271

The above has been verified by observations made during testing of flexible pipes reported in [5.1]. One observation during these tests is that the sliding bending stiffness increased as the internal pressure was raised, whereas CAFLEX predicted a constant value. This can be explained by the fact that since the tendon tend to be directed along the loxodromic curve rather than the geodesic, transverse curvature of the tendon will occur. If the tendon is prestressed due to internal pressure, tension or torque, a geometric or initial stress stiffness will occur in each tendon that will increase the resistance against transverse deformation. This will be seen as an increased bending stiffness of the overall pipe cross section. It is noted that this *initial stress stiffness effect* has no connection to the global initial stress stiffness due to global effective tension.

Another observation from the tests is that the friction moment was a factor 2.8 (in average) less than the value predicted by CAFLEX when using a friction coefficient according to [1.7] of 0.07. The CAFLEX model for predicting the friction moment was originally based on a simple energy approach considering the friction forces and the sliding of the tendon along the geodesic. Since the geodesic represents an upper limit for tendon displacements, the CAFLEX theory will give an upper bound estimate of the friction moment. Both the sliding bending stiffness and the friction moment are important input parameters to the global analyses. Improved methods of predicting these parameters have therefore been suggested in Sub-sections 5.3.2 and 5.3.3, respectively.

Prediction of stresses due to bending

The following stress components are considered by CAFLEX:

Axial stress due to tension variation.
Axial stress due to friction.
Bending stress due to normal curvature increment.

The axial stress due to tension is found from axisymmetric analysis. The friction induced stress is found by considering the friction forces occuring along one quarter pitch, assuming a harmonic longitudinal slip as for the geodesic solution (Confer Eq.(2.29)). The bending

stress is based on the geodesic solution according to Eq.(2.32). In the CAFLEX manual [1.6] it is clearly stated that the bending stresses are valid only for pipe sections being sufficiently far away from end restraints. To demonstrate the relevance of this limitation, a comparison has been made between the results obtained by the CAFLEX model and the results from the case study of the 8-inch flexible riser presented in Section 4.8. The results from this comparison is presented in Table 5.1.

Table 5.1 Comparison of stresses between CAFLEX and AFLEX

Stress components (MPa)	CAFLEX	AFLEX
$\Delta\sigma_{at}+\Delta\sigma_{ac}$	120	405
$\Delta\sigma_{b2}$	0	187
$\Delta\sigma_{b3}$	169	≈ 0
$\Delta\sigma_{tot}$	289	592

where $\Delta\sigma_{at}$ and $\Delta\sigma_{ac}$ are the axial stress ranges caused by tension and global curvature respectively. $\Delta\sigma_{b2}$ and $\Delta\sigma_{b3}$ are the bending stress ranges caused by transverse and normal curvature whereas $\Delta\sigma_{tot}$ is the total stress range. It is seen that the total dynamic stress range obtained by CAFLEX is 52% less than the value predicted by AFLEX. This is mainly caused by the end restraint effect giving an increased axial stress due to friction. It is also seen that the position of maximum stress is different. The CAFLEX formulation assumes that the maximum bending stress occurs due to normal curvature and friction at the tensile/compressive sides of the pipe, whereas the maximum found by the AFLEX analyses occurs from transverse curvature and friction close to the neutral axis of bending at the end restraint. The above demonstrates that the CAFLEX program as anticipated cannot be used to calculate stresses close to the end fitting.

Lifetime estimation

According to the theory implemented in CAFLEX the lifetime of a nonbonded flexible pipe may be determined from the minimum of the following values:

The time corresponding to aging of the thermoplastic materials.
The time needed to reduce the tendon thickness by adhesive wear to such an extent that either the mean stress exceeds a predefined portion of the ultimate stress or the dynamic stress range exceeds the Goodman line in the Haig diagram.

The effect of fretting on the fatigue limit is not considered. The Archard formula is used to predict the thickness reduction per year (see Eq.(3.1). The relative displacements during bending are further estimated by assuming that the tendon moves towards the geodesic as described by Eq.(2.29) and Eq.(2.30). By inserting Eq.(2.29) and Eq.(2.30) into Eq.(4.6) the relative displacement range between two crosswound armouring layers is found to be:

$$\Delta u_{rel} = 4 \frac{R^2}{\rho} \frac{1}{\tan\alpha} \tag{5.3}$$

which is in accordance with the formula given in the CAFLEX manual. By using the above equation for the example presented in Section 4.8, a relative displacement of 22.6 mm is obtained. This is 83% larger than the value predicted by AFLEX. This indicates that conservative estimates is obtained by the analytical formula. This is caused by the fact that friction forces will reduce the transverse displacements in the real case. By assuming longitudinal slip only, confer Tan et. al. [1.31] and Eq.(2.29), the corresponding value will be 7 mm, which is 43% lower than the AFLEX value. A nonconservative estimate is therefore obtained by their approach.

5.3 Improvements of the CAFLEX model

As mentioned in Sub-section 5.2.1, some simplifications were made in the CAFLEX program such as neglecting local forces and moments due to the small change in lay angle, layer radius and centre line elongation induced by axisymmetric loads. In addition, for the bending tests reported in [5.1], the following discrepancies were found between observed and predicted values:

The friction moment calculated by CAFLEX is larger than the measured values.
The measured sliding bending stiffness seems to increase with increasing internal pressure.

In the following, equations are proposed to describe the above effects.

5.3.1 The effect of local forces and moments

Reference is given to Eq.(5.1) and Eq.(5.2). In Eq.(5.1), the tendon axial force Q_l can be found by studying the axial strain ε_l of the tendon centre line as a function of pipe axial displacements, local radial displacements and global twist given as:

$$\varepsilon_l = \varepsilon_z \cos^2\alpha - \frac{u_2}{R} \sin^2\alpha + R\theta_{,z} \sin\alpha \cos\alpha \qquad (5.4)$$

where all parameters are defined in Figure 5.3.

The moments M_1 and M_3 are found by using the theory developed in Chapter 2. From this theory, the twist and normal curvature increment obtained when moving from the reference stress free state to the deformed equilibrium state can be expressed as:

 ISBN 82-7119-427-5 ISSN 0802-3271

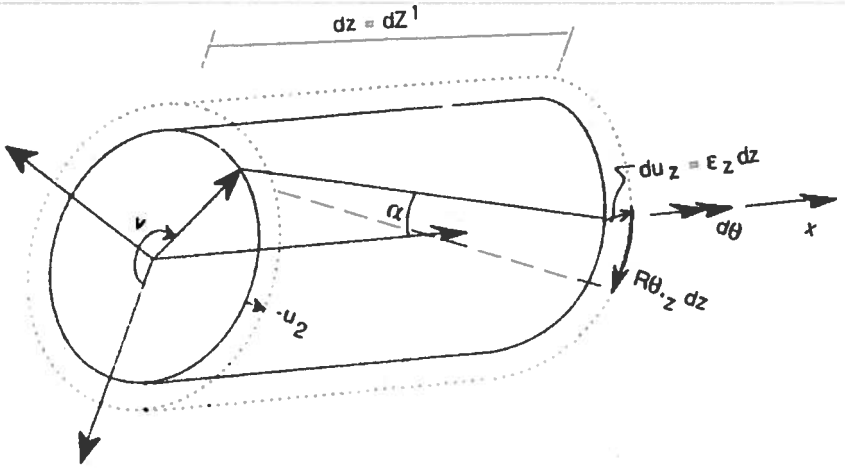

Figure 5.3 Geometrical relations

$$\Delta\kappa_1 = \kappa_1 u_{1,1} + (\kappa_3 - \kappa_t) u_{3,1} + \kappa_1 \kappa_3 u_2 \tag{5.5}$$

$$\Delta\kappa_3 = -2\kappa_1 u_{3,1} - (\kappa_1)^2 u_2 + \kappa_3 u_{1,1} \tag{5.6}$$

where κ_t is the surface curvature in the transverse direction. It is noted that these expressions give different results than found by Witz and Tan [1.20]. The reason is that Witz and Tan express the new accumulated torsion and curvature by using the updated lay angle and layer radius and then insert these quantities directly into Eqs.(2.13)-(2.14), obtained for a helix. This excludes consideration of centre line straining that will induce both twist and normal curvature change.

By studying the displacement and strain components along the local coordinate axes shown in Figure 5.4, the displacement differentials are obtained as:

$$u_{1,1} = \varepsilon_z \cos^2\alpha + R\theta_{,z} \sin\alpha \cos\alpha \tag{5.7}$$

$$u_{3,1} = \varepsilon_z \cos\alpha \sin\alpha - R\theta_{,z} \cos^2\alpha \tag{5.8}$$

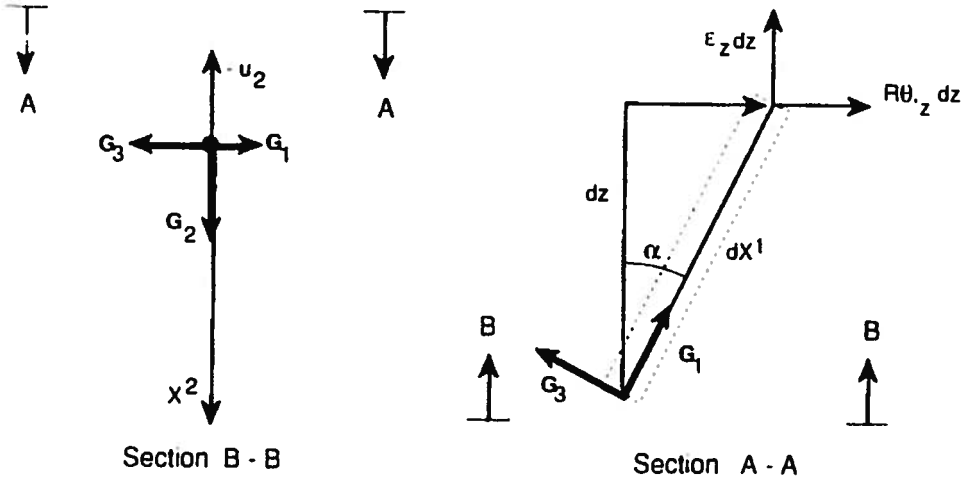

Figure 5.4 Components of deformation in local system

By inserting Eqs.(5.7)-(5.8), Eqs.(2.13)-(2.14) and Eq.(2.35) into Eqs.(5.5)-(5.6), the following results are obtained:

$$\Delta\kappa_1 = \frac{\sin\alpha\cos\alpha}{R}(\varepsilon_z\sin^2\alpha + R\theta_{,z}\frac{\cos^3\alpha}{\sin\alpha} + \sin^2\alpha\frac{u_2}{R}) \tag{5.9}$$

$$\Delta\kappa_3 = \frac{\sin^2\alpha}{R}(-\varepsilon_z\cos^2\alpha + R\theta_{,z}(2\frac{\cos^2\alpha}{\tan\alpha} + \sin\alpha\cos\alpha) - \cos^2\alpha\frac{u_2}{R}) \tag{5.10}$$

By use of Eq.(5.4), Eq.(5.9) and Eq.(5.10), the moments M_1 and M_3 and the axial force Q_1 are found by:

$$Q_1 = C_\sigma A\ \varepsilon_1 \tag{5.11}$$

$$M_1 = C_\tau I_t\ \Delta\kappa_1 \tag{5.12}$$

$$M_3 = C_\sigma I_3\ \Delta\kappa_3 \tag{5.13}$$

By using Eq.(5.1) and Eq.(5.2) and decomposition of the axial force Q_1 and the shear force Q_3 in the respective pipe directions, the following total global force and torque from the n tendons in a layer are obtained.

$$T = n\,(Q_1 \cos\alpha + (\kappa_3 M_1 - \kappa_1 M_3)\sin\alpha) \tag{5.14}$$

$$M_t = n\,(Q_1 R\sin\alpha + M_1\cos\alpha + M_3\sin\alpha - (\kappa_3 M_1 - \kappa_1 M_3) R\cos\alpha) \tag{5.15}$$

The above expressions are linearized as the current torsion and normal curvature are assumed to remain equal to the initial ones. This is considered to be reasonable since the strains induced by axisymmetric loading generally are small. The importance of the above corrections are illustrated by an example presented in Figure 5.5. The figure shows the local bending stress due to change in normal curvature as a function of the global longitudinal strain ε_z, for alternative tendon thicknesses. The layer radius is 73 mm and the lay angle is 35°. It is seen that for moderate global strain levels, the stresses are small even for a tendon thickness of 9 mm which is larger than normally applied in a flexible pipe.

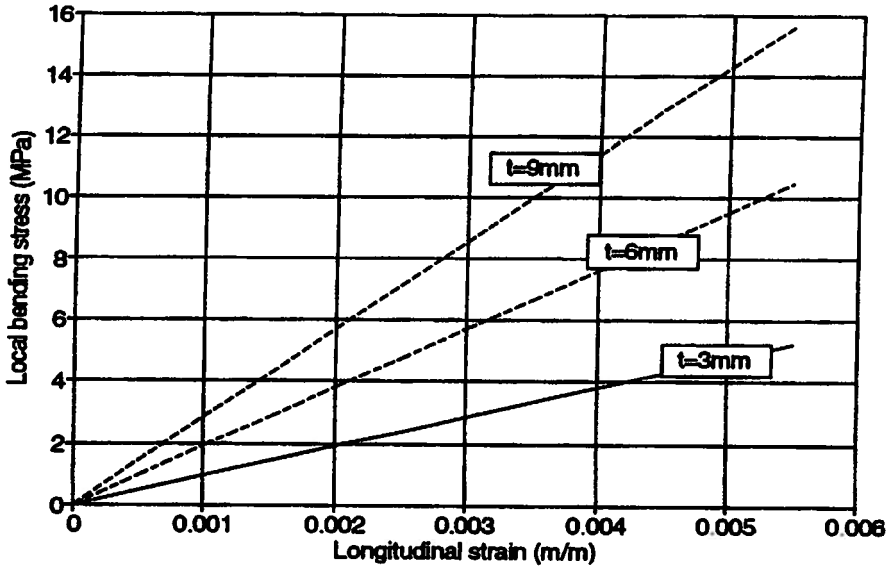

Figure 5.5 Normal curvature stress

5.3.2 The initial stress stiffness effect

During the bending tests reported in [5.1], it was found that by increasing the internal pressure from 7 to 250 bar, the average sliding bending stiffness was increased by 5.3 kNm^2 from 21.9 kNm^2 to 27.2 kNm^2 The physical interpretation of this is that the tendon will follow the loxodromic curve rather than the geodesic during bending. Since the tendon is prestressed, a

local initial stress stiffness will introduce an increased resistance against transverse curvature. The sideways displacement difference between these two limit curves can be expressed by Eq.(2.30) as:

$$u_3=\frac{R^2}{\rho\tan\alpha}\left(2\sin\alpha+\frac{\cos^2\alpha}{\sin\alpha}\right)\sin v \tag{5.16}$$

The virtual work contribution from the axial load Q_1 in the tendon along one pitch is determined by:

$$W_i=\int_0^{2\pi} Q_1 u_{3,1}\delta u_{3,1}\frac{R}{\sin\alpha}dv \tag{5.17}$$

With reference to Figure 5.6, the corresponding external virtual work reads:

$$W_e=\frac{\Delta EI}{\rho}\delta\varphi \tag{5.18}$$

where ΔEI is the increase in bending stiffness from one tendon. By equating the two expressions and by summation for all n tendons and m armouring layers, the total increase in bending stiffness ΔEI_{tot} is obtained as:

$$\Delta EI_{tot}=\sum_{j=1}^{m}\sum_{i=1}^{n}\frac{Q_1^{ij}R_j^2}{2}\left(9\cos^4\alpha_j\sin^2\alpha_j+6\cos^6\alpha_j+\frac{\cos^8\alpha_j}{\sin^2\alpha_j}+\frac{\cos^4\alpha_j}{\sin^2\alpha_j}+4\right) \tag{5.19}$$

The above equation gives an increase in bending stiffness of 7.4 kNm^2 for the test reported in [5.1] which is within the variation observed for each individual test.

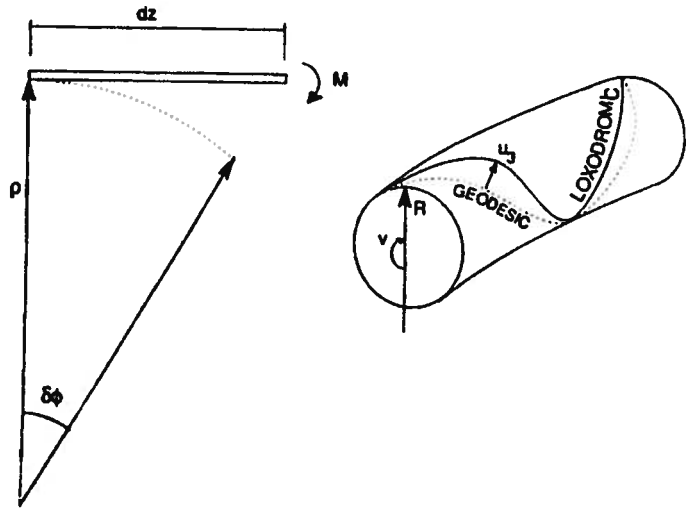

Figure 5.6 Theoretical Model

5.3.3 The friction moment

The observed average friction moment under 250 bar internal pressure reported in [5.1] was 1.0 kNm. This represents a reduction by a factor of 2.8 compared to the result predicted by CAFLEX when using 0.07 as friction coefficient between the armouring layers. As stated in the previous sub-section, the sideways displacements will be restrained by friction, implying that the displacements between the tendon and the supporting pipe will mainly occur in the longitudinal direction. Assuming a constant radius as above, the longitudinal displacement is given from Eq.(2.29) as:

$$u_l = \frac{R^2}{\rho} \frac{\cos^2\alpha}{\sin\alpha} \sin\nu \tag{5.20}$$

The internal work performed by the friction forces along one tendon during one half pitch can be expressed as:

$$W_i = \int_0^{\pi} \Sigma q_2 \mu \, \delta|u_1| \frac{R}{\sin\alpha} \, dv \tag{5.21}$$

where the summation symbol denotes that the lineloads induced by contact pressures at the tendon inner and outer surfaces have been included. Further, due to a moment M_f balancing the friction moment:

$$W_e = M_f \, \delta\varphi \tag{5.22}$$

By equating the internal and external work and by summation over all tendons in a layer, the following friction moment M_f developed between one armouring layer and the sheath is obtained:

$$M_f = \frac{4 \cos\alpha}{\tan\alpha} \frac{R^3}{b(1+h)} \Sigma q_2 \mu \tag{5.23}$$

where h is the gap between each tendon divided by the width of the tendon. Similarly between two neighbouring armouring layers with opposite but equal lay angles

$$M_f = \frac{8 \cos^2\alpha}{\tan\alpha} \frac{R^3}{b(1+h)} \Sigma q_2 \mu \tag{5.24}$$

The above expressions give a friction moment of 1.14 kNm, which is in good agreement with the observed value.

 ISBN 82-7119-427-5 ISSN 0802-3271

6 EXPERIMENTAL STUDIES

6.1 Introduction

The main purpose of this Chapter is to present verification studies carried out by comparing stresses obtained by the numerical model developed in Chapter 2 with stresses measured by strain gauges on one tendon of a 4-inch internal diameter (ID) nonbonded pipe. These tests were carried out in September 1991 as a part of this study. The specimen used in this test will in the following be referred to as Pipe 1.

During 1991-1992 fatigue testing was carried out on two pipes, including the specimen mentioned above and one additional 4-inch ID nonbonded pipe from another producer. These tests were carried out as a part of the FPS-2000 program and used here as a reference. The second specimen will in the following be referred to as Pipe 2.

Both pipes were initially exposed to 10^6 cycles of a specified fatigue test program. These cycles did not result in fatigue failure of any specimen. Thereafter the load amplitudes were increased in order to create fatigue and the pipes were tested until fatigue failure occured. The fatigue failures of tendons were observed from outside as twist induced "cork-screw" deformation of the pipes.

The second purpose of this Chapter is to evaluate and explain the observed fatigue failure modes of both test pipes. Since the fatigue failures were observed as severe twist deformation

 ISBN 82-7119-427-5 ISSN 0802-3271

of the overall test pipe structure, it was not possible to know *when* the first tendon failed. It was therefore not possible to relate the fatigue failures to *S-N* data and hence the theoretical evaluations had to be qualitative, rather than quantitative.

6.2 Description of test rig

The test rig arrangement used in all experiments is illustrated in Figure 6.1.

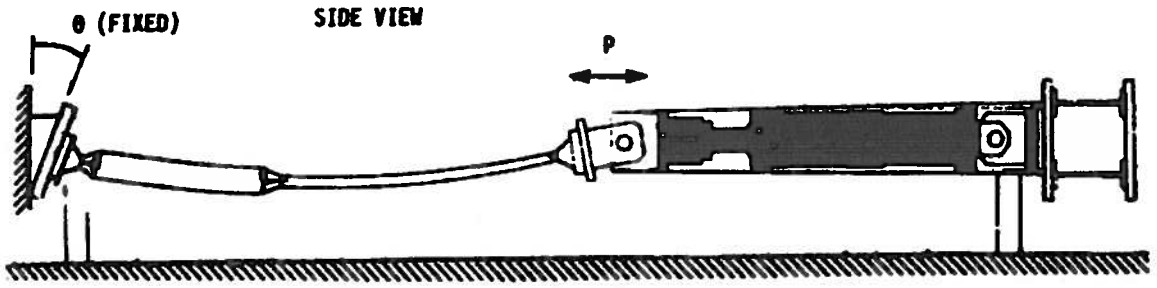

Figure 6.1 Test rig set-up

The test pipes were horizontally mounted in a steel frame rig. One end of the pipe was fixed to the steel frame at a predefined angle θ. Axial force in the pipe was applied at the opposite end, using a 500 kN servohydraulic actuator. Note that this arrangement gives a combination of axial force and moment at the fixed pipe end. This is a realistic modelling of the boundary condition seen for real flexible riser application. Spherical bearings were further mounted between the pipe flange and the actuator. Hence, negligible bending moment were expected at this end, and torque was eliminated in the pipe. In testing mode, the actuator was operated in close loop load control monitored by the actuator load cell.

 ISBN 82-7119-427-5 ISSN 0802-3271

6.3 Description of test specimens

The key parameters needed to describe the structural properties of the two test pipes were obtained partly by experiments as reported in [5.1]-[5.2] and partly by using the CAFLEX program. The key values used for the present analyses are given in Table 6.1.

The friction coefficients between the inner and outer armouring surfaces were obtained by calibrating the friction moment obtained from the new version of CAFLEX (see Sub-section 5.3.3) against the value obtained from the testing [5.1]-[5.2]. Pipe 2 had antifriction layers at the inner surfaces of both armouring layers. The measured friction moment was 2.1 kNm at 200 bar pressure, giving a friction coefficient during sliding of 0.1 between the steel layers and the antifriction layers. Pipe 1 had antifriction layer at the inner surface of the inner armouring layer only and lubrication had been applied between the steel layers. According to oral communication with the producer, this lubrication was used for manufacturing purposes and not to reduce wear. The friction moment was measured to 1.0 kNm at 250 bar internal pressure, giving a friction coefficient of 0.05 between the lubricated steel layers during sliding, assuming a friction coefficient of 0.1 between the inner layer and the antifriction sheath in accordance with the result for Pipe 2.

The producers were notified that the pipes would be tested by combined axial and bending load cycles. Hence the pipes were fitted with a bending stiffener at one end. The geometry and bending stiffness distribution of the stiffeners are shown in Figures 6.2 and 6.3, for Pipe 1 and Pipe 2 respectively. The stiffener was attached to the end termination, and the pipe was allowed to slide in the stiffener. The total bending stiffness of a cross section covered by the stiffener was hence the sum of the individual stiffnesses of the pipe and stiffener.

The end termination represents a stress concentration both with regard to global pipe moment and local tendon stresses. The global stress concentration is due to an increased curvature of the pipe towards the end. The local stress concentration is due to the termination of each tendon by means of an epoxy casting inside the inner cylinder surface of the end fitting, see Figures 6.4 and 6.5. In order to ensure that each tendon is surrounded by epoxy, the armouring wires are bent outward into a fan configuration. This introduces a possible stress

 ISBN 82-7119-427-5 ISSN 0802-3271

concentration at the bend. The purpose of the steel ring shown in Figures 6.4 and 6.5 is to lock the armouring wires and hence reduce the stress concentration.

The purpose of the bending stiffener is to reduce the global stress concentration. At the Pipe 1 bending stiffener/end fitting and at the bending stiffener/pipe transition, there is a jump in bending stiffness of the order 1:10 and 1:2.2 respectively, at 250 bar internal pressure. Due to these discontinuities, global stress concentrations are introduced. At the pipe-nipple transition, the cross sectional behaviour leads to an additional local stress concentration, as no slip take place between the cross sections as described above. The corresponding transition values for Pipe 2 are 1:250 and 1:1.06. Thus there will be an increased global stress concentration at the bending stiffener/end fitting transition for Pipe 2.

The purpose of the bending stiffener is to provide a stiffness transition sufficiently smooth to reduce bending stresses and to move the bending stress maximum out of the pipe/nipple region. If this proves to be successful, the fatigue strength of the pipe would be governed by the fatigue properties of straight pipe sections with no local stress concentrations. This would lead to a considerable increase in the fatigue life, and to a simplified fatigue design analysis as the local stress concentration becomes small and possibly negligible.

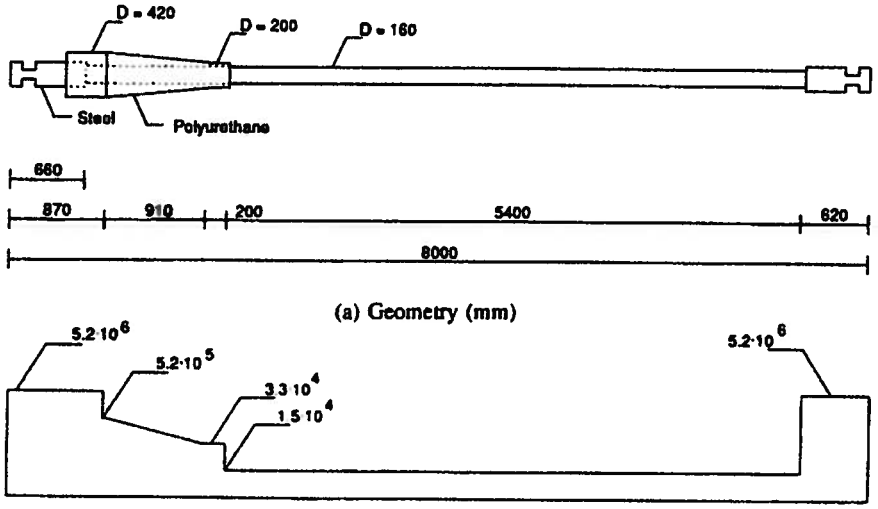

Figure 6.2 Pipe 1 geometry and bending stiffness distribution

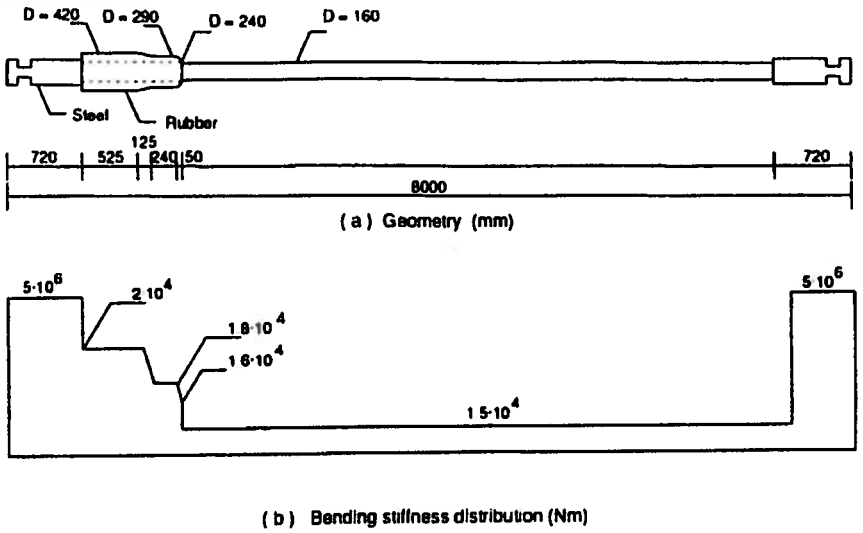

Figure 6.3 Pipe 2 geometry and bending stiffness distribution

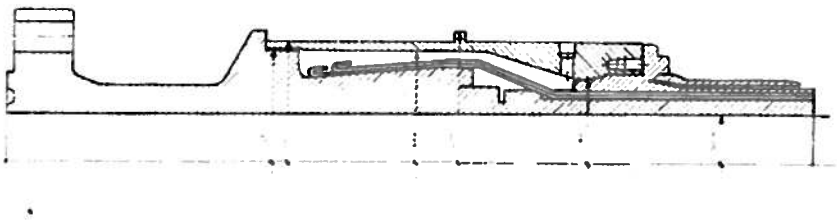

Figure 6.4 End fitting geometry for Pipe 1

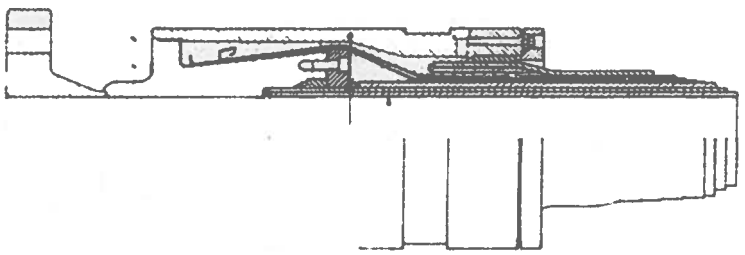

Figure 6.5 End fitting geometry for Pipe 2

 ISBN 82-7119-427-5 ISSN 0802-3271

Table 6.1 Description of test specimens

Parameter	Pipe 1	Pipe 2
Weight in air, waterf. (kgm^{-1})	59.6	52.0
Weight in air, empty (kgm^{-1})	51.3	43.7
Axial stiffness (N)	$2.14\ 10^8$ 1)	$1.74\ 10^8$ 1)
Sliding bending stiffn. (kNm^2) (No loading)	7.6 1)	8.5 1)
Sliding bending stiffn. (kNm^2)	15.0 1) (250 bar pressure)	15.0 1) (200 bar pressure)
Friction moment (7 bar pres.)(kNm)	0.35	0.86
Friction moment (kNm)	1.0 (250 bar pressure)	2.1 (200 bar pressure)
Tendon cross section a/b (mm)	6.0/3.0	6.0/3.0
Number of tendons Outer/Inner	60/57	53/50
Armouring radius Outer/Inner (mm)	73/70	74/69
Critical curvature radius (m)	1.0	0.40
Lay angle Outer/Inner (deg)	+35/-35	-35/+35

1) Values obtained by CAFLEX

 ISBN 82-7119-427-5 ISSN 0802-3271

6.4 Investigation of stress effects at bending gradients

6.4.1 Description of test program

The main purpose of the test was to investigate the effect of end restraints on tendon stresses. Numerical simulations as those described in Chapter 4 had demonstrated that high stresses may occur at the pipe neutral axis due to local transverse curvature of the tendon and a non-linear coupling with axial forces. These simulations also showed that axial stresses may increase dramatically due to the fact that the elongation at one location can not be compensated by similar compression in a neighbouring section both due to the position of the tendon at the end restraint and curvature gradient effects. It was therefore of interest to measure both these effects and accordingly, the following three sets of tests were carried out:

Test 1: 0^o end angle, 250 bar internal pressure and axial tension ranging from 10 to 400 kN in steps of 50 kN.

Test 2: 8^o end angle, 250 bar internal pressure and axial tension ranging from 10 to 400 kN in steps of 50 kN.

Test 3: 13^o end angle, 250 bar internal pressure and axial tension ranging from 10 to 400 kN in steps of 50 kN.

In the first test, stresses due to axisymmetric load conditions were measured in order to ensure that the strain gauges worked correctly. Tests two and three were carried out to investigate the effect of having increased bending gradients. In order to ease installation of strain gauges, these were mounted at the bare pipe end. This end of the pipe was given a fixed rotation to induce the wanted curvature variations.

A load case described by 0^o end angle, 7 bar internal pressure and 10 kN tension was used as a reference state for all tests.

 ISBN 82-7119-427-5 ISSN 0802-3271

The testing temperature was 20 °C approximately.

6.4.2 Instrumentation

Local bending stresses caused by moments about the surface normal were measured by two pairs of strain gauges mounted 5 and 30 mm from the end fitting along one of the outer layer tendons. The position of these two strain gauge pairs corresponded approximately to the neutral axis of bending, as shown in Figure 6.6.

In order to measure the axial stress distribution, four series of three strain gauges were mounted on the same tendon at four stations positioned at an average distance along the pipe longitudinal axis of 46 mm, 318 mm, 626 mm and 935 mm from the end fitting. These strain gauges were also mounted at the neutral axis of bending in order to avoid interaction between the axial stresses and normal curvature induced bending stresses (Confer Eq.(2.32) and Eq.(2.66)). The reason why three strain gauges were used at each station was to eliminate the effect of local bending stresses induced by irregular support of the outer layer from the inner layer, thus assuming that the average value would represent the axial stress component with sufficient accuracy.

In order to measure the global curvature distribution, two extensometers were mounted at the compressive and tensile sides of the pipe at a distance of 160 mm from the end fitting. In addition, one extensometer was mounted 480 mm from the end fitting on the compressive side.

 ISBN 82-7119-427-5 ISSN 0802-3271

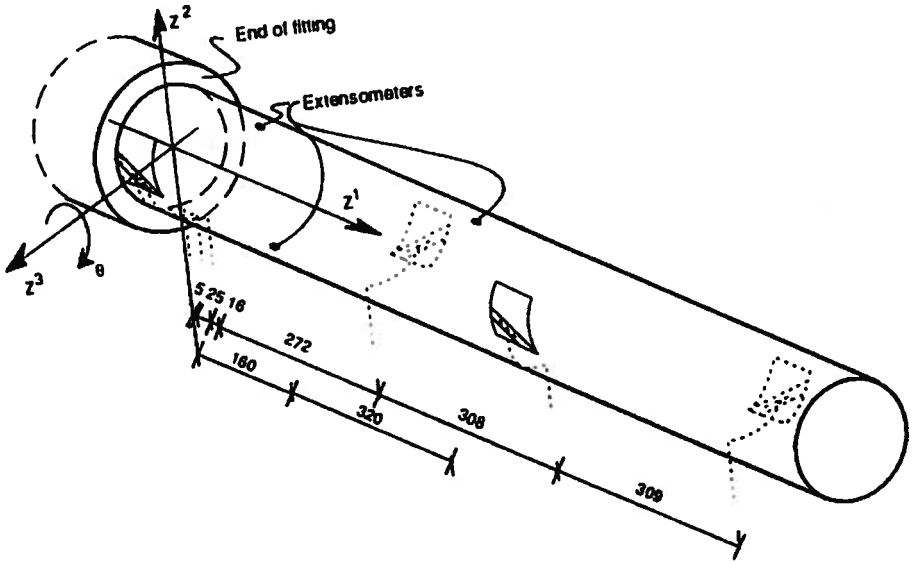

Figure 6.6 Position of strain gauges

6.4.3 Method of analysis

Four different computer programs were used to calculate the tendon stresses.

CAFLEX [1.6] was used to find the tendon axial stresses due to internal pressure and tension. This program was also used to determine the stiffness parameters in radial direction.'

The AFLEX program based on the present theory was used to find the stresses in the tendon due to bending. AFLEX applies a finite element model for one armouring tendon subjected to an arbitrary load history defined by axial forces and corresponding global curvature distributions. In Sub-section 4.7.2 it was demonstrated that due to friction the order of load application will influence the resulting stresses. Thus, in order to simulate the stress history throughout loading and unloading, the true combination of tension and curvature distribution was needed. The load history applied in the AFLEX model therefore consisted of a series of tensions and curvature distributions.

In order to obtain the curvature distributions at each tension level, the computer program PAS [6.1] was used. PAS is a computer program for two-dimensional nonlinear static analysis of

pipes. The curvature was, however, also measured at two stations as described in Sub-section 6.4.2 in order to verify the theoretical values.

The end restraint parameters needed in the AFLEX model had to be found by a local analysis considering the interaction between the tendon and the epoxy. The computer program SESAM [6.2] was used for this purpose.

6.4.4 Description of numerical models

The finite element model used to find the curvature distribution (the PAS program) is shown in Figure 6.7. The specimen was modelled as a beam with different boundary conditions at the two ends. At the left end, the beam was fixed against both vertical and horizontal translations, whereas the rotation was prescribed according to the respective load cases defined in Sub-section 6.4.1. At the other end, only vertical translation was fixed. In the horizontal direction a tensile load T was applied according to Sub-section 6.4.1. The element length used varied from 39.6 mm to 290 mm. This was obtained by using 64 beam elements.

The stiffness distribution of the bending stiffener section was taken from Figure 6.2 (see also Figure 6.7), taking into account that the bending stiffener was positioned at the right end during these tests. The curvature at the instrumented pipe section was therefore controlled by the pipe bending stiffness only, and could exceed the critical value with subsequent increase of the bending stiffness. The bending stiffness implemented into the finite element model was therefore based on a trilinear relationship between the moment and the curvature as shown in Figure 6.8, having an initial stiffness according to the measured friction moment and corresponding curvature [5.1], a sliding bending stiffness according to Table 6.1 and a significantly higher value for curvatures exceeding the critical value.

The corresponding AFLEX finite element model is shown in Figure 6.9. The model starts 100 mm inside the end fitting, at the end of the steel ring (confer Figure 6.4). Here, each tendon is bent to provide sufficient room for epoxy infill. The element length from this point to 1150 mm outside the end fitting was 15.3 mm, whereas the element length was increased to 39.6

mm for the remaining section. 100 and 175 elements were used for the two sections respectively.

Since the loads were introduced stepwise at 50 kN intervals, no lubrication effect would be present between the steel layers, and the friction coefficient would be static. The friction coefficient was assumed to be 0.3 according to Sub-section 3.3.2 and the friction spring characteristic was tuned to obtain this value after 0.1 mm sliding, corresponding to the transition between the gross-slip and reciprocating sliding regimes defined in Sub-section 3.2.2. The Coulomb friction model was used as the test-rig set-up allows one way loading only.

The load history was selected to investigate the equilibrium states from the reference state throughout one cycle of tension loading and unloading. The curvature distributions applied were corresponding to the initial reference configuration and to subsequent configurations at 10 kN, 50 kN, 100 kN, 200 kN, 300 kN and 400 kN tension. Since the pressure was released prior to application of the end angle, the friction springs were applied at the first load level after having applied 10 kN tension and the respective end angles.

The radial stiffness of the supporting pipe was calculated by CAFLEX and found to be $8.51 \cdot 10^8$ Nm^{-2} and $1.87 \cdot 10^9$ Nm^{-2} inwards for the outer and inner armouring layers respectively and $7.0 \cdot 10^6$ Nm^{-2} outwards for both layers.

At both ends, the surface normal and transverse translations as well as the rotation about the surface normal were fixed. In the longitudinal direction, a spring was introduced at both ends. The stiffness of this spring depends on the stiffness of the epoxy infill as well as the geometry of the cavity, and had to be found from separate analyses by using SESAM [6.2].

The SESAM finite element model is shown in Figure 6.10. The geometry of the model was taken from Figure 6.4. The tendon was modelled by beam elements with 3 nodes in the longitudinal direction (linear axial strain), whereas the epoxy was modelled by means of linear strain triangular elements under plane strain conditions of the twisted sector following the

 ISBN 82-7119-427-5 ISSN 0802-3271

helix. Altogether 46 beam elements and 524 triangular elements were used in the model. The modulus of elasticity of the epoxy was taken to be 2.8 GPa, confer [6.3].

Along the segments a_1, a_2, a_3, a_4, a_8, a_9, and a_{10}, the epoxy is rigidly connected to the steel surface. Thus all translational degrees of freedom were fixed along these segments. Along segment a_6 there is a steel ring that restrains the tendon from vertical upward movement. Thus the vertical translational degree of freedom was fixed along this segment. The segments a_5 and a_7 are, however, made by the pipe structure itself and were therefore left free to move both horizontally and vertically. The right end lower corner node represents the end of the tendon. At this end, an axial tensile load of 1000 N was applied.

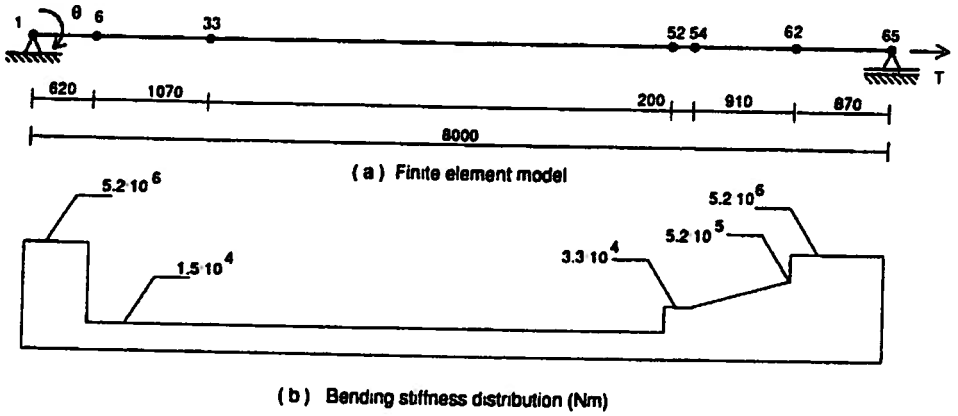

Figure 6.7 PAS finite element model for end restraint effect simulation

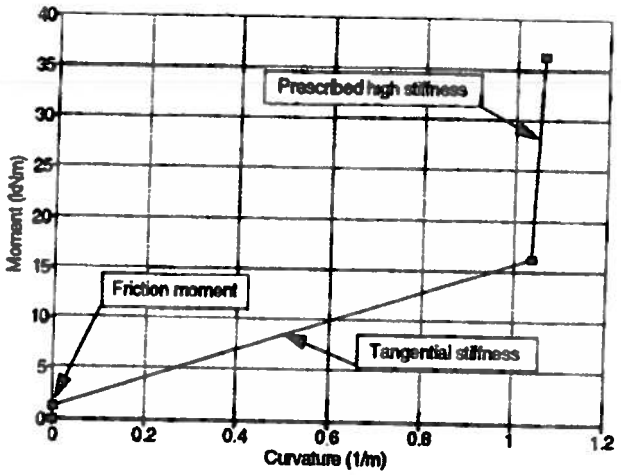

Figure 6.8 Diagram of moment/curvature relationship implemented into PAS

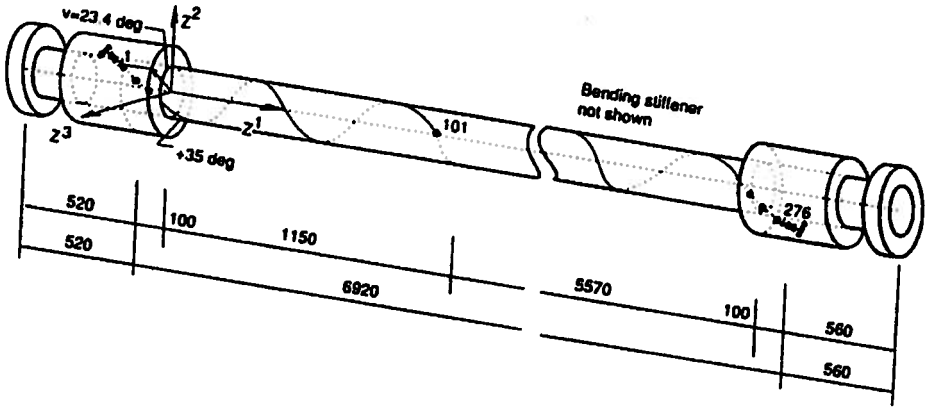

Figure 6.9 AFLEX finite element model for end restraint effect simulation

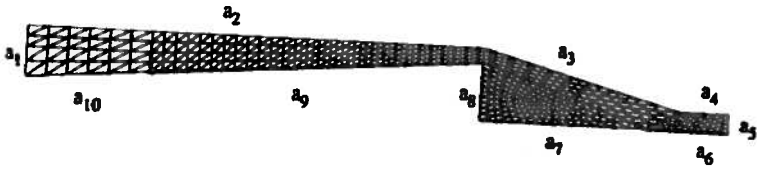

Figure 6.10 SESAM finite element model for Pipe 1 end fitting

6.4.5 Results from initial analyses

The result from the SESAM analysis showed that the displacement at 1000 N tension was 0.0453 mm which gave a longitudinal spring stiffness in the AFLEX model of 2.2 10^7 Nm^{-1}

Figures 6.11 and 6.12 show the different curvature distributions obtained by PAS for alternative tension levels for the 8^o and 13^o end angles respectively. It is seen that as the tension increase, the curvature build up to high values at the end fitting. This is a consequence

of the low bending stiffness of the pipe at the fixed end. It is also seen that the change of curvature tends to be reduced for increasing tension. This will limit hysteresis effects on the stresses, since the major part of the curvature change take place at relative low tension and contact pressure values.

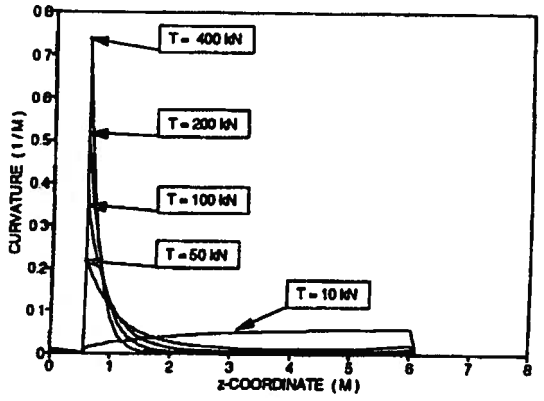

Figure 6.11 Curvature distribution for alternative tension levels, 8° end angle

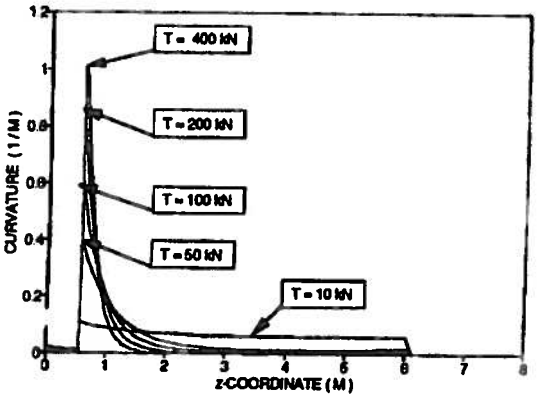

Figure 6.12 Curvature distribution for alternative tension values, 13° end angle

6.4.6 Measured and calculated axisymmetric stresses

Figure 6.13 shows the axisymmetric stresses obtained by CAFLEX together with the observed values. The measured values were obtained by averaging all strain gauge values. It is seen that the measured stress due to 250 bar internal pressure is 35 MPa less than the calculated value, whereas very good correlation between the measured and calculated values is obtained due to the increase in applied tension. It is difficult to explain the initial deviation, as the end-cap induced tension due to the internal pressure should ensure almost equal load sharing between the two armouring layers. One possibility is that the end restraint properties are slightly different for the two layers. If so, the result will be that one layer will carry more load than the other close to the end fitting. The coefficient of variation for these measurements was found to be 0.20-0.25 for all load steps, which indicates that local bending stress effects induced by the irregular inner layer is proportional to the axial stress and should be considered in the stress analysis of the outer layer. This is, however, counteracted by the fact that the inner layer normally will have the highest stresses due to large contact loads. Since the inner

layer normally rests on thermoplastics, such effects are expected to be less important for the inner layer.

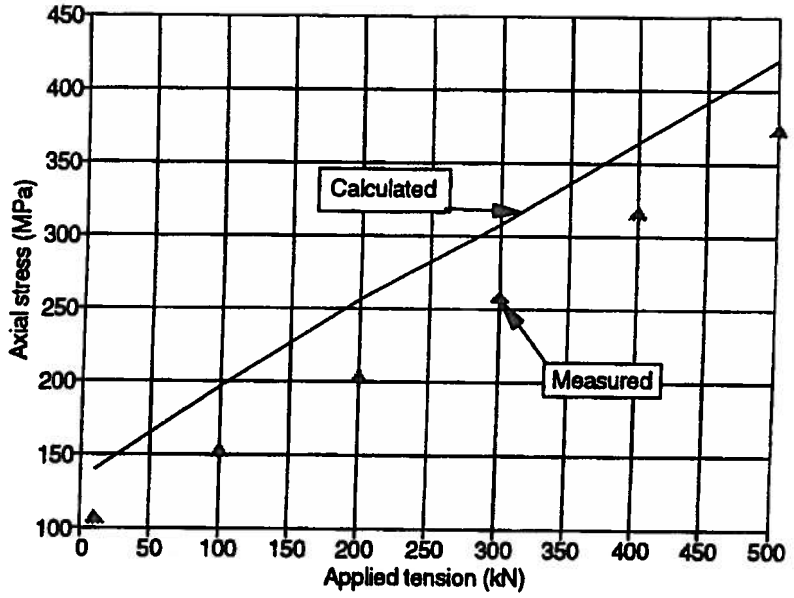

Figure 6.13 Measured and calculated axisymmetric stresses

6.4.7 Measured and calculated bending induced stresses

Figures 6.14 and 6.15 show the measured and the calculated curvature at the extensometers for 8^o and 13^o end angles respectively. In these figures curves are used for the measured values whereas the calculated values are indicated by markers. It is seen that for Station 1 which is closest to the end fitting, there is an initial deviation which tends to be eliminated as the tension is increased. This may be due to deviation between the actual bending stiffness and friction moment, and the values used in the calculations for the initial configuration and at low tensions. For station 2 it is seen that the calculated curvatures decrease for tension values above 50 kN whereas the measured values stay almost constant above this value. The measured constant curvature is due to exceedance of the maximum tolerance limit for the extensometer at station 2. The actual curvatures in station 2 could therefore have been slightly above this value. This indicates that the calculated curvature gradient is steeper than the actual gradient. The actual bending stiffness may therefore have been slightly above the values used

in the simulations. The measured bending stiffness values reported in [5.1] indicate higher bending stiffness than used in the calculations. However by using these values, the calculated values were significantly above the measured values. Having in mind that the curvature gradient is very steep, the calculated curvature distribution is therefore believed to be in reasonable agreement with the measured behaviour.

It is also seen that there is a significant hysteresis in the measured curvature behaviour. The curvature seems to be constant until 150 kN - 200 kN of the tension load is released.

In the subsequent figures the calculated values are shown by curves, whereas the measured values are shown by markers.

Figures 6.16 and 6.17 show the calculated axial stress distribution together with the measured values for 100 kN and 400 kN tension levels and for 8^o and 13^o end angles respectively. It is seen that for the 8^o end angle there is good correlation between the measured and calculated stresses at 400 kN tension, whereas the measured values are significantly below the calculated values at 100 kN. This can be explained by looking at Figure 6.14. The measured curvature is less than the calculated and the deviation is seen to be constant for all tensions above 100 kN. The relative contribution from this deviation will, however, be larger at 100 kN than 400 kN. For 13^o end angle there is good correlation for both 100 kN and 400 kN tensions at the two closest strain gauge stations and this is in agreement with the good correlation found between measured and calculated curvatures (See Figure 6.15) for these tension levels. It is seen that the measured values at the two next strain gauge stations are significantly below the calculated values. However, the lesson learnt during these simulations was that the resulting stress distribution is very sensitive to small changes in the curvature distribution. Considering these factors, the measurements confirm that axial stresses will build up at bending gradients, in a similar way as calculated by the theoretical model.

Figures 6.18 and 6.19 show the corresponding theoretical and measured bending stresses at the two strain gauges that were used for this purpose. It is seen that there is a good correlation specially at high tension levels. The deviation at low tension levels is similar to the behaviour

found for the curvatures and may be due to deviation between the bending stiffness used and the actual value.

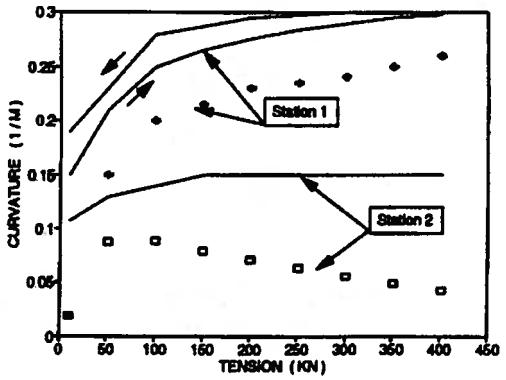

Figure 6.14 Measured (solid line) and calculated (dots) curvature as a function of tension for 8° end angle

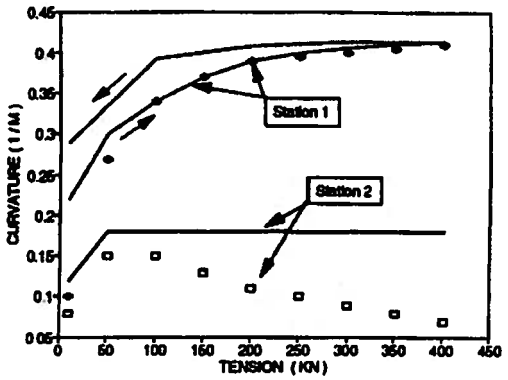

Figure 6.15 Measured (solid line) and calculated (dots) curvatures for 13° end angle

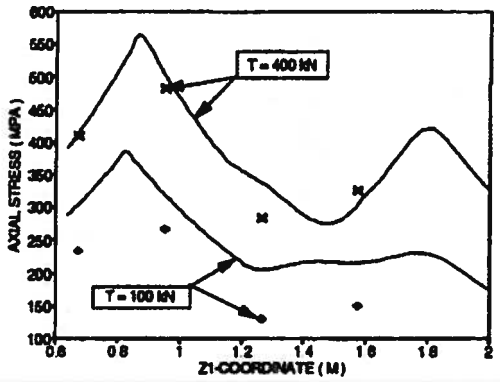

Figure 6.16 Measured (dots) and calculated (solid line) axial stresses for 8° end angle

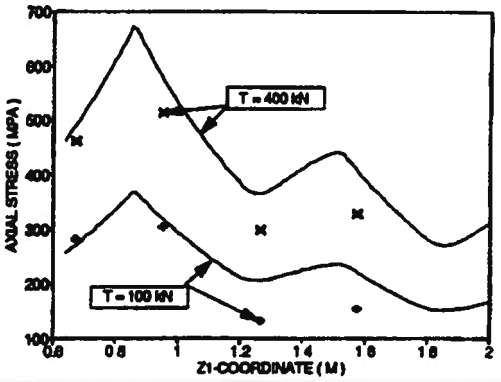

Figure 6.17 Measured (dots) and calculated (solid line) axial stresses for 13° end angle

 ISBN 82-7119-427-5 ISSN 0802-3271

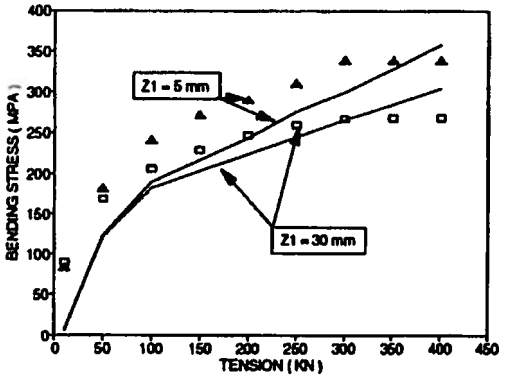

Figure 6.18 Measured (dots) and calculated (solid line) bending stresses for 8° end angle

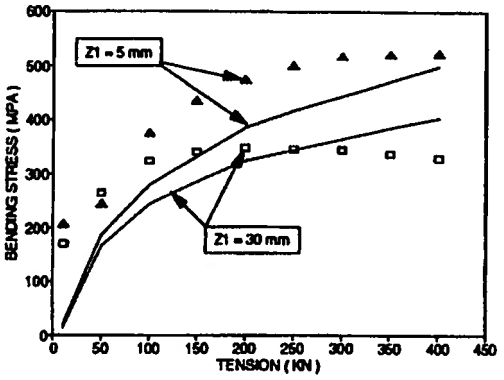

Figure 6.19 Measured (dots) and calculated (solid line) bending stresses for 13° end angle

Figures 6.20 shows the calculated and measured axial stress history at the first strain gauge station for 13° end angle. It is seen that the measured hysteresis is less for high tension values. This is believed to be due to the curvature hysteresis shown in Figure 6.15. As the curvature stay constant during the first phase of unloading there will be limited sliding and hysteresis.

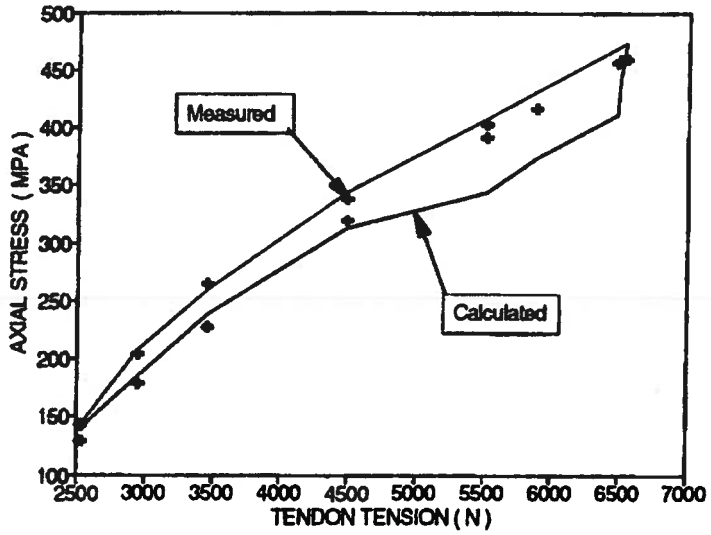

Figure 6.20 Measured (dots) and calculated (solid line) axial stress history at strain gauge station 1 for 13° end angle

 ISBN 82-7119-427-5 ISSN 0802-3271

6.5 Pipe 2 fatigue testing

6.5.1 Fatigue test program

The fatigue test of Pipe 2 consisted of two load sequences as described in Table 6.2

Table 6.2 Test conditions for Pipe 2

Sequence no.	Int. pressure (MPa)	Tension range (kN)	End angle (deg.)	Number of cycles
1	20.0	0.2 - 130.0	10.0	10^6
2	20.0	0.2 - 260.0	5.0	$5 \cdot 10^5$

6.5.2 Description of test results

The test was terminated after $5 \cdot 10^5$ cycles of Load sequence 2, due to observed twist deformation of the pipe structure. Inspection of the pipe showed that these deformations were due to fracture of both armouring layers [6.4]. The fractures in both layers occured due to metal fatigue at the tendon bends inside the end fitting. In the inner layer, 20 out of 50 tendons failed whereas 44 out of 53 tendons failed in the outer layer. Among these failures, 18 and 43 failures occured within the shaded areas shown in Figure 6.21 for the inner and outer layers respectively.

The following discussion will concentrate on investigating a possible correlation between the observed failures and the stress ranges found by theoretical calculations.

 ISBN 82-7119-427-5 ISSN 0802-3271

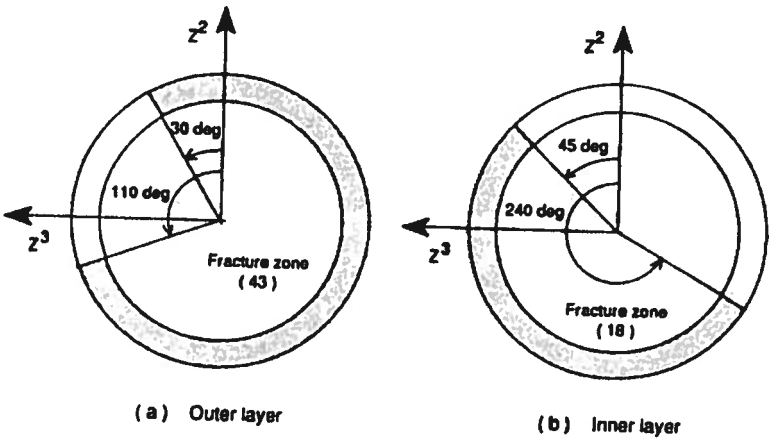

Figure 6.21 Fracture regions inside end-fitting of Pipe 2

6.5.3 Method of analysis

CAFLEX, AFLEX, PAS and SESAM were used in a similar way as described in Sub-section 6.4.3 in order to predict the stress ranges inside the end fitting. However, since the fatigue failures occured at the tendon bend inside the end fitting, the SESAM analysis was also applied to investigate the local bending stresses at this point.

The stress ranges were found as stress differences between two load conditions. Due to friction and nonlinear curvature/tension interaction, it was not obvious that the maximum stress ranges were identified by considering the minimum and the maximum tension levels. It was therefore necessary to examine the stress history throughout loading and unloading. Since all failures occured at the same cross section, only the stress history of the first element was needed.

The maximum longitudinal stress range $\Delta\sigma_{11}$ found during one load cycle was taken as the sum of the axial and local bending stresses at the actual cross section as follows:

$$\Delta\sigma_{11}=\Delta\sigma_{a}+\Delta\sigma_{b3} \qquad (6.1)$$

 ISBN 82-7119-427-5 ISSN 0802-3271

where $\Delta\sigma_a$ is the axial stress range and $\Delta\sigma_{b3}$ is the local bending stress range caused by bending about the X^3-axis.

The AFLEX program can perform stress analysis for one tendon in each run. In order to find the stress ranges around the circumference of the cross section, 8 different tendons were investigated, each found at 45 degrees intervals around the pipe circumference.

6.5.4 Description of numerical models

The finite element model used in the PAS program to find the curvature distribution is shown in Figure 6.22. The pipe was modelled in a similar way as described in Sub-section 6.4.4. The average element length within the bending stiffener region was 39.2 mm and was increased to an average value of 176.5 mm outside this region.

The corresponding AFLEX finite element model is shown in Figure 6.23. The model starts 85 mm inside the end fitting, close to the end of the steel ring (Confer Figure 6.5), where each tendon is bent in order to provide sufficient room for epoxy infill. The element length from this point to a section 1015 mm outside the end fitting was 13.4 mm while the element length was increased to 38.6 mm for the remaining section. This was obtained by using 100 and 175 elements for the two sections respectively. The friction coefficient between the armouring layers and the respective antifriction layers was found by CAFLEX to be 0.10. The Coulomb friction model was used. The characteristic of the friction springs in the Coulomb model was based on applying the full magnitude of the friction force after 0.1 mm displacement as described in Sub-section 6.4.4.

The load procedure was further based on investigating the subsequent equilibrium states from the reference state defined by the respective end angles and 0.2 kN tension and throughout one cycle of tension loading and unloading. The curvature distributions applied were corresponding to tension levels of 0.2 kN, 10 kN, 50 kN and 130 kN for Load sequence 1. The corresponding curvature distributions for Load sequence 2 were taken at 0.2 kN, 10 kN, 50 kN and 260 kN tension.

 ISBN 82-7119-427-5 ISSN 0802-3271

The stiffness along the surface normal was found by CAFLEX analyses to be $5.1 \cdot 10^8$ Nm^{-2} and $1.23 \cdot 10^9$ Nm^{-2} inwards for the outer and inner armouring layers respectively and $9.2 \cdot 10^6$ Nm^{-2} outwards for both layers. At both ends, the surface normal and transverse translations as well as the rotation about the surface normal were fixed. In the longitudinal direction, a longitudinal spring was introduced at both ends. The property of this spring depends on the stiffness of the epoxy infill as well as the geometry of the cavity, and had to be found from separate analyses by using SESAM.

The SESAM finite element model is shown in Figure 6.24, where the geometrical quantities were taken from Figure 6.5. The tendon and surrounding epoxy was modelled in a similar way as described in Sub-section 6.4.4.

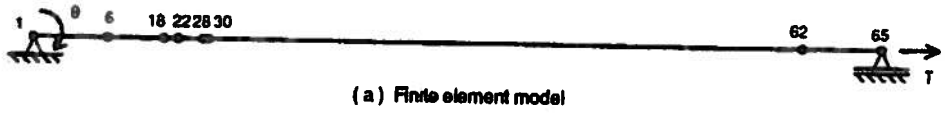

Figure 6.22 PAS finite element model for Pipe 2

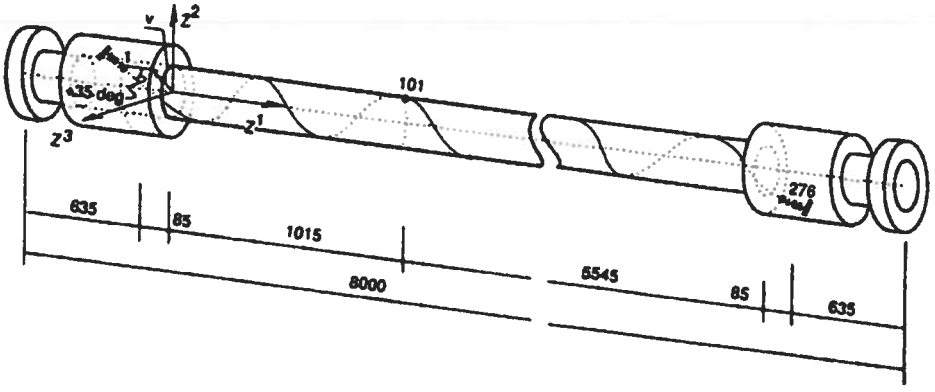

Figure 6.23 AFLEX finite element model for Pipe 2

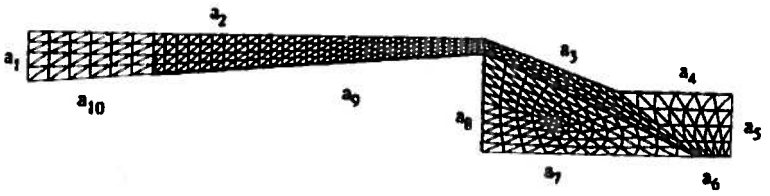

Figure 6.24 SESAM finite element model for Pipe 2

6.5.5 Results from initial analyses

The result from the SESAM analysis showed as expected a stress maximum at the tendon bend at the transition between segments a_6 and a_7 in Figure 6.24. The bending stress was tensile at the outer surface and compressive at the inner surface of the tendon. For each MPa in axial stress, there was 0.30 MPa bending stress when assuming a sharp bend of the tendon according to Figure 6.5. Inspection of the tendons in the end fitting, confirmed the sharp directional change.

The displacement at 1 kN tension was 0.0559 mm, which gave a longitudinal spring stiffness to be used in the AFLEX model of $1.79 \cdot 10^7$ Nm^{-1}

Figures 6.25 and 6.26 show the curvature distributions obtained by PAS at alternative tension levels for Load sequence 1 and Load sequence 2 respectively. It is seen that as the tension increases, the curvature build up to higher values at the end fitting. This is caused by the fact that the bending stiffener is far too soft to provide a gradually increase of stiffness between the pipe and the fixed end fitting. The largest curvature occur in Load sequence 1. This is due to the 10^0 end angle, which is reduced to 5^0 for Load sequence 2.

Table 6.3 gives the tendon axial stresses for the armouring layers as well as the contact pressure occuring between the armouring layers as obtained by CAFLEX for three alternative tension levels covering both load sequences and at 200 bar internal pressure.

 ISBN 82-7119-427-5 ISSN 0802-3271

Table 6.3 Axial stresses due to axisymmetric loading of Pipe 2

Quantity	T=0.2kN	T=130 kN	T=260 kN
Axial stress σ_a Outer layer (MPa)	160	244	328
Axial stress σ_a Inner layer (MPa)	160	258	356
Contact pressure σ_{22} (MPa)	1.9	3.4	4.6

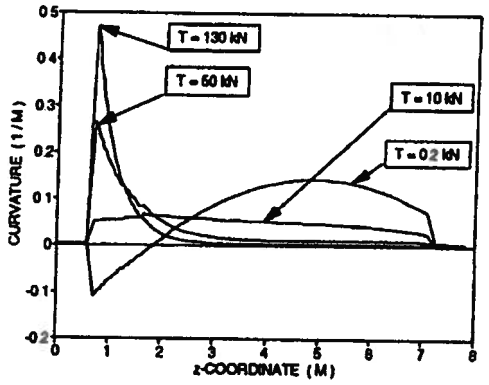

Figure 6.25 Curvature distributions at alternative tension levels for Pipe 2, Load sequence 1 of fatigue testing

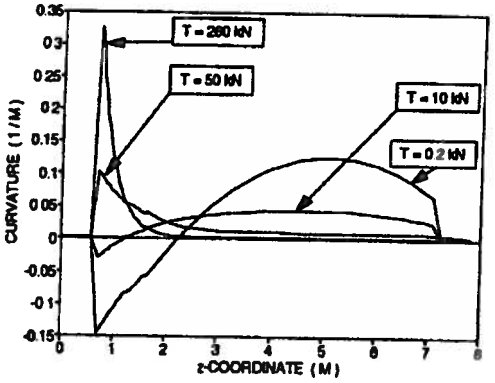

Figure 6.26 Curvature distributions at alternative tension levels for Pipe 2, Load sequence 2 of fatigue testing

6.5.6 Results and discussion of the AFLEX analyses

Figure 6.27 shows the theoretical normalized stress ranges for both layers and load sequences. The stresses were normalized with respect to the theoretical fatigue limit obtained by linear interpolation in the Haig diagram (Confer Sub-section 1.2.2). The fatigue limit was assumed to be 482 MPa at zero mean stress. This value was based on fatigue tests of individual

tendons as reported by Eknes and Berge [6.4]. The fracture zones are indicated by the shaded areas. It is seen that for Load sequence 1, the stresses were within the fatigue limit except for two points being slightly above the fatigue limit. For Load sequence 2, however, the stress ranges were far beyond the fatigue limit, having maximum values approximately in the middle of the observed fracture zones. For the non-fracture zone, the stresses were found to be below the fatigue limit. The calculated distribution of stress ranges was therefore in fairly good agreement with the observations. The high variation of the stress around the circumference indicates that curvature effects give significant contributions to the total stress range

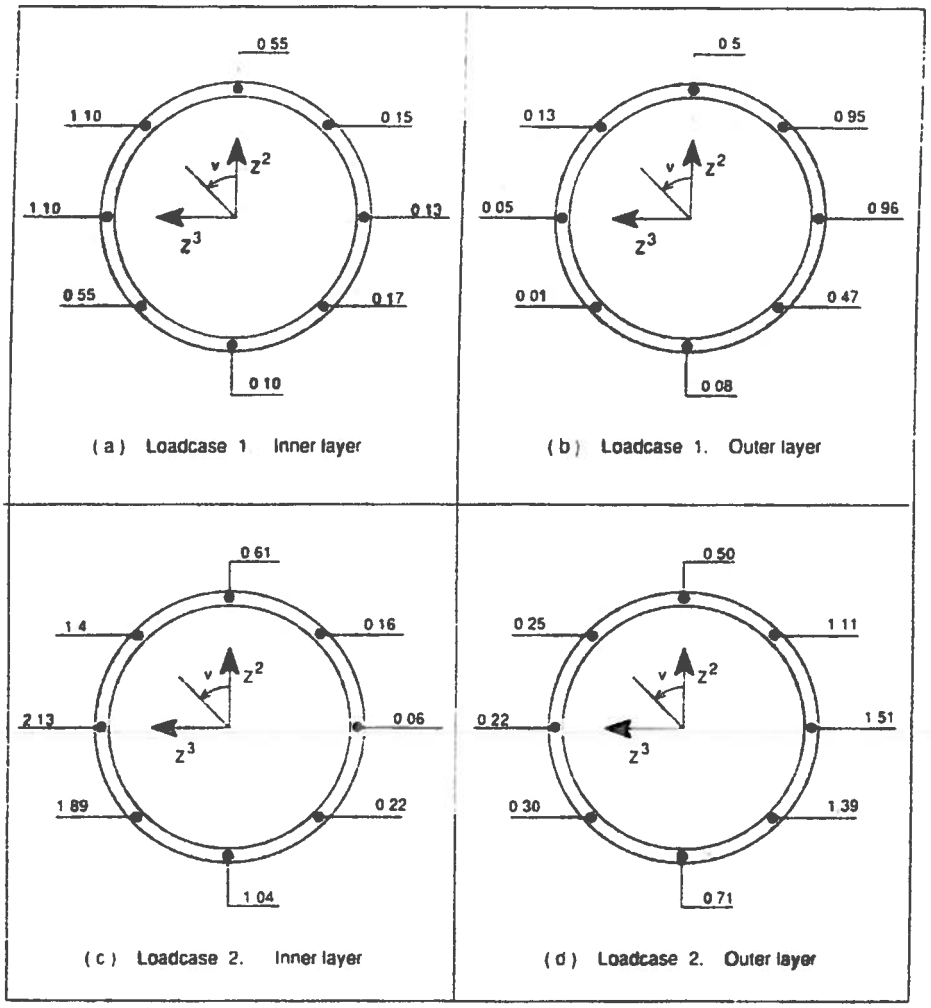

Figure 6.27 Normalized stress distribution at the fracture cross-section of Pipe 2

 ISBN 82-7119-427-5 ISSN 0802-3271

6.6 Pipe 1 fatigue testing

6.6.1 Fatigue test program

The fatigue test of Pipe 1 consisted of two load sequences as described in Table 6.4

Table 6.4 Test conditions for Pipe 1 during fatigue testing

Sequence no.	Int. pressure (MPa)	Tension range (kN)	End angle (deg.)	Number of cycles
1	25.0	0.2 - 200.0	10.0	10^6
2	25.0	0.2 - 500.0	5.0	$1.3 \cdot 10^6$

6.6.2 Description of test results

The test was terminated after $1.3 \cdot 10^6$ cycles during Load sequence 2 due to severe twist deformation in the pipe. Inspection of the different layers of the pipe structure showed that the fatigue failure included several fractures in both armouring layers [6.5]. The results from an inspection of each individual fracture can be summarized as follows:

The initial failure had taken place in the inner tensile armouring layer. The failures of individual wires was caused by fretting fatigue as evidenced by the character of the fracture surfaces and the presence of oxide debris.

Almost all failures of individual armouring tendons were within a distance of 2 m from the end of the bending stiffener.

 ISBN 82-7119-427-5 ISSN 0802-3271

Practically all failures of the inner layer occured along the top of the pipe on the compressive side relative to the global bending moment (20 fractures) or within a region 90^0 from the top (17 fractures) (see Figure 6.29).

Failures in the outer layer had taken place inside the epoxy casting of the termination, concentrated on the tensile side of the pipe relative to the global bending moment (20 fractures). These fracture surfaces had significantly smaller fatigue areas than found for the inner layer fractures, which indicates that these failures were secondary, caused by load redistribution following the failures of the inner layer.

The distribution of failures for the outer layer is indicated by the shaded area in Figure 6.28. 20 out of 60 tendons failed and all fractures were within the shaded area.

The distribution of failures in the inner layer for the first 3 m of Pipe 1 is shown in Fig 6.29. In this Figure the pipe has been rotated 90 degrees towards the reader, so that the compressive side of the pipe is positioned at Z^3=0, closest to the reader.

As fretting induced fatigue was the primary source of failure, and due to the fact that this phenomenon depend primarily on contact stresses and relative displacements (confer Sub-section 3.2.2), it is of interest to find a possible correlation between the observed failures, and the actual contact forces and displacements found from theoretical analyses, confer Sub-section 6.6.5.

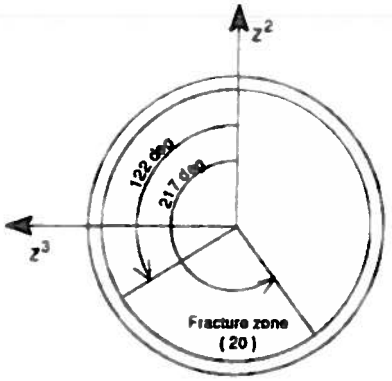

Figure 6.28 Fatigue failure zone for outer layer of Pipe 1

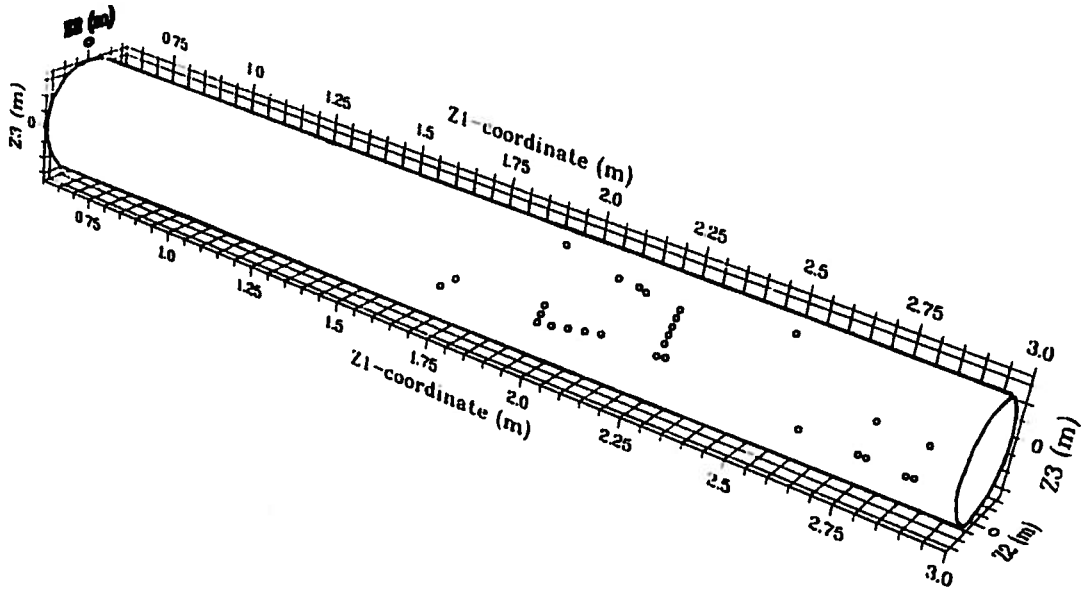

Figure 6.29 Distribution of fretting failures at the inner layer of Pipe 1

6.6.3 Method of analysis

In order to predict the stress and relative displacements of the armouring layers the same procedure as described in Sub-section 6.5.3 was used.

However, since the position of the fretting fatigue failures were distributed at different positions along the pipe longitudinal axis the procedure described in Sub-section 4.8.2 had to be used in addition. The stress and relative displacement ranges were calculated based on Eqs.(4.4)-(4.6).

6.6.4 Description of numerical models

The finite element model used in the PAS computer program in order to find the curvature distribution is shown in Figure 6.30. The tensile load T was applied according to Section 6.6.1 for the two load sequences. The element length was in average 46.3 mm along the bending

stiffener, and was increased to an average of 68.9 mm outside this region. In total 124 elements were used.

The AFLEX finite element model of the tendon, is shown in Figure 6.31. The model included 100 mm inside the end fitting and was started at the end of the steel ring (See Figure 6.4). The element length from this point to 1075 mm outside the bending stiffener, where the most severe curvature changes were expected, was 20.3 mm whereas the element length was increased to 43.2 mm for the remaining section. 150 and 125 elements were used for the two sections respectively. The friction coefficients used were 0.05 between the armouring layers and 0.1 between the inner layer and the supporting sheath according to Section 6.3. The Coulomb friction model was applied. The spring stiffness was tuned to give the maximum friction force for 0.1 mm displacement corresponding to the transition between the gross-slip and reciprocating sliding regimes according to Sub-section 3.2.2.

The load sequence was found from investigation of equilibrium states from the reference state defined by the respective end angles and 0.2 kN tension and throughout one tension cycle. The curvature distributions applied were corresponding to tension levels of 0.2 kN, 10 kN, 50 kN and 200 kN for Load sequence 1. The corresponding curvature distributions for Load sequence 2 were taken at 0.2 kN, 10 kN, 50 kN and 500 kN applied tension.

At both ends, the surface normal and transverse translations as well as the rotation about the surface normal were fixed. In the longitudinal direction, longitudinal springs were introduced at both ends according to Sub-section 6.4.4.

The application of the SESAM finite element model was described in Sub-section 6.4.4.

Figure 6.30 PAS finite element model for fatigue analysis of Pipe 1

 ISBN 82-7119-427-5 ISSN 0802-3271

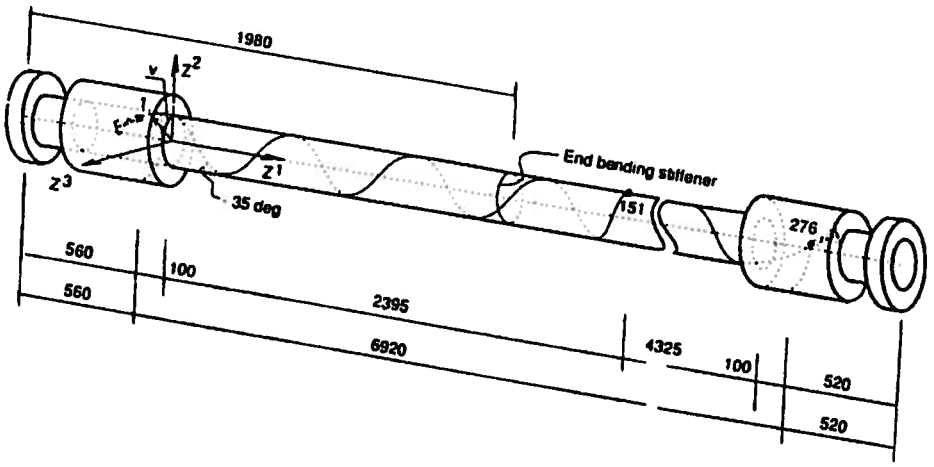

Figure 6.31 AFLEX finite element model for fatigue analysis of Pipe 1

6.6.5 Contact geometry and stresses

In order to study the fretting performance of the armouring tendons, an investigation of the contact geometry and the associated stresses was required.

From the specimen it was observed that the fretting damage occured at two almost circular regions on either side of the inner tendon outer surface (Confer Figure 6.32 a). This is explained by the fact that the curvature of the outer tendon is higher than for the inner tendon along the line of possible contact. Thus contact will occur at one point on each side of the tendon centre line.

The Herz contact theory assumes that the surrounding material volume is large compared to the volume having locally high stresses at the contact area. As the observed contact areas were found to be of similar dimension as the cross section area of the tendons, this theory was considered irrelevant in this case. A simplified approach was therefore introduced, assuming that the contact area is circular with a surface radius of curvature equal to the curvature of the line of possible contact. The contact area and stresses can then be found by the following procedure (see Figure 6.32 b):

 ISBN 82-7119-427-5 ISSN 0802-3271

1. Calculate the curvature along the possible contact line κ.

2. Express the indentation u as a function of the contact circle radius c and the curvature found above

3. Express the maximum contact stress σ_c by Hookes law using the Youngs modulus C_σ, the indentation u and the tendon thickness b.

4. Assume a linear distribution of the contact stress and calculate the total force from the contact area.

5. Determine the force resulting from the common area of two crossing tendons and the average contact pressure between them σ_{22}.

6. Due to the observation of two contact regions, the contact stress and geometry is found by equating the result from step 4 with half the value from step 5

By using the above procedure, the following results emerge for the maximum contact stress σ_c and the contact radius c:

$$\sigma_c = \sqrt{C_\sigma \, \sigma_{22} \, \frac{a^2}{2\pi b R} \, \frac{\sin^2\alpha}{\tan 2\alpha}} \tag{6.2}$$

$$c = \sqrt{\frac{R}{\sin^2\alpha \, \cos 2\alpha}} \left[\frac{\sigma_{22}}{C_\sigma} \, \frac{a^2 b}{2\pi R} \, \frac{\sin^2\alpha}{\tan 2\alpha}\right]^{\frac{1}{4}} \tag{6.3}$$

 ISBN 82-7119-427-5 ISSN 0802-3271

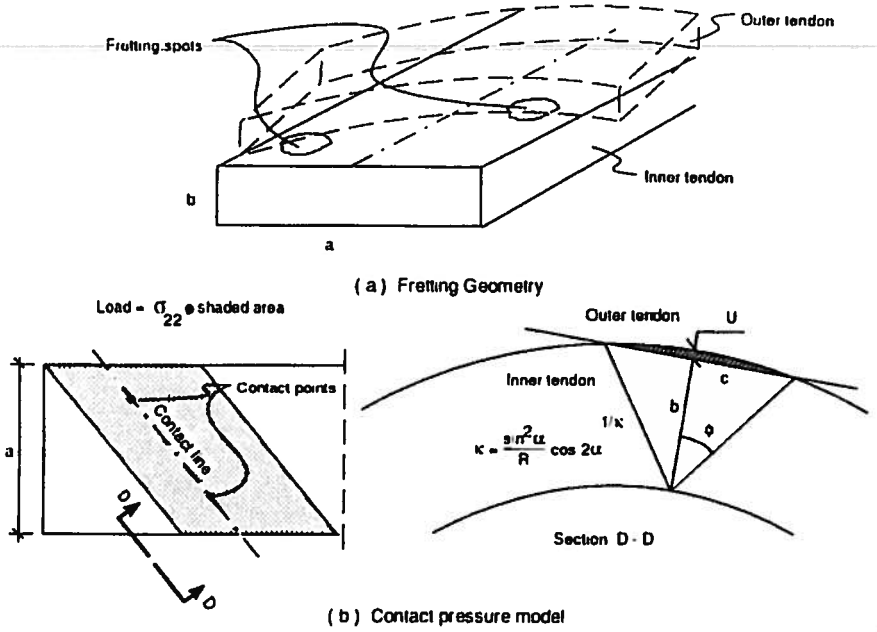

Figure 6.32 Consideration of tendon contact geometry and stresses

6.6.6 Results from initial analyses

The result from the SESAM analysis showed an increase in the longitudinal stress at the tendon bend of 0.26 MPa for each MPa in axial stress. This was, however, based on assuming that the tendon had a sharp bend, see Figure 6.4. However, by inspecting the tendons in the end fitting, it was found that the actual directional change was much smoother than indicated in Figure 6.4, as a radius of curvature of 30-40 mm was measured. The major part of axial load in the tendon will therefore be transmitted into the epoxy by means of membrane action only.

This was confirmed by modelling the actual geometry by use of the SESAM program. The resulting bending stress was now reduced to 0.02 MPa per MPa axial stress, which also shows the importance of the detail design and manufacture of the end fitting.

Figures 6.33 and 6.34 show the curvature distributions obtained by PAS at four alternative tension levels for the two load sequences. It is seen that as the tension increase, the curvature build up at the end of the end fitting. Two distinct peaks are observed. The left peak is due to the linear increase in stiffness of the bending stiffener, whereas the second peak is due to

the step in stiffness between the bare pipe and the last 200 mm of the bending stiffener. The largest curvature occur in Load sequence 1. This is due to the 10^o end angle, which is reduced to 5^o for Load sequence 2.

Table 6.5 gives the tendon axial stresses for the armouring layers as well as the contact pressure between the armouring layers as obtained by CAFLEX for four alternative tension levels and at 250 bar internal pressure. By using the contact pressures given in Table 6.5 in Eq.(6.2) and Eq.(6.3) it was found that the local contact stress between the tendons would vary in the range 28-60 MPa, whereas the corresponding contact circle radius would vary in the range 0.6-0.8 mm for Load sequence 2. The observed fretting spots were slightly larger, having a radius in the range 1-1.5 mm [6.5]. It is noted that the contact areas will tend to increase during the wearing process.

Table 6.5 Axial stresses due to axisymmetric loading

Quantity	T=0.2kN	T=50 kN	T=200 kN	T=500 kN
Axial stress σ_a Outer layer (MPa)	140	168	252	420
Axial stress σ_a Inner layer (MPa)	153	184	276	458
Contact pressure σ_{22} (MPa)	1.9	2.3	3.4	5.6

 ISBN 82-7119-427-5 ISSN 0802-3271

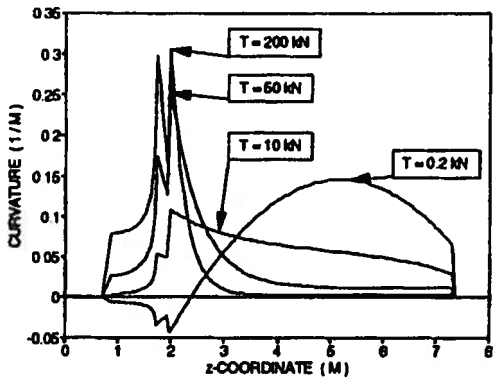

Figure 6.33 Curvature distributions for Load sequence 1 of Pipe 1 fatigue testing

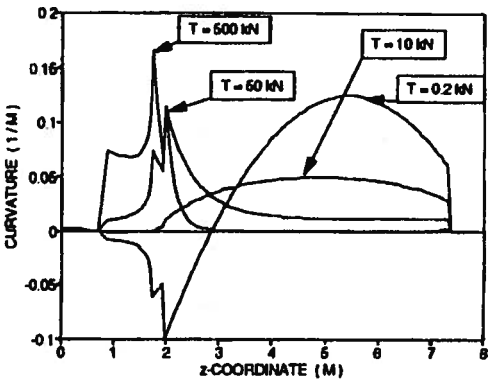

Figure 6.34 Curvature distributions for Load sequence 2 of Pipe 1 fatigue testing

6.6.7 Results and discussion of the AFLEX analyses

Figure 6.35 shows the normalized stress ranges obtained in the outer layer for both load sequences at the failure cross section. The stresses were normalized with respect to the theoretical fatigue limit which in this case was assumed to be 472 MPa at zero mean stress. This value was based on fatigue tests of individual tendons as reported by Eknes and Berge [6.5]. It is seen that the stresses are within the fatigue limit since all values are below 1.0. This confirms the observation that no fatigue failures were observed in these fractures.

It is seen that the stress values are almost constant around the circumference. This means that there is limited influence from bending in this case. This is caused by the bending stiffener design providing the maximum curvature to occur far away from the end fitting restraint.

The distribution of the maximum stress ranges of the inner layer are shown by contour plots in Figures 6.36 and 6.37 for Load sequence 1 and Load sequence 2 respectively. In these figures the pipe has been rotated 90 degrees towards the reader, so that the compressive side of the pipe structure is positioned at Z^3=0, closest to the reader.

 ISBN 82-7119-427-5 ISSN 0802-3271

It is seen that for both load sequences, there are relative low stresses at the compressive side. This is reasonable since bending will induce tendon axial compressive stresses. The stresses on the tensile side were found to be higher. Since the large part of the fatigue failures were observed on the compressive side, this imply that the stress range was not the governing parameter in this case.

The distribution of the maximum relative displacement ranges are shown by similar contour plots in Figures 6.38 and 6.39 for Load sequence 1 and Load sequence 2 respectively. The fretting failures (for the first 3 m of the pipe) are further indicated by circular markers in Figure 6.39. By looking at the relative displacements it is seen that the relative displacements occuring in Load sequence 2 were smaller than in Load sequence 1. This is caused by the fact that the curvature changes were smaller and that the contact pressures were higher in Load sequence 2, thus creating less sliding of the armouring.

According to Nakazawa et al. [3.9], fretting fatigue occured for relative displacement amplitudes up to 20 μm, i.e. displacement ranges up to 40 μm at a contact stress of 50 MPa. From Figure 6.39 it is seen that for Load sequence 2 there is a large area right outside the bending stiffener (At Z^l=1.98 m) in which the relative displacements are in the range 20-70 μm. This is partly within the fretting fatigue regime as reported in [3.9]. Spots of such low values are also found evenly distributed along the compressive side and it is seen that fretting failures occured in such areas with a concentration of failures within the largest area calculated by the theoretical model. It is however noted that corresponding minimum relative displacement areas are also observed on the tensile side which should indicate that similar failures should be found there too. Such failures are, however, not found in the experiments. This can be explained by the fact that the theoretical model has been based on a friction spring stiffness that will give the full magnitude of the friction force for 0.1 mm sliding, combined with a friction coefficient of 0.05 between the two armouring layers and 0.1 between the inner layer and the sheath. In the stick regime, however, the coefficient of friction may be considerably higher [3.3], thus giving locally higher friction within the minimum relative displacement areas. As the stresses at the tensile side is higher than on the compressive side, higher contact pressures will be found on the tensile side. Thus stick-slip

 ISBN 82-7119-427-5 ISSN 0802-3271

may have been suppressed on the tensile side, i.e. fretting induced fatigue was not initiated on this side.

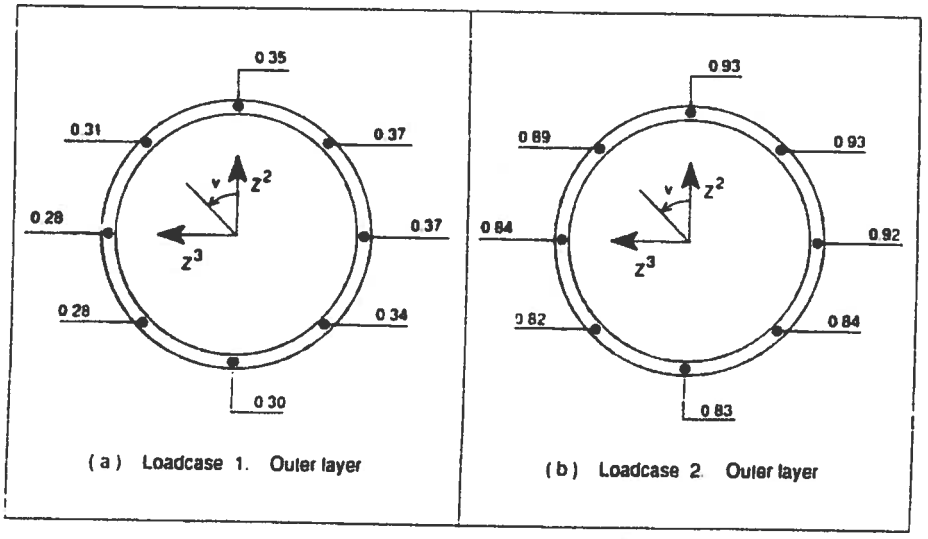

Figure 6.35 Normalized stress ranges in the outer layer failure cross-section of Pipe 1

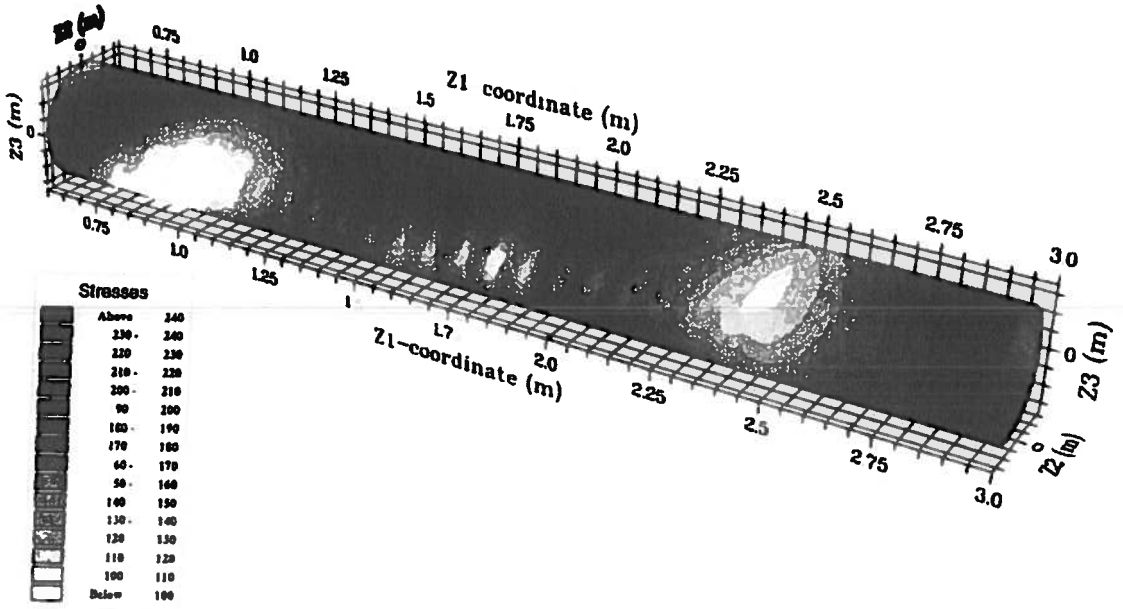

Figure 6.36 Distribution of maximum stress ranges in inner layer of Pipe 1, Load seq.1

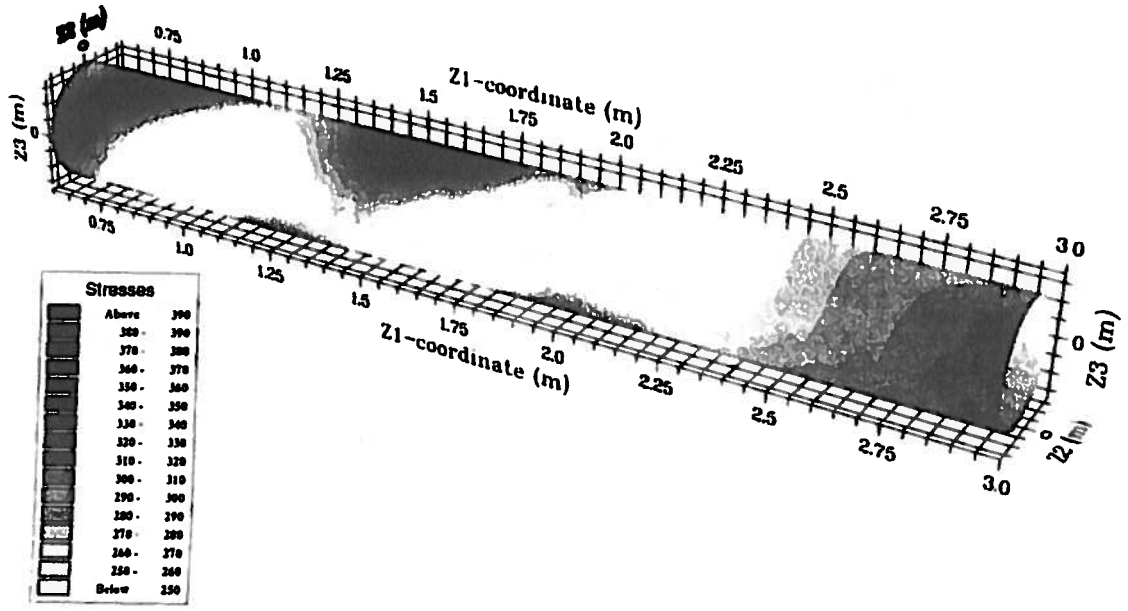

Figure 6.37 Distribution of maximum stress ranges in inner layer of Pipe 1, Load seq. 2

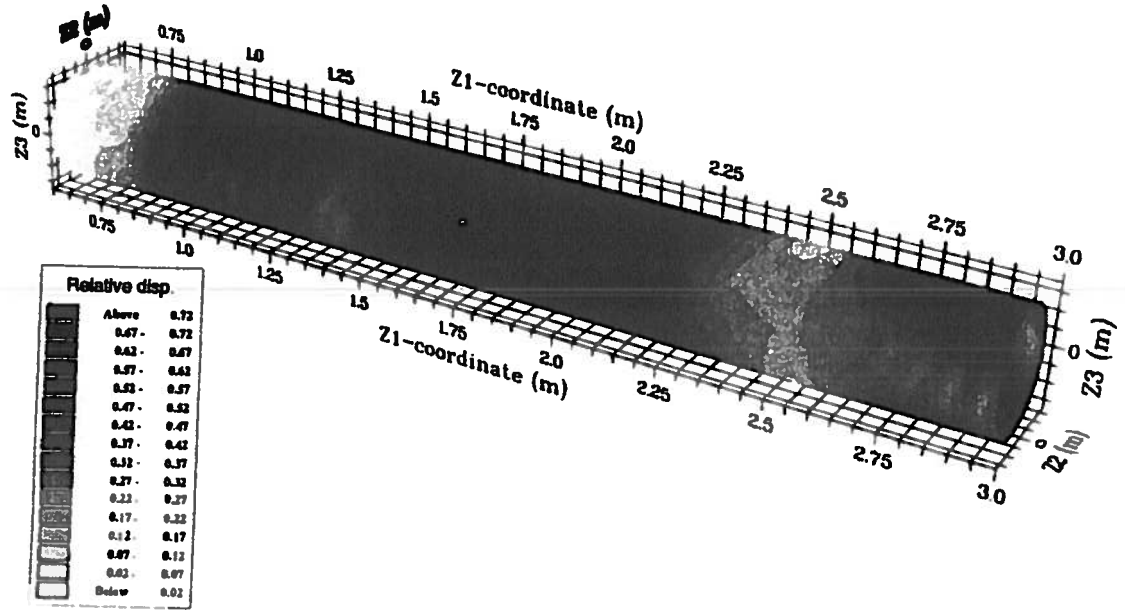

Figure 6.38 Distribution of maximum relative displacement ranges for Pipe 1, Load seq. 1

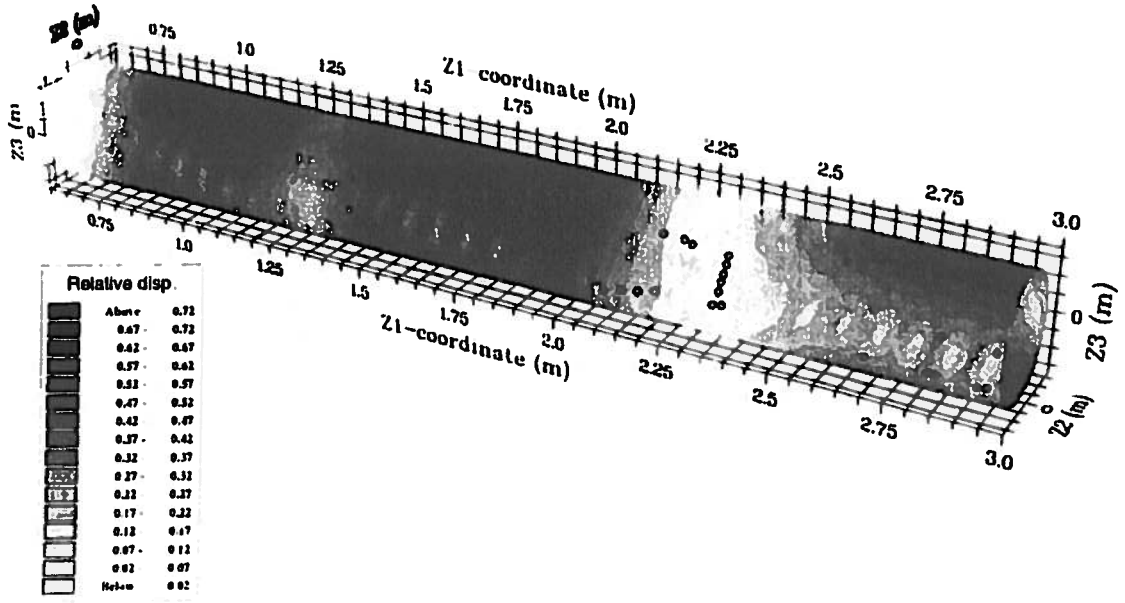

Figure 6.39 Distribution of maximum relative displacement ranges for Pipe 1, Load seq. 2

 ISBN 82-7119-427-5 ISSN 0802-3271

7 CONCLUDING REMARKS

The main intention of this study has been to improve existing methods for stress and fatigue analysis of nonbonded flexible pipe armouring exposed to dynamic loading.

The overall conclusion from the investigations carried out is that the derived finite element model represents a significant step forward, compared to existing formulations.

The main advantage of the present formulation compared to existing models is its capability to consider realistic boundary conditions for individual tendons, and to analyse a pipe with varying curvature. Such improvements are important as both features are necessary when dealing with stress analysis of a riser termination, where the most severe fatigue damage normally is found.

The present model is shown to give good correlation with experimental data, both with regard to stresses and displacements.

The potential of the method is to perform lifetime analysis of flexible pipe termination on the basis of *SN*-data in a similar way as for conventional steel risers. Evaluation of fretting fatigue and wear should also become possible. The lack of test data related to various failure modes is, however, obvious, and calls for extensive future testing in order to make the present method applicable for practical design of flexible risers.

 ISBN 82-7119-427-5 ISSN 0802-3271

More specific conclusions will be given in the following.

7.1 Conclusions

An 8 degree of freedom curved beam element has been developed. This has been obtained by application of kinematic restraints forcing the tendon element to slide on the deformed cylinder. The restraints have been formulated by use of differential geometry and eliminates the need for a fixed reference system. The nonlinear equations have been established by an updated Lagrangian formulation and solved by a Newton-Raphson incremental procedure. The stresses and displacements of the tendon are defined from the twist, curvatures and displacements along the local curvilinear axes. This gives an efficient formulation. The model allows for arbitrary boundary conditions as well as contact forces induced by friction. The formulation can handle arbitrary load histories defined by any combination of tension and corresponding global curvature distribution. This is known to be sufficient to analyse the bending stiffener region of flexible pipes. The formulation has been implemented into the computer program AFLEX.

Numerical studies has been carried both to verify the model and to study various physical effects. Comparisons between the numerical and analytical results obtained for constantly curved pipes show excellent agreement.

The effect of variable curvature combined with zero friction has been investigated. It has been shown that the results obtained by analytical solutions based on constant curvature can be used to find conservative estimates for twist and changes of normal curvature for an individual tendon. The tendon movements on the supporting surface are, however, significantly underestimated by the analytical expressions.

Transverse displacements have also been studied for friction-free pipes as a function of tension. The results show that the geodesic represents the upper limit for the displacements as the tension is increased. At low tensile stresses the tendon will be restrained from moving to the geodesic by the cross section stress resultants induced by the twist and changes in curvatures needed to reach the geodesic.

One effect of friction is that the transverse displacements will be significantly reduced compared to the geodesic solution. It is, however, shown that these displacements will not in general be completely eliminated as one may conclude from simple analytical considerations. This is due to the fact that the resultant friction force depends on the slip direction. At zero transverse displacement, the transverse friction force component is zero. Slip will therefore take place until the transverse friction force component balance the transverse tension component.

The maximum longitudinal slip is insignificantly influenced by friction. This is due to the fact that the shear stresses needed to keep the tendon fixed are much higher than the friction resistance.

The effect of selecting alternative friction spring formulations has been studied. The results show that a hyperelastic spring formulation gives similar results for axial stress ranges as a Coulomb friction model provided that the curvature history is periodic and include change in direction. However, in order to follow the true stress history, the Coulomb friction model has to be used.

For prediction of stress ranges, the effect of selecting different load histories has been found to have limited influence as long as the start and end values are equal.

Under action of friction, end restraint and variable curvature, high axial stresses may occur. This is caused by the fact that the curves described by the tendon at the tensile and compressive sides of the pipe have different length. In order to eliminate the length difference, tendon is fed into the unbalanced section thus inducing axial stresses by friction.

A case study carried out on a 8-inch flexible riser shows that high stresses will occur at the point the global curvature starts for extreme loading. The maximum stress is dominated by friction induced axial stress and bending stress caused by local transverse curvature. The maximum is found close to the neutral axis of global bending. The transverse tendon movements have been found to be eliminated for the inner layer and limited for the outer layer.

 ISBN 82-7119-427-5 ISSN 0802-3271

Comparisons made between the numerical solution and an existing model for the 8-inch riser demonstrate that simplified models can not be used to calculate stresses at end restraints. Conservative estimates can, however, be obtained for the tendon movements.

An improved analytical formula for calculating the friction moment has been developed. This expression has been found to give good agreement with test data.

The geometric stiffness effect being observed as an increase in the sliding bending stiffness as the pressure is increased, has been given a physical interpretation. A simple analytical formula that describes this phenomenon has been developed.

Experimental work has been carried out to verify the stresses predicted by the numerical model. This has been obtained by measuring strains in one outer layer tendon of a 4-inch test pipe. Both axial stress distribution and local bending stresses due to transverse curvature were measured. The results show that there is good agreement between calculated and measured bending stresses, specially at high tension levels. For the axial stress, deviations have been found for some cases. This is explained by the difficulties of correctly describing the curvature distribution as the curvature gradients were high in the tests. The measurements, however, confirm that axial stresses will build up in a similar way as predicted by the numerical model.

In order to estimate the end fitting axial stiffness and to investigate local stress effects inside the end fitting the computer program SESAM has been used. The results show that local bending stresses will occur at the tendon bend inside the epoxy casting. The stress values have been found to be sensitive to the geometry of the bend.

Fatigue testing has been carried out on two 4-inch flexible pipes. For one of the specimens the fatigue failures were found at the point of tendon directional change inside the end fitting in both layers. This was caused by a combination of local bending stresses induced by tendon tension and a global moment maximum at the end fitting. Good correlation has been found between the position of the failures and the predicted stress ranges.

For the other specimen the primary failure was found to be fretting fatigue in the inner layer.

 ISBN 82-7119-427-5 ISSN 0802-3271

A simple analytical model has been developed to predict the maximum contact stress at individual contact points between two cross-wound armouring layers in direct contact. Good agreement has been found between the predicted contact geometry and the observations. Good correlation has also been found between the position of the fractures and the predicted conditions of relative displacements.

7.2 Recommendations for further work

It has been found that the developed model is capable of accurately describing relevant conditions of stresses and slip for predicting different failure modes. The potential of the method is therefore to perform lifetime analysis on the basis of various failure modes like metal fatigue, fretting and wear. However, the failure modes found from the experimental work are not included in the failure models presented so far in the literature. This together with development of new flexible pipe designs to meet future requirements of deep water petroleum production requires future research in order to characterize relevant failure modes.

The high stress ranges found in the 8-inch flexible riser indicates that the approach of not allowing stress ranges to exceed the fatigue limit may not be adequate. If this is the case, the *SN*-approach has to be used in order to calculate the fatigue life. More research work has to be done to establish *SN*-data for relevant environmental conditions.

In this study the outer tension armouring layers have been focused on. Other armouring elements such as the interlocked Zeta spiral will require another model. Due to direct metal to metal contact and high contact pressures, fretting fatigue may be critical. Development of a model for describing the micro stress and relative displacement conditions for such layers will represent an interesting extension of the present work.

The present model is based on consideration of one tendon exposed to a given set of load and displacement conditions. Implementing the present model for one tendon into a model based on total cross section integration represents a natural extension of the model.

 ISBN 82-7119-427-5 ISSN 0802-3271

The fatigue tests demonstrated that the final damage of the pipe cross section will result from progressive failures of individual tendons. Failure of one tendon will not cause collapse by itself but will induce stress redistribution in the cross section. The model described in the above paragraph will enable such effects to be included in the analysis.

It has been assumed in the present formulation that each tendon can be analysed without taking into account any interaction with other tendons in the same layer. This has been considered to be a reasonable assumption as long the curvature is less than the critical curvature. Due to production tolerances, however, two tendons may be in initial contact prior to pipe bending. Such effects may also be studied by including a sideways contact formulation in the above model.

 ISBN 82-7119-427-5 ISSN 0802-3271

8 REFERENCES

[1.1] Bjelland, O.: *The Veslefrikk Transfer Systems*, Proc. of the Offshore Technology Conference, OTC, Houston, 1990.

[1.2] Brown, P.A., Soltanahmadi, A., Chandwani, R.: *Problems Encountered in Detailed Design of Flexible Riser Systems*, Engineering Structures, Vol.11, 1989.

[1.3] Pettenati-Auziere, C.: *Flexible Dynamic Risers, State of the Art*, Norwegian Petroleum Society, Flexible Pipe Technology Seminar, Oslo, Norway, 1986.

[1.4] Sødahl, N.R. : *Methods for Design and Analysis of Flexible Risers*, Dr.ing Thesis, Division of Marine Structures, the Norwegian Institute of Technology, NTH, Trondheim, Norway, 1990.

[1.5] Mo, O., Torset, O.P.: *Requirements and Applicable Standards for Design, Manufacturing and Installation of Flexible Pipes*, Engineering Structures, Vol.11, 1989.

[1.6] IFP, SINTEF: *CAFLEX, Computer Program for Capacity Analysis of Flexible Pipes*, Theory Manual, SINTEF, Struct. Engr., Report. no. STF71 F91019, July 1990.

 ISBN 82-7119-427-5 ISSN 0802-3271

[1.7] Feret, J.J, Bournazel, C.L, Rigaud, J.: *Evaluation of Flexible Pipes' Life Expectancy Under Dynamic Conditions*, Proc. of the Offshore Technology Conference, OTC 5230, Houston, 1986.

[1.8] Larsen, C.M., Leira, B.J., Olufsen, A., Sødahl, N.: *Design Methods for Flexible Risers*, Proc. of the International Conference on Behaviour of Offshore Structures, BOSS, London, 1992.

[1.9] Larsen, C.M., Olufsen, A.: *Extreme Response Estimation of Flexible Risers*, Proc. of the International Conference on Offshore and Polar Engineering, ISOPE, San Fransisco, 1992.

[1.10] Haver, S.: *Long Term Response Analysis, Advantages and Present Limitations*, STATOIL, Deep Water Jacket Seminar, Trondheim, 1985.

[1.11] Farnes, K.A.: *Long-term Statistics of Response in Non-linear Marine Structures*, Dr.ing Thesis, Division of Marine Structures, The Norwegian Institute of Technology, NTH, Trondheim, Norway, 1990.

[1.12] Larsen, C.M, Passano, E.: *Extreme Response Estimation for Marine Risers*, Proc. of the Offshore Mechanics and Arctic Engineering Conference, OMAE, Houston, 1990.

[1.13] Leira, B.J., Olufsen, A.: *Lifetime Analysis of Flexible Pipes by Frequency and Time Domain Methods*, SINTEF, Struct. Engr., Report no. STF71 F91003, 1991.

[1.14] Larsen, C.M: *Flexible Riser Analysis - Comparison of Results from Computer Programs*, Marine Structures, pp. 103-119, 1992.

[1.15] Kodaissi, E., Lemarchand, E., Narzul, P.: *State of the Art on Dynamic programs for Flexible Riser Systems*, Proc. of the Offshore Mechanics and Arctic Engineering Conference, OMAE, 1990.

 ISBN 82-7119-427-5 ISSN 0802-3271

[1.16] Oliveira, J.G.de, Goto, Y., Okamoto, T.: *Theoretical and Methodological Approaches to Flexible Pipe Design and Application*, Proc. of the Offshore Technology Conference, OTC 5021, May 1985.

[1.17] Feret, J.J, Bournazel, C.L.: *Calculation of Stresses and Slip in Structural Layers of Unbonded Flexible Pipes*, Proc. of the Offshore Mechanics and Arctic Engineering Conference, OMAE, 1986.

[1.18] McNamara, J.F, Harte, A.M: *Three Dimensional Analytic Simulation of Flexible Pipe Wall Structure*, Proc. of the Offshore Mechanics and Arctic Engineering Conference, OMAE, 1989

[1.19] Often, O., Løtveit, S.A.: *A Common Theoretical Formulation for Bonded and Nonbonded Flexible Pipes under Axisymmetric Loads*, Proc. kursdagene, The Norwegian Institute of Technology, NTH, Trondheim, January 1990.

[1.20] Witz, J.A., Tan, Z.: *On the Axial-Torsional Behaviour of Flexible Pipes, Umbilicals and Marine Cables*, Department of Offshore Engineering, Univ. College of London, May 1991.

[1.21] Knapp, R.H.: *Derivation of a new Stiffness Matrix for Helically Armoured Cables considering Tension and Torsion*, Int. Journ. of Numerical Methods, Vol.14, pp.515-529, 1979.

[1.22] Huang, N.C.: *Finite Extension of an Elastic Strand With a Central Core*, Trans. ASME, Vol.45, December 1978.

[1.23] Costello, G.A, Philips, J.W.: *Contact Stresses in Twisted Wire Cables*, Journal of the Engineering Mechanics Division, ASCE, Vol.99, No. EM2, April 1973.

[1.24] Costello, G.A, Philips, J.W.: *A More Exact Theory for Twisted Wire Cables*, Journal of the Engineering Mechanics Division, ASCE, Vol.100, No. EM5, October 1974.

 ISBN 82-7119-427-5 ISSN 0802-3271

[1.25] Costello, G.A, Blanco, J.A.: *Cylindrical Constraint of Helical Springs*, Trans. ASME, June 1974.

[1.26] Costello, G.A, Philips, J.W.: *Effective Modulus of Twisted Wire Cables*, Journal of the Engineering Mechanics Division, ASCE, Vol.102, No. EM1, February 1975.

[1.27] Costello, G.A.,Sinha, S.K.: *Torsional Stiffness of Twisted Wire Cables*, Journal of the Engineering Mechanics Division, ASCE, Vol.103, No. EM4, August 1977.

[1.28] Lanteigne, J.: *Theoretical Estimation of the Response of Helically Armoured Cables to Tension, Torsion and Bending*, Journal of Applied Mechanics, Vol. 52, pp. 423-432, June 1985.

[1.29] Velinsky, S.A. : *Analysis of Fiber-Core Wire Rope*, Trans. ASME, Vol.107, pp.388-393, Sept.1985.

[1.30] Lutchansky, M.: *Axial Stresses in Armor Wires of Bent Submarine Cables*, Journal of Engineering for Industry, August 1969.

[1.31] Tan, Z. Witz, J.A., Lyons, G.J., Fang, J. and Patel, H. : *On the Influence of Internal Slip between Component Layers of Unbonded Flexible Pipes*, Proc. of the Offshore Mechanics and Arctic Engineering Conference, OMAE, 1991.

[1.32] Leclair, R.A., Costello, G.A.,: *Axial, Bending and Torsional Loading of a Strand with Friction*, Proc. of the Offshore Mechanics and Arctic Engineering Conference, OMAE, Houston, 1987.

[2.1] Kirchoff, G.: *Ueber das Gleichgewicht und die Bewegung eines uendlich dunnen elastischen Stabes*, J. reine angew. Math., Vol. 56, pp. 285-313.

[2.2] Love, A.E.H.: *A Treatise on the Mathematical Theory of Elasticity*, Dover Publ., 4th Edition, 1944.

[2.3] Hay, G.E.: *The Finite Displacement of Thin Rods*, Trans. American Math. Soc., Vol. 51, pp. 65-102, 1942.

[2.4] Ericksen, J.E, Truesdell, C.: *Exact Theory of Stress and Strain in Rods and Shells*, Arch. Rat. Mech. Anal., Vol. 1, pp. 295-323, 1958.

[2.5] Huang, Nai-Chien: *Theories of Elastic Slender Curved Rods*, Journ. of Applied Math. Phys., ZAMP, Vol.24, pp. 1-19, 1973

[2.6] Washizu, K.: *Some Considerations on a Naturally Curved and Twisted Slender Beams*, J.Math. Phys., Vol. 43, pp. 111-116, 1964.

[2.7] Eisenhart, L.P.: *A Treatise on the Differential Geometry of Curves and Surfaces*, Dover Publ. Inc., 1960

[2.8] Borisenko, A.I., Tarapov, I.E. : *Vector and Tensor Analysis with Applications*, Prentice-Hall, Inc., 1968

[2.9] Keener, James, P. : *Principles of Applied Mathematics*, Addison-Wesley Publishing Company, 1988.

[2.10] Søreide, T.H.: *Lecture notes on Analysis of Non-linear Structures*, Division of Structural Mechanics, The Norwegian Institute of Technology, NTH, Trondheim, Norway, 1989

[2.11] Levold, E. : *Solid Mechanics and Material Models including Large Deformations*, Ph.D. Thesis, Division of Structural Mechanics, The Norwegian Institute of Technology, NTH, Trondheim, Norway, 1990.

[2.12] Hibbit, H.D., Marcal, P.V., and Rice, J.R.: *A Finite Element Formulation for Problems of Large Strain and Large Displacements*, Intern. Journ. of Solids and Structures, Vol.6, pp. 1069-1086, 1970

 ISBN 82-7119-427-5 ISSN 0802-3271

[2.13] McMeeking, R.M. and Rice, J.R.: *Finite Element Formulations for Problems of Large Elastic-plastic Deformation*, International Journ. of Solids and Structures, Vol.11, pp. 601-661, 1975

[2.14] Oden, J.R.: *Finite Elements of Nonlinear Continua*, McGraw-Hill, 1972.

[2.15] Bathe, K.J.: *Finite Element Procedures in Engineering Analysis*, Prentice-Hall Inc., 1982.

[2.16] Bergan, P.G.: *Nonlinear Analysis of Plates Considering Geometric and Material Effects*, Ph.D Dissertation, Univ. of Berkeley, 1971. Second edition: Report No. 72-1, Division of Structural Mechanics, The Norwegian Institute of Technology, NTH, Trondheim, 1972

[2.17] Søreide, T.H.: *Collapse Behaviour of Stiffened Plates using Alternative Finite Element Formulations*, Report No. 77-3, Division of Structural Mechanics, The Norwegian Institute of Technology, NTH, Trondheim, 1973

[2.18] Mattiason, K.: *On the Co-Rotational Finite Element Formulation for Large Deformation Problems*, Publication 83:1, Department of Structural Mechanics, Chalmers University of Technology, Gøteborg, 1983

[2.19] Michalowski, R., Mroz, Z.: *Associated and Non-associated Sliding Rules in Contact Friction Problems*, Arch. Mech., Vol.30, pp. 259-276, Warszawa, 1978.

[2.20] Meyer, D.W., Plesha, M.E., Cooper, R.F.: *A Contact Friction Algorithm including Nonlinear Viscoelasticity and Single Yield Surface Provision*, Computers & Structures, Vol.42, No.6, pp. 913-925, 1992.

[2.21] Fiskvatn, Audun: *Elementmetoden*, Kompendium (In Norwegian), Division of Structural Mechanics, The Norwegian Institute of Technology, NTH, Trondheim, Norway, April 1980.

 ISBN 82-7119-427-5 ISSN 0802-3271

[3.1] Rabinowicz, E. : *Friction and Wear of Materials*, John Wiley & Sons, 1965.

[3.2] Rabinowicz, E. : *The Wear Coefficient - Magnitude, Scatter, Uses*, ASME-ASLE International Lubrication Conference, Calif. August 18-21, 1980.

[3.3] Vingsbo, O., Odfalk, M. : *Fretting Maps and Fretting Behaviour of some FCC Metal Alloys*, Proc. Int. Conf. on Wear of Materials, Denver, The American Soc. of Mechanical Engineers, 1989.

[3.4] Mindlin, R.D., Deresiewicz, H. : *Elastic Spheres in Contact Under Varying Oblique Forces*, Journal of Applied Mechanics, Trans. ASME, pp. 327-344, September 1953.

[3.5] Mindlin, R.D. : *Compliance of Elastic Bodies in Contact*, Journal of Applied Mechanics, Trans. ASME, Vol. 71, pp. 259-268, September 1949.

[3.6] Deresiewicz, H. : *Oblique Contact of Nonspherical Elastic Bodies*, Journal of Applied Mechanics, Trans. ASME, pp. 623-624, December 1957.

[3.7] Mindlin, R.D., Mason, W.P., Osmer, T.J., Deresiewicz, H. : *Effects of an Oscillating Tangential Force on the Contact Surfaces of Elastic Spheres*, Proc. of the First U.S. National Congress of Applied Mechanics, pp. 203-208, 1951.

[3.8] Vingsbo, O., Søderberg, S. : *On Fretting Maps*, Wear, 126, pp.131-147, 1988.

[3.9] Nakazawa, K., Sumita, M., Maruyama, N. : *Fretting Fatigue of High Strength Steels in Sea Water*, Proc. Evaluation of materials Performance in Severe Environments. Kobe, 1989.

[3.10] Waterhouse: *Fretting Fatigue*, Waterhouse R.B. (ed.), Applied Science, 1981

 ISBN 82-7119-427-5 ISSN 0802-3271

[3.11] Holmberg, K.: *Friction in low speed lubricated rolling and sliding contacts*, Thesis for the degree of Doctor of Technology accepted by the Helsinki University of Tecnology, Otaniemi, Technical Research Centre of Finland, Espoo, April 1984.

[3.12] Nielsen, R., Colquhoun, R.S. McCone, A., Witz, J.A, Chandwani, R. : *Tools for Predicting Service Life of Dynamic Flexible Risers*, European Offshore Mechanics Symposium. Trondheim, 1990

[4.1] *Unigraph+2000*, User's Guide, Uniras A/S, February 1991.

[5.1] Skallerud, B. : *Damping Models and Structural Damping in Pipe 1*, SINTEF, Struct. Engr., Draft report no 2.2-8, May, 1991.

[5.2] Skallerud, B. : *Damping Models and Structural Damping in Pipe 2*, SINTEF, Struct. Engr., Report no. STF71-F91059, November, 1991.

[5.3] Olufsen, A. : *Project Overview FPS 2000/Flexible Risers and Pipes*, Proc. from Flexible Pipe Technology, Seminar, 18-20 February, 1992.

[5.4] Sævik, S., Engseth, A., Bech, A. : *Models for Response Analysis of Flexible Pipe Wall Sections*, SINTEF Draft report no. 2.1-27, February, 1992.

[6.1] *PAS - Pipeline Analysis System*, Users Manual, Version 1.0, A. R. Reinertsen, Trondheim, January 1990.

[6.2] *SESAM/SESTRA Super Element Structural Analysis, User's Manual*, Veritas Sesam Systems, Høvik, 1st September,1991

[6.3] *Kompositboken*, Plast og Gummitekniska Institutet, Stockholm, 1988 (in Swedish).

[6.4] Eknes, A., Berge, S.: *Failure Analysis of Pipe 2 Tested in Fatigue*, Draft Report, SINTEF Structural Engineering/FCB, August 1992.

[6.5] Eknes, A., Berge, S.: *Failure Analysis of Pipe 1 Tested in Fatigue*, Draft Report, SINTEF Structural Engineering/FCB, August 1992.

 ISBN 82-7119-427-5 ISSN 0802-3271

APPENDIX A

PROOF OF GEODESIC CURVE EXPRESSIONS

A.1 Displacements, torsion and curvatures

Reference is given to Eqs.(2.26)-(2.28). The surface normal vector components which are represented by the second term in these equations, are determined by taking the cross-product between the two tangent vectors obtained by differentiating the position vector components of a point on the toroid given by Eqs.(2.4)-(2.6) with respect to ν and ϕ respectively. The result is:

$$\frac{\partial S}{\partial Z^1} = -R\rho\cos\nu\sin\phi + R^2\cos^2\nu\sin\phi \qquad \text{(A.1)}$$

$$\frac{\partial S}{\partial Z^2} = R\rho\cos\nu\cos\phi - R^2\cos^2\nu\cos\phi \qquad \text{(A.1)}$$

$$\frac{\partial S}{\partial Z^3} = R\rho\sin\nu\cos^2\phi - R^2\sin\nu\cos\nu\cos^2\phi \qquad \text{(A.3)}$$

In order to solve the differential equations and to find the associated torsion and curvatures along the curve, coordinate derivatives with respect to the arc length coordinate up to third order, are needed. The derivatives are determined on the basis of the same position vector

 ISBN 82-7119-427-5 ISSN 0802-3271

components with consideration of the fact that v and ϕ both are one to one functions of the arc length coordinate X^1 as:

$$Z^1_{,1} = \rho\cos\phi\phi_{,1} + R\sin v\sin\phi v_{,1} - R\cos v\cos\phi\phi_{,1} \tag{A.4}$$

$$\begin{aligned} Z^1_{,11} = {} & -\rho\sin\phi\phi^2_{,1} + \rho\cos\phi\phi_{,11} + R\cos v\sin\phi v^2_{,1} + R\sin v\cos\phi v_{,1}\phi_{,1} \\ & + R\sin v\sin\phi v_{,11} + R\sin v\cos\phi\phi_{,1}v_{,1} + R\cos v\sin\phi\phi^2_{,1} - R\cos v\cos\phi\phi_{,11} \end{aligned} \tag{A.5}$$

$$\begin{aligned} Z^1_{,111} = {} & -\rho\cos\phi\phi^3_{,1} - 2\rho\sin\phi\phi_{,1}\phi_{,11} - \rho\sin\phi\phi_{,11}\phi_{,1} + \rho\cos\phi\phi_{,111} \\ & - R\sin v\sin\phi v^3_{,1} + R\cos v\cos\phi v^2_{,1}\phi_{,1} + 2R\cos v\sin\phi v_{,1}v_{,11} + 2R\cos v\cos\phi v^2_{,1}\phi_{,1} \\ & - 2R\sin v\sin\phi v_{,1}\phi^2_{,1} + 2R\sin v\cos\phi v_{,11}\phi_{,1} + 2R\sin v\cos\phi v_{,1}\phi_{,11} + R\cos v\sin\phi v_{,1}v_{,11} \\ & + R\sin v\cos\phi v_{,11}\phi_{,1} + R\sin v\sin\phi v_{,111} - R\sin v\sin\phi\phi^2_{,1}v_{,1} + R\cos v\cos\phi\phi^3_{,1} \\ & + 2R\cos v\sin\phi\phi_{,1}\phi_{,11} + R\sin v\cos\phi\phi_{,11}v_{,1} + R\cos v\sin\phi\phi_{,1}\phi_{,11} - R\cos v\cos\phi\phi_{,111} \end{aligned} \tag{A.6}$$

$$Z^2_{,1} = \rho\sin\phi\phi_{,1} - R\sin v\cos\phi v_{,1} - R\cos v\sin\phi\phi_{,1} \tag{A.7}$$

$$\begin{aligned} Z^2_{,11} = {} & \rho\cos\phi\phi^2_{,1} + \rho\sin\phi\phi_{,11} - R\cos v\cos\phi v^2_{,1} + R\sin v\sin\phi v_{,1}\phi_{,1} \\ & - R\sin v\cos\phi v_{,11} + R\sin v\sin\phi\phi_{,1}v_{,1} - R\cos v\cos\phi\phi^2_{,1} - R\cos v\sin\phi\phi_{,11} \end{aligned} \tag{A.8}$$

$$\begin{aligned} Z^2_{,111} = {} & -\rho\sin\phi\phi^3_{,1} + 2\rho\cos\phi\phi_{,1}\phi_{,11} + \rho\cos\phi\phi_{,11}\phi_{,1} + \rho\sin\phi\phi_{,111} \\ & - R\sin v\cos\phi v^3_{,1} + R\cos v\sin\phi v^2_{,1}\phi_{,1} - 2R\cos v\cos\phi v_{,1}v_{,11} + 2R\cos v\sin\phi v^2_{,1}\phi_{,1} \\ & + 2R\sin v\cos\phi v_{,1}\phi^2_{,1} + 2R\sin v\sin\phi v_{,11}\phi_{,1} + 2R\sin v\sin\phi v_{,1}\phi_{,11} - R\cos v\cos\phi v_{,1}v_{,11} \\ & + R\sin v\sin\phi v_{,11}\phi_{,1} - R\sin v\cos\phi v_{,111} + R\sin v\cos\phi\phi^2_{,1}v_{,1} + R\cos v\sin\phi\phi^3_{,1} \\ & - 2R\cos v\cos\phi\phi_{,1}\phi_{,11} + R\sin v\sin\phi\phi_{,11}v_{,1} - R\cos v\cos\phi\phi_{,1}\phi_{,11} - R\cos v\sin\phi\phi_{,111} \end{aligned} \tag{A.9}$$

$$Z^3_{,1} = R\cos v v_{,1} \tag{1.10}$$

$$Z^3_{,11} = -R\sin v v^2_{,1} + R\cos v v_{,11} \tag{A.11}$$

 ISBN 82-7119-427-5 ISSN 0802-3271

$$Z^3_{,111} = -R\cos\nu\nu^3_{,1} - 2R\sin\nu\nu_{,1}\nu_{,11} - R\sin\nu\nu_{,1}\nu_{,11} + R\cos\nu\nu_{,111} \tag{A.12}$$

By solving with respect to the Lagrange multiplier λ in Eq.(2.26) and implementing this result together with Eq.(A.8) in Eq.(2.27), the following differential equation is obtained:

$$\phi_{,1} = \frac{C}{(\rho - R\cos\nu)^2} \tag{A.13}$$

where C is an arbitrary constant which can be determined by observing that $\phi_{,1}$ is antisymmetric about the neutral axis of bending. Thus, by simple geometry at $\nu=\pi/2$:

$$\phi_{,1} = \frac{\cos\alpha}{\rho} \tag{A.14}$$

Along the curve, ν is expressed by the arc length coordinate as:

$$\nu = \frac{\sin\alpha}{R} X^1 \tag{A.15}$$

By using Eq.(A.14) and Eq.(A.15) in Eq.(A.13), then develop $\phi_{,1}$ as a Taylor expansion in R/ρ, and finally integrating with respect to the arc length coordinate X^1, the new ϕ coordinate ϕ^* emerges:

$$\phi^* = \frac{R}{\rho\tan\alpha}\left(\nu + 2\frac{R}{\rho}\sin\nu\right) \tag{A.16}$$

where all R/ρ terms of higher order than one, are neglected. The first term represents the previous ϕ coordinate, whereas the second term represents the change induced when following the geodesic. Further, along the curve:

 ISBN 82-7119-427-5 ISSN 0802-3271

$$R^2 v_{,1}^{*\,2} + (\rho - R\cos\nu)^2 \phi_{,1}^{*\,2} = 1 \tag{A.17}$$

By using Eq.(A.17) and differentiation of Eq.(A.16), the new ν coordinate ν^* is further determined to be:

$$\nu^* = \nu - \frac{R}{\rho}\frac{\cos^2\alpha}{\sin^2\alpha}\sin\nu \tag{A.18}$$

where the second term represents the change in the initial ν coordinate. The total relative displacement between the curve and the toroid is now obtained as:

$$u_{tot} = \rho^2\Delta\phi^2 + R^2\Delta\nu^2 = \frac{R^2}{\rho\tan\alpha}\sqrt{4+\frac{1}{\tan^2\alpha}}\sin\nu \tag{A.19}$$

The longitudinal and transverse components of the slip are then obtained by simple decomposition as:

$$u_1 = \rho\Delta\phi\cos\alpha + R\Delta\nu\sin\alpha = \frac{R^2}{\rho}\frac{\cos^2\alpha}{\sin\alpha}\sin\nu \tag{A.20}$$

$$u_3 = \rho\Delta\phi\sin\alpha - R\Delta\theta\cos\alpha = \frac{R^2}{\rho\tan\alpha}\left(2\sin\alpha+\frac{\cos^2\alpha}{\sin\alpha}\right)\sin\nu \tag{A.21}$$

This concludes the proof regarding the displacements needed relative to the supporting pipe surface in order to follow the geodesic.

The torsion τ and the normal curvature κ_3 are further determined on the basis of the developed differentials and use of Taylor expansion in one term of R/ρ. Thus, by use of Eq.(A.16) and Eq.(A.18) in the differentials of Eqs.(A.4)-(A.12), the following expressions are obtained:

 ISBN 82-7119-427-5 ISSN 0802-3271

$$Z^1_{,1} = \cos\alpha\cos\phi + \frac{R}{\rho}\cos\alpha\cos\nu\cos\phi + \sin\alpha\sin\nu\sin\phi - \frac{\cos^2\alpha}{\sin\alpha}\frac{R}{\rho}\sin\nu\cos\nu\sin\phi \qquad (A.22)$$

$$Z^2_{,1} = \cos\alpha\sin\phi + \cos\alpha\frac{R}{\rho}\sin\phi\cos\nu - \sin\alpha\sin\nu\cos\phi + \frac{\cos^2\alpha}{\sin\alpha}\frac{R}{\rho}\sin\nu\cos\phi\cos\nu \qquad (A.23)$$

$$Z^3_{,1} = \sin\alpha\cos\nu - \frac{\cos^2\alpha}{\sin\alpha}\frac{R}{\rho}\cos^2\nu \qquad (A.24)$$

$$Z^1_{,11} = -\frac{\cos^2\alpha}{\rho}\sin\phi + \frac{\sin^2\alpha}{R}\cos\nu\sin\phi - 2\frac{\cos^2\alpha}{\rho}\cos\nu\sin\phi + \frac{\cos^2\alpha}{\rho}\sin^2\nu\sin\phi \qquad (A.25)$$

$$Z^2_{,11} = \frac{\cos^2\alpha}{\rho}\cos\phi - \frac{\sin^2\alpha}{R}\cos\nu\cos\phi + 2\frac{\cos^2\alpha}{\rho}\cos^2\nu\cos\phi - \frac{\cos^2\alpha}{\rho}\sin^2\nu\cos\phi \qquad (A.26)$$

$$Z^3_{,11} = -\frac{\sin^2\alpha}{R}\sin\nu + 3\frac{\cos^2\alpha}{\rho}\sin\nu\cos\nu \qquad (A.27)$$

$$Z^1_{,111} = -\frac{\sin^3\alpha}{R^2}\sin\nu\sin\phi + \frac{\sin^2\alpha\cos\alpha}{R\rho}\cos\nu\cos\phi + 7\frac{\cos^2\alpha\sin\alpha}{R\rho}\sin\nu\cos\nu\sin\phi \qquad (A.28)$$

$$Z^2_{,111} = \frac{\sin^3\alpha}{R^2}\sin\nu\cos\phi + \frac{\sin^2\alpha\cos\alpha}{R\rho}\cos\nu\sin\phi - 7\frac{\cos^2\alpha\sin\alpha}{R\rho}\sin\nu\cos\nu\cos\phi \qquad (A.29)$$

$$Z^3_{,111} = -\frac{\sin^3\alpha}{R^2}\cos\nu + 4\frac{\cos^2\alpha\sin\alpha}{R\rho}\cos^2\nu - 3\frac{\cos^2\alpha\sin\alpha}{R\rho}\sin^2\nu \qquad (A.30)$$

The normal curvature is then found from classic differential geometry by:

$$\kappa_3 = \sqrt{(Z^1_{,11})^2 + (Z^2_{,11})^2 + (Z^3_{,11})^2} = \frac{\sin^2\alpha}{R}\left(1 - 3\frac{R}{\rho}\frac{\cos^2\alpha}{\sin^2\alpha}\cos\nu\right) \qquad (A.31)$$

ISBN 82-7119-427-5 ISSN 0802-3271

and the torsion by:

$$\tau = \frac{1}{(\kappa_3)^2}\left(Z^1_{,111}(Z^2_{,1}Z^3_{,11}-Z^2_{,11}Z^3_{,1}) + Z^2_{,111}(Z^1_{,11}Z^3_{,1}-Z^1_{,1}Z^3_{,11}) + Z^3_{,111}(Z^1_{,1}Z^2_{,11}-Z^1_{,11}Z^2_{,1})\right) \tag{A.32}$$
$$= \frac{\sin\alpha\cos\alpha}{R}\left(1 - \frac{R}{\rho}\left(\frac{1}{\sin^2\alpha}-3\right)\cos\nu\right)$$

The above concludes the proof regarding torsion and curvature along the geodesic.

A.2 Consideration of tendon rotation along the geodesic

In the above it was shown that normal curvature change and twist will occur along the geodesic. This will induce cross section stress resultants in the tendons. In Chapter 2 the assumption was made that the tendon is fixed to the surface normal, and remain so during deformation of the supporting pipe surface. A possible deviation from this assumption will occur due to the torque induced by the twist. In order to test the assumption of Chapter 2, the tendon is allowed to rotate a fixed angle θ_1 about the longitudinal axis X^1 as shown in Figure A.1. This rotation will be restrained by the tension induced contact stress. By equilibrium and consideration of the tendon rotating on the curved surface, the following torque differential equation is obtained for the infinitesimal element:

$$\frac{dM_1}{dX^1} = Q_1\frac{\kappa_3}{\kappa_t}\theta_1 \tag{A.33}$$

By assuming that the constant rotation θ_1 of the tendon cross section has no influence on the twist which is represented by the second term in Eq.(A.32), M_1 is found directly by the torsion stiffness and the twist. By differentiation of M_1, and use the result in Eq.(A.33), the maximum tension force Q_1 needed in order to keep the cross section at the predefined angle θ_1 is obtained as:

 ISBN 82-7119-427-5 ISSN 0802-3271

$$Q_1 = C_t I_t \frac{\cos^3\alpha}{R\rho}\left(\frac{1}{\sin^2\alpha} - 3\right)\left(\frac{1}{\theta_1}\right) \qquad \text{(A.34)}$$

In Figure A.2 this equation has been studied, by investigating a 4 mm thick and 9 mm wide tendon at 0.1 m layer radius and using 0.5^o as rotation tolerance limit. It is seen that at high curvatures, high longitudinal stresses are needed in order to avoid further rotation for 25^o lay angle, whereas the values are significantly reduced for lay angles above 30^o. Since the lay angles normally used are above 30^o, small deviations will occur between the tendon weak axis and the surface normal even at low axial stresses.

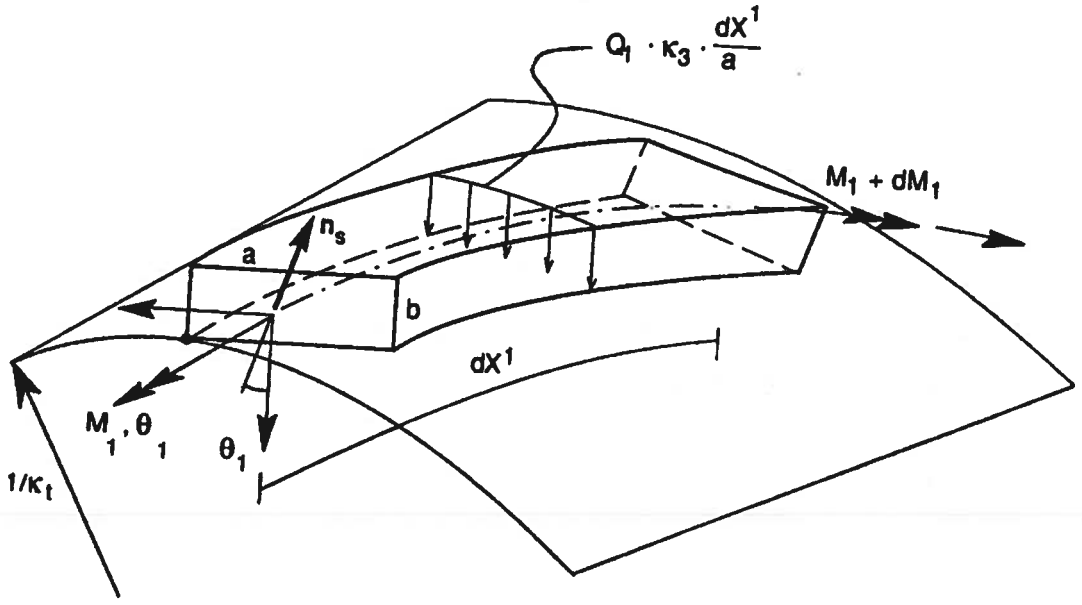

Figure A.1 Torsion equilibrium of infinitesimal element

ISBN 82-7119-427-5 ISSN 0802-3271

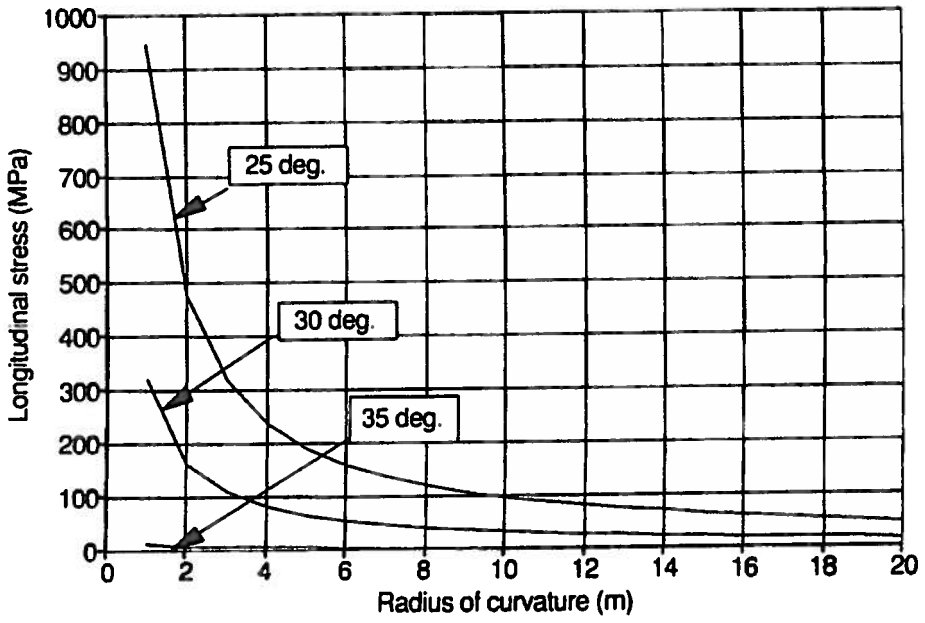

Figure A.2 Longitudinal stress needed to keep the cross section rotation less than 0.1^{o}

ISBN 82-7119-427-5 ISSN 0802-3271

APPENDIX B

PROOF OF LOXODROMIC CURVE EXPRESSIONS

B.1 Strain, torsion and curvatures

Let the vectors, g_k of arbitrary length be directed along the centre line and the principal axes of the tendon cross section. By use of Eqs.(2.21)-(2.23) the following expressions are obtained:

$$\kappa_1 = \frac{g_3}{|g_3|} \cdot \frac{\frac{dg_2}{dX^1}}{|g_2|} \tag{B.1}$$

$$\kappa_2 = \frac{g_3}{|g_3|} \cdot \frac{\frac{dg_1}{dX^1}}{|g_1|} \tag{B.2}$$

$$\kappa_3 = \frac{g_2}{|g_2|} \cdot \frac{\frac{dg_1}{dX^1}}{|g_1|} \tag{B.3}$$

 ISBN 82-7119-427-5 ISSN 0802-3271

By using the position vector components defined in Eqs.(2.4)-(2.6), the tangent vector g_I is obtained by simple differentiation of these components with respect to the arc length coordinate X^I as:

$$\begin{aligned} g_1 &= (\rho\phi_{,1}\cos\phi + Rv_{,1}\sin v\sin\phi - R\phi_{,1}\cos v\cos\phi)\, E_1 \\ &+ (\rho\phi_{,1}\sin\phi - Rv_{,1}\sin v\cos\phi - R\phi_{,1}\cos v\sin\phi)\, E_2 \\ &+ Rv_{,1}\cos v\, E_3 \end{aligned} \tag{B.4}$$

Since the loxodromic curve intersects the coordinate curves on the surface with the constant angle α, the ϕ coordinate is uniquely defined in terms of the arc length coordinate X^I as:

$$\phi = \frac{\cos\alpha}{\rho} X^1 \tag{B.5}$$

The derivatives of Eq.(B.4) are thus given by using Eq.(B.5) and Eq.(A.15). The length of the g_I vector is determined to be:

$$|g_1| = 1 - \frac{R}{\rho}\cos^2\alpha\cos v \tag{B.6}$$

By further differentiation with respect to X^I:

$$\begin{aligned} \frac{dg_1}{dX^1} &= (-\rho\phi_{,1}^2\sin\phi + 2Rv_{,1}\phi_{,1}\sin v\cos\phi + (Rv_{,1}^2+R\phi_{,1}^2)\cos v\sin\phi)\, E_1 \\ &+ (\rho\phi_{,1}^2\cos\phi + 2Ev_{,1}\phi_{,1}\sin v\sin\phi - (Rv_{,1}+R\phi_{,1}^2)\cos v\cos\phi)\, E_2 \\ &+ Rv_{,1}^2\sin v\, E_3 \end{aligned} \tag{B.7}$$

The normal vector is determined on the basis of the surface normal, using Eqs.(A.1)-(A.3) and normalization, as:

 ISBN 82-7119-427-5 ISSN 0802-3271

$$\frac{g_2}{|g_2|} = \cos\nu\sin\phi E_1 - \cos\nu\cos\phi E_2 - \sin\nu E_3 \tag{B.8}$$

where the normalization is based on the length of the g_2 vector which is determined to be:

$$|g_2| = R\rho(1-\frac{R}{\rho}\cos\nu) \tag{B.9}$$

Then by one time differentiation of g_2 with respect to X^1:

$$\begin{aligned}\frac{dg_2}{dX^1} = {} & (-R\rho\sin\nu\sin\phi\nu_{,1}+R\rho\cos\nu\cos\phi\phi_{,1}+2R^2\cos\nu\sin\nu\sin\phi\nu_{,1}-R^2\cos^2\nu\cos\phi\phi_{,1})E_1 \\ & + (R\rho\sin\nu\cos\phi\nu_{,1}+R\rho\cos\nu\sin\phi\phi_{,1}-2R^2\cos\nu\sin\nu\cos\phi\nu_{,1}-R^2\cos^2\nu\sin\phi\phi_{,1})E_2 \\ & + (-R\rho\cos\nu\nu_{,1}\cos\nu\nu_{,1}+R^2\cos^2\nu\nu_{,1}-R^2\sin^2\nu\nu_{,1})E_3\end{aligned} \tag{B.10}$$

The unit vector g_3 along X^3 is determined by taking the cross-product as:

$$\frac{g_3}{|g_3|} = \frac{g_1}{|g_1|}\times\frac{g_2}{|g_2|} \tag{B.11}$$

By using Eqs.(B.4-B.11) in Eqs.(B.1-B.3), the following results emerge:

$$\kappa_1 = \frac{\sin\alpha\cos\alpha}{R(1-\frac{R}{\rho}\cos^2\alpha\cos\nu)} \approx \frac{\sin\alpha\cos\alpha}{R}(1+\frac{R}{\rho}\cos^2\alpha\cos\nu) \tag{B.12}$$

$$\kappa_2 = -\frac{\cos\alpha}{\rho}\frac{((1+\sin^2\alpha)\sin\nu+(\frac{R}{\rho})^2\cos^2\alpha\cos^2\nu\sin\nu)}{(1-2\frac{R}{\rho}\cos^2\alpha\cos\nu+(\frac{R}{\rho})^2\cos^2\alpha\cos^2\nu)} \approx -\frac{\cos\alpha}{\rho}(1+\sin^2\alpha)\sin\nu \qquad (B.13)$$

$$\kappa_3 = \frac{\sin^2\alpha}{R}\frac{(1-\frac{R}{\rho}\frac{\cos^2\alpha}{\sin^2\alpha}\cos\nu+(\frac{R}{\rho})^2\frac{\cos^2\alpha}{\sin^2\alpha}\cos^2\nu)}{(1-\frac{R}{\rho}\cos^2\alpha\cos\nu)} \approx \frac{\sin^2\alpha}{R}(1-\frac{\cos^4\alpha}{\sin^2\alpha}\frac{R}{\rho}\cos\nu) \qquad (B.14)$$

which concludes the proof regarding twist and curvature changes.

The longitudinal component of the Green strain tensor along the rod centre line is further determined by consideration of the displacements relative to the undeformed reference system. The components are determined by using Eq.(B.4) in Eq.(2.56) as:

$$E_{11}^{*0} = \frac{1}{2}(\boldsymbol{g}_1 \cdot \boldsymbol{g}_1 - \boldsymbol{G}_1 \cdot \boldsymbol{G}_1) = -\frac{R}{\rho}\cos^2\alpha\cos\nu + \frac{1}{2}(\frac{R}{\rho})^2\cos^2\alpha\cos^2\nu \qquad (B.15)$$

B.2 Proof of the consideration made in Sub-section 2.4.6

In Sub-section 2.4.6, it was noted that the resulting torsion of the cross section may be obtained in two ways, either by using the $\boldsymbol{G}_I$ triad, which is fixed to the tendon cross-section, directly according to Eq.(2.21), or by use of Eq.(2.11), Eq.(2.16) and Eq.(2.20). The first alternative was used in the previous derivation of Eq.(B.12), whereas the second alternative is examined below.

By using κ_2 from Eq.(B.13) and κ_3 from Eq.(2.14) in Eq.(2.20) and by differentiation and neglecting higher order terms of R/ρ, the second term of Eq.(2.16) may be written as:

$$\frac{d\omega}{dX^1} = -\frac{\cos\alpha\sin\alpha}{\rho}\left(1+\frac{1}{\sin^2\alpha}\right)\cos\nu \qquad \text{(B.16)}$$

The first term is determined by means of Eq.(2.11), where the I_1 triad has to be based on the curve principal torsion flexure axes, which generally not are coincident with the G_1 triad of the tendon cross-section. The consequence of this is that when expressing the I_2 vector, the second derivative of the arc length must be used instead of the surface normal. The result is:

$$\tau = \frac{\sin\alpha\cos\alpha}{R}\left(1 + \left(2+\cos^2\alpha+\frac{\cos^2\alpha}{\sin^2\alpha}\right)\frac{R}{\rho}\cos\nu\right) \qquad \text{(B.17)}$$

which gives the same result as Eq.(B.12) when added to Eq.(B.16). This concludes the proof.

B.3 Proof of the consideration made in Sub-section 2.5.3

In Sub-section 2.5.3 it was noted that by using the displacement functions of Eq.(2.29) and Eq.(2.30) in the curvature increments of Eq.(2.77) and Eq.(2.79), these increments can be used to obtain the same results as Eq.(2.64) and Eq.(2.66) by respective addition of the increments defined by Eq.(2.31) and Eq.(2.32). This means that if the geodesic is considered as a reference state from which further deformation takes place towards the loxodromic curve, the kinematical description developed in Chapter 2 is consistent with direct application of differential geometry.

By using the restraints induced by Eq.(2.34), Eq.(2.93) and Eq.(2.94), the twist and normal curvature increments of Eq.(2.77) and Eq.(2.79) can be approximated as:

$$\Delta\kappa_1 = \kappa_1 u_{1,1} + (\kappa_3-\kappa_t)u_{3,1} \qquad \text{(B.18)}$$

 ISBN 82-7119-427-5 ISSN 0802-3271

$$\Delta\kappa_3 = -2\kappa_1 u_{3,1} + \kappa_3 u_{1,1} \tag{B.19}$$

Further, by introducing the negative signed versions of Eq.(2.29) and Eq.(2.30) in the two above equations and differentiation, the following results emerge:

$$\Delta\kappa_1 = \frac{\sin\alpha\cos\alpha}{\rho}\left(\frac{\cos^2\alpha}{\sin^2\alpha} - \sin^2\alpha - 1\right)\cos v \tag{B.20}$$

$$\Delta\kappa_3 = \frac{\cos^2\alpha}{\rho}\left(2 + \sin^2\alpha\right)\cos v \tag{B.21}$$

The negative sign of Eq.(2.29) and Eq.(2.30) is due to the fact that the geodesic is used as the reference, rather than the loxodromic curve.

It is now easily seen that by adding the increments of Eq.(2.31) and Eq.(2.32) respectively, the results of Eq.(2.64) and Eq.(2.66) are obtained for the total increment, which concludes the proof.

ISBN 82-7119-427-5 ISSN 0802-3271

APPENDIX C

TABLES OF FATIGUE STRESS RANGES

C.1 Pipe 2 stress ranges at failure cross section

The subsequent tables gives the calculated maximum stress ranges at the failure cross section inside the end fitting of both pipes. The values are obtained at 45° angle intervals of the surface coordinate v around the circumference. In these tables, $\Delta\sigma_{at}$ is the axial stress induced by tension, $\Delta\sigma_{ac}$ is the axial stress induced by curvature, $\Delta\sigma_{b3}$ is the bending stress caused by bending about the X^3 axis, $\Delta\sigma_{11}$ is the total longitudinal stress and $\Delta\sigma_{fg}$ is the fatigue limit of the material.

ISBN 82-7119-427-5 ISSN 0802-3271

Table C.1 Stress ranges and fatigue limit, Sequence 1, outer layer.

Position, v (°)	$\Delta\sigma_{at}$ (MPa)	$\Delta\sigma_{ac}$ (MPa)	$\Delta\sigma_{b3}$ (MPa)	$\Delta\sigma_{11}$ (MPa)	$\Delta\sigma_{fg}$ (MPa)
0	84	42	38	164	323
45	84	-48	11	47	355
90	84	-100	-5	-21	375
135	84	-87	-1	-4	370
180	84	-61	7	30	360
225	84	35	36	155	325
270	84	130	65	279	290
315	84	127	69	275	291

Table C.2 Stress ranges and fatigue limit, Sequence 2, outer layer.

Position, v (°)	$\Delta\sigma_{at}$ (MPa)	$\Delta\sigma_{ac}$ (MPa)	$\Delta\sigma_{b3}$ (MPa)	$\Delta\sigma_{11}$ (MPa)	$\Delta\sigma_{fg}$ (MPa)
0	168	-42	38	164	323
45	168	-102	20	85	344
90	168	-109	18	77	347
135	168	-91	23	100	340
180	168	0	51	219	308
225	168	115	86	369	265
270	168	133	91	392	259
315	168	72	73	313	281

 ISBN 82-7119-427-5 ISSN 0802-3271

Table C.3 Stress ranges and fatigue limit, Sequence 1, inner layer.

Position, v (^{o})	$\Delta\sigma_{at}$ (MPa)	$\Delta\sigma_{ac}$ (MPa)	$\Delta\sigma_{b3}$ (MPa)	$\Delta\sigma_{11}$ (MPa)	$\Delta\sigma_{fg}$ (MPa)
0	98	37	41	176	319
45	98	141	72	311	281
90	98	140	72	310	281
135	98	38	41	177	319
180	98	-70	8	36	359
225	98	-153	-16	-71	409
270	98	-145	-14	-61	403
315	98	-62	11	47	356

Table C.4 Stress ranges and fatigue limit, Sequence 2, inner layer.

Position, v(^{o})	$\Delta\sigma_{at}$ (MPa)	$\Delta\sigma_{ac}$ (MPa)	$\Delta\sigma_{b3}$ (MPa)	$\Delta\sigma_{11}$ (MPa)	$\Delta\sigma_{fg}$ (MPa)
0	196	-48	45	193	314
45	196	90	86	372	264
90	196	182	114	492	230
135	196	155	106	457	240
180	196	31	69	296	285
225	196	-111	26	111	337
270	196	-180	5	21	364
315	196	-153	13	56	353

ISBN 82-7119-427-5 ISSN 0802-3271

C.2 Pipe 1 stress ranges at failure cross section in outer layer

Table C.5 Stress ranges and fatigue limit, Sequence 1, outer layer

Angle , v (^{o})	$\Delta\sigma_{at}$ (MPa)	$\Delta\sigma_{ac}$ (MPa)	$\Delta\sigma_{11}$ (MPa)	$\Delta\sigma_{fg}$ (MPa)
0	112	9	121	342
45	112	-5	107	344
90	112	-14	98	345
135	112	-14	98	345
180	112	-8	104	344
225	112	6	118	342
270	112	15	127	341
315	112	15	127	341

Table C.6 Stress ranges and fatigue limit, Sequence 2, outer layer

Angle , v (^{o})	$\Delta\sigma_{at}$ (MPa)	$\Delta\sigma_{ac}$ (MPa)	$\Delta\sigma_{11}$ (MPa)	$\Delta\sigma_{fg}$ (MPa)
0	280	17	297	317
45	280	4	284	319
90	280	-10	270	321
135	280	-18	262	320
180	280	-14	266	320
225	280	-12	268	320
270	280	11	291	318
315	280	20	300	317

 ISBN 82-7119-427-5 ISSN 0802-3271